

601153

2 of 3

RADC-TDR-64-140, Vol III

166-P \$3.00



INVESTIGATION OF LINEAR BEAM AND NEW CONCEPTS
OF MICROWAVE POWER GENERATION

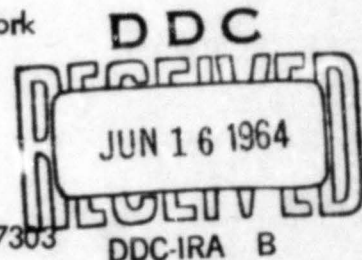
Part I - Reduction of Spurious Output Signals in High Power Klystrons

Part II - A Study of Space-Charged Wave Propagation Along A
Periodically Varying Electron Beam

TECHNICAL DOCUMENTARY REPORT NO. RADC-TDR-64-140, Vol III

May 1964

Techniques Branch
Rome Air Development Center
Research and Technology Division
Air Force Systems Command
Griffiss Air Force Base, New York



Project No. 5573, Task No. 557303

(Prepared under Contract AF30(602)-3243 by the School of Electrical
Engineering, Cornell University, Ithaca, New York)

When US Government drawings, specifications, or other data are used for any purpose other than a definitely related government procurement operation, the government thereby incurs no responsibility nor any obligation whatsoever; and the fact that the government may have formulated, furnished, or in any way supplied the said drawings, specifications, or other data is not to be regarded by implication or otherwise, as in any manner licensing the holder or any other person or corporation, or conveying any rights or permission to manufacture, use, or sell any patented invention that may in any way be related thereto.

Qualified requesters may obtain copies from Defense Documentation Center.

Defense Documentation Center release to Office of Technical Services is authorized.

If this copy is not needed, return to RADC (EMATE).

FOREWORD

The research reported in these volumes was performed at the School of Electrical Engineering, Cornell University under Contract AF30(602)-3243. The following is the breakdown of the reports contained in each volume:

Vol I - INVESTIGATION OF LINEAR BEAM AND NEW CONCEPTS OF MICROWAVE POWER GENERATION (Research Report EERL3)

Vol II - INVESTIGATION OF LINEAR BEAM AND NEW CONCEPTS OF MICROWAVE POWER GENERATION

Part I - Theoretical and Experimental Considerations of the Double-Quantum Photoelectric Effect (Research Report EE566)

Part II - Gain Expressions for Beam-Plasma Interaction (Research Report EERL5)

Vol III - INVESTIGATION OF LINEAR BEAM AND NEW CONCEPTS OF MICROWAVE POWER GENERATION

Part I - Reduction of Spurious Output Signals in High Power Klystrons (Research Report EE579)

Part II - A Study of Space-Charged Wave Propagation Along a Periodically Varying Electron Beam (Research Report EERL4)

Key Words: Electron Tube Devices, Klystrons

ABSTRACT
(Part I)

This is a study of a particular electromagnetic compatibility problem. The objective of this work was to develop and to provide for experimental verification of a design technique for reducing spurious output signals in high-power klystrons, and thus to provide a practical method for the reduction of spurious output signals in high-power radar transmitters where the power amplifier is a klystron.

The study included: (1) the definition of the particular electromagnetic compatibility problem, (2) a solution for the problem, and (3) the design and construction of a high-power, hot-test facility for measuring spurious output signals. The approach in developing the cavity design was to consider the higher-order modes present in the output cavity and place these mode resonances systematically at optimum frequencies. The test facility was constructed from a high-power radar transmitter and the transmission line included a signal-sampling network capable of measuring up to the sixth harmonic of an S-band fundamental signal.

Absolute power measurements were made on the second and third harmonics of the VA-87C klystron (S-band). Relative power measurements were made on the second, third, fourth, and fifth harmonics of the SAL-36 klystron (L-band). These measurements, along with other pertinent data, are compared.

ABSTRACT (Part II)

The problem of space-charge wave propagation along a scalloped Brillouin beam is investigated both by analysis and experiment. The major result of the analysis is the description of the r-f currents and velocities in the beam by the solutions of Mathieu's Equation. Both growth and decay are predicted with a maximum instability rate of 6.8 db per scallop. This instability includes a locking between the periods of the space-charge wave and the scallop on the beam. Experimental evidence of both amplification and attenuation as well as of the locking phenomenon is presented and shown to agree with the predicted values. Effects of various parameters are discussed, and experimental data showing the effects of cavity position and magnetic field are presented as the bulk of the experimental work.

Three important phenomena not adequately covered by the theory were experimentally detected. Saturation began to occur just as the r-f to d-c power ratio became equal to .01. The effect of a fraction of a per cent of axial flux through the cathode and a small translaminar stream was found to give significantly different theoretical results. The third important observation was an anomalous growth in the peak velocity of the beam under no-signal conditions.

The experimental work was performed on a 5.2-kv, 1.15-micro-perveance Brillouin beam operating under pulsed conditions.

From these experimental results, it is concluded that the laminar, linear, generalized one-dimensional model is insufficient for accurate

numerical predictions. Additional knowledge of the amount and effect of any cathode-leakage flux and translaminar electrons is necessary to predict the quantitative behavior of space-charge waves on a scalloped Brillouin beam.

PUBLICATION REVIEW

This report has been reviewed and is approved. For further technical information on this project, contact R. Hunter Chilton, EMATE, Extension 4251.

Approved:

R. Hunter Chilton
R. HUNTER CHILTON
Project Engineer
Electron Devices Section

Approved:

Arthur J. Frohlich
Arthur J. Frohlich
Chief, Techniques Branch
Surveillance & Control Division

CONTENTS

	Page
PART I	
I. INTRODUCTION	1
II. DESCRIPTION OF THE ELECTROMAGNETIC COMPATIBILITY PROBLEM	3
A. ORIGIN OF SPURIOUS SIGNALS	3
B. NEED FOR ELECTRO-MAGNETIC COMPATIBILITY	4
III. SPURIOUS OUTPUT SIGNALS IN KLYSTRONS	6
A. MEASUREMENTS ON SPERRY SAL-36	7
B. MEASUREMENTS ON THE VARIAN VA-87	12
1. VA-87 Test Set	13
2. VA-87 Measurements	18
a. Multiprobe Measurements on VA-87	19
b. Measurements on the VA-87C	19
C. COMPARISON OF RESULTS	22
IV. PROPOSED METHOD OF REDUCING THE SPURIOUS OUTPUT SIGNALS IN HIGH-POWER KLYSTRONS	25
A. PROPOSED OUTPUT STRUCTURE	28
B. SOLUTION OF THE BOUNDARY VALUE PROBLEM	31
1. Analysis for Region 1	37
2. Analysis for Region 3	39
3. Analysis for Region 1 and 3	41

	Page
4. Analysis for Region 2	45
5. Analysis of Region 4	46
6. Analysis of Total Admittance Function	50
7. Special-Case Checks of Solution	51
C. CONSTRUCTION OF PROPOSED OUTPUT STRUCTURE	52
V. SUMMARY AND RECOMMENDATIONS	56
VI. REFERENCES	57

CONTENTS

	Page
PART II	
I. INTRODUCTION	59
II. STATEMENT OF THE PROBLEM	61
III. PHYSICAL EXPLANATION	62
IV. THEORY	65
A. MODEL	65
B. ASSUMPTIONS	66
C. FORM OF THE ARGUMENT	69
1. Notation	69
2. Analysis	69
D. PREDICTIONS	85
1. Growing Solutions	86
2. Effect of Initial Conditions	86
3. Relative Periods of Plasma and Scallop Waves	87
4. Nonsinusoidal Shape of the Envelope	89
5. Relation Between Experimental and Mathematical Parameters	90
6. Importance of Factors Suppressed by the Theory	92
V. EXPERIMENT	95
A. METHODS	95
1. Experimental Conditions	95
2. Means of Taking Data	97

	Page
3. Sample Data	102
4. Experimental Difficulties	106
B. VALIDITY OF THE ASSUMPTIONS	107
C. DISCUSSION OF THE PREDICTED RESULTS	112
1. Maximum Growth Rate	112
2. Cavity Position	115
3. Wavelengths	115
4. Effect of the Magnetic Field Parameter	124
5. Shift in the Minima	125
6. Curvature of the Standing Waves	125
D. DISCUSSION OF THE UNPREDICTED RESULTS	128
1. Power Saturation	128
2. Anomalous Velocity Growth	132
3. Differences Between Current and Velocity Data	135
4. Nonuniformities	137
VI. SUMMARY OF CONCLUSIONS	139
APPENDIX: DESCRIPTION OF THE APPARATUS	143
A. VACUUM SYSTEM	143
1. Primary Section	143
2. Secondary System	144
3. Construction	144
4. Seals	145
B. SCANNING MECHANISM	145
C. CATHODE	146
VII. REFERENCES	148

PART I

LIST OF ILLUSTRATIONS

Figure		Page
1	Circuit for Harmonic Measurements on SAL-36 Klystron.	9
2	Harmonic Filter Arrangement.	9
3	Variations of Fundamental and Harmonic Powers as a Function of Input Power for a Beam Voltage of 65 kv.	10
4	Variations of Fundamental and Harmonic Powers as a Function of Input Power for a Beam Voltage of 80 kv.	11
5	Block Diagram of VA-87 Spurious-Output Test Facility.	14
6	VA-87 Spurious-Output Test Facility.	15
7	VA-87, Test Instrument.	16
8	Block Diagram of VA-87, Signal-Sampling Device.	18
9	Variation of Second Harmonic Power in VA-87B as Beam Voltage Only is Changed.	20
10	Variation of Second Harmonic Power in VA-87B as Fundamental Frequency Only is Changed.	21
11	Variation of Output Power Level with a Change in Drive Power Only on the VA-87C.	23
12	Cross Section of Cavity with Symmetrical Output Coupling Iris.	29
13	Co-ordinate System of Cavity with Symmetrical Coupling Iris.	30
14	Interaction Cavity.	32
15	Coupling Cavity.	32
16	Assumed Interaction Gap Field ($r = a$).	36
17	Assumed Coupling Iris Field ($z = L$).	36
18	Coaxial Output Line.	47
19	New Output Structure for VA-87.	53
20	New Output Structure for VA-87 Minus Output Cavity.	55

Figure		Page
1	The A, q Stability Chart of Mathieu Equation: $d^2 I/dx^2 + (A + 2q \cos 2x)I = 0$.	78
2	a) Weighting Function $f(x_0, q)$ Versus Cavity Position x_0 Showing Variation with Gain Factor q . b) Normalized Radius r/b Corresponding to Cavity Position x_0 . (Taken From Bloom.)	81
3	Curves Used in the Calculation of the Growth Factor μ : (a) Dimensionless parameter $R^{\frac{1}{2}}$ defined by $R^{\frac{1}{2}} = \lambda_q/\lambda_p$ from Rigrod and Lewis, (b) Plasma reduction factor p given by $p = 1/R^{\frac{1}{2}} = \omega_q/\omega_p$, (c) Normalized plasma reduction factor $p/\beta b$, (d) Synchronous value of the ratio of gain factor to percentage scallop $(q/\Delta)_0$.	84
4	Schematic Diagram of Electron-Beam Analyzer.	98
5	Sample Data of r-f Current Distributions. a) Cavity Placed at Optimum Position for Amplification, b) Cavity Placed at Optimum Position for Attenuation, c) Space-Charge Wave Propagation on the Strict Brillouin Beam.	103
6	Sample Data of D-C Current Distribution on Scalloping Beam.	104
7	Peak Velocity and D-C Current along the Axis. a) Peak Velocity with Cavity Placed at Optimum Position for Amplification in each Case (Last curve shows growth in no-signal peak velocity), b) D-C Current along the Axis for Corresponding Magnetic Fields.	105
8	R-F and D-C Current Distributions at a Beam Cross-Section.	106

Figure		Page
9	Growth Factor μ and Percentage Scalloping versus Axial Magnetic Field Strength. (a) Curve is Plot of Calculated Values of the Growth Factor μ : (Data points are experimental results measured on velocity and current profiles along the axis.) (b) Curve is Plot of Measured Values of Percentage Scalloping. (Ordinate scale is multiplied by 1000.)	113
10	Peak-Velocity Standing Waves along the Scalloped Beam with 10-w Drive Level and a Magnetic Field Strength of 209 gauss (Figures a, b, c, and d show a Continuous Variation of Cavity Position through a Full Scallop Cycle Starting with $x_0 = 3\pi/4$).	116
11	a) Curve Shows Plot of Theoretical Effective Growth Factor versus Position of Cavity; Data Points are Experimental Results under Corresponding Conditions; b) Plot of Beam Radius Corresponding to Cavity Position.	117
12	Wavelengths versus Axial Magnetic Field Strength; (a) Plot of Theoretical Effective Plasma Half-Wavelength, (b) Plot of Theoretical Scallop Wavelength with No Cathode-Leakage Flux, (c) Plot of Measured Scallop Wavelength at the Beam Edge, (d) Plot of Theoretical Cyclotron Wavelength; Data Points Are from Experimental Results Using r-f and d-c Peak Velocity and d-c Current Measurements.	118
13	Total Annular r-f Current versus Axial Distance from the Anode with Cavity Position as Parameter.	126
14	Peak-Velocity Standing Waves along the Scalloped Beam with and without an Input Signal.	127
15	Peak-Velocity Standing Waves along the Scalloped Beam for Various Input Power Levels.	129
16	Growth Factor μ versus r-f Input Power with Magnetic Field as Parameter.	130

Figure		Page
17	No-Signal Peak Velocity along the Scalloped Beam for Various Magnetic Fields.	133
18	Effective Plasma Half-Wavelength versus Axial Magnetic Field Strength. (Curve shows plot of theoretical values of space-charge half-wave-length; data points are measured values taken from velocity standing waves.)	136

PART I

REDUCTION OF SPURIOUS OUTPUT SIGNALS
IN HIGH-POWER KLYSTRONS

A. R. Howland, Jr.

I. INTRODUCTION

The problems associated with electromagnetic compatibility in the microwave region are manifold. These problems may render entire systems inoperative, produce erroneous system results, and reduce the number of systems that can be used, since each system occupies a given segment of the available electromagnetic spectrum.

Solution of the electromagnetic compatibility problem can be achieved by time sharing in a particular geographic area, by frequency allocation, or by a reduction in the required electromagnetic spectrum for each system. The last method is the only solution that provides for a minimum of "down-time" and extends present technology.

This study attempts a practical solution for the problem of reducing the required spectrum allocation for high-power radar systems that use a klystron power amplifier in the transmitter. The major electromagnetic compatibility problem associated with high-power multicavity klystrons is that of reducing the harmonically related spurious output signals. This work is essentially a continuation of the work started by L. A. MacKenzie.¹

There are two basically different methods by which these spurious output signals can be reduced or effectively eliminated: (1) by the use of external filters and (2) by improving the design of the klystron. The first method applies to existing installations. The second method applies to both existing and future installations. The primary usefulness of the second method is in future applications.

The measurement of spurious output signals in the wave-guide transmission line is complicated because these spurious signals are propagated in more than one mode in the wave guide. Such signals can be measured

by multiprobe techniques, by secondary wave-guide technique, and by the mode-mixer technique. A system for measuring spurious output signals based on the mode-mixer technique is installed as a part of the facility constructed for this program at Cornell University.

The measurements of spurious output signals made during this program were made as a function of the input signal level and the beam voltage of the tube under test. Measurements were made on Sperry Model SAL-36 and Varian Model VA-87C. The results and conclusions based on these tests follow.

II. DESCRIPTION OF THE ELECTROMAGNETIC COMPATIBILITY PROBLEM

Electronic equipment must be able to function in the presence of other equipment without interfering with the operation of the other equipment. To do this the equipment must be compatible with the electromagnetic environment. While high-power microwave transmitters are seldom affected in their operation by the presence of other electronic equipment in the electromagnetic environment, they are one of the major man-made sources of spurious electromagnetic energy that influences the operation of other equipment.

A. ORIGIN OF SPURIOUS SIGNALS

The sources of unwanted electromagnetic energy are natural and man-made. Natural sources, which usually consist of random noise, are: galactic noise, atmospheric noise, precipitation noise, and corona discharge. The amplitudes of the signals from these natural sources vary widely with time and cover a broad band of frequencies. Man-made sources are: motors, switches, diathermy machines, radar transmitters, communications transmitters, and equipment used for intentional jamming.

Electromagnetic compatibility problems arise because each time a wanted signal is generated, an infinite set of unwanted or spurious signals is also generated. This interference is compounded, since, in any nonlinear device, each signal (desired or spurious) can mix with every other signal (desired or spurious) to produce other sets of spurious energy, etc.

Obviously, if most of the signals in these infinite sets of spurious outputs did not have zero amplitude, the useful electromagnetic spectrum would be even more limited than it is today. The resultant of all of these signals, termed "noise," is observed as part of the ambient noise level of the electromagnetic environment; the noise products, referred to as spurious output signals, are those signals whose amplitude is well above the "noise floor." Because these signals are the strongest, and because they are often overlooked in the design stage of any system, these signals cause much of the interference.

A classic example of electromagnetic compatibility is reported by Campbell.² He describes interference in a radar-to-communication system. In this type of system, it is entirely possible that a spurious signal from the radar will be much greater than the transmitted fundamental or carrier-frequency signal of the communication system. Radar systems have spurious output signals that will interfere not only with communications systems but also with other radar systems. Considerable effort has gone into programs designed to predict the level and type of radio-frequency compatibility that can be expected in a given electromagnetic environment.³

B. NEED FOR ELECTRO-MAGNETIC COMPATIBILITY

As higher-power emitters of radio-frequency energy are developed and as receivers are designed to be more sensitive, the problems of providing electromagnetic compatibility for all systems becomes more pronounced. If these problems were solved, there would be a reduction in

system down-time resulting from spurious signals, a reduction in erroneous results, and larger numbers of operational systems could be included within the electromagnetic spectrum.

III. SPURIOUS OUTPUT SIGNALS IN KLYSTRONS

The multicavity klystron is operated in a nonlinear region for maximum efficiency. For this operating condition, harmonic signals of the fundamental or carrier signal are present in the klystron. For example, consider the case of a two-cavity klystron. From the point-of-view of ballistic theory, the current at the second cavity I_c can be expressed in a Fourier series as

$$I_c = I_o + 2I_o \sum_{n=1}^{\infty} J_n(nx) \cos n(\omega t - \theta_o) , \quad (1)$$

where I_o = d-c beam current, x = bunching parameter, θ_o = d-c transit angle, and $J_n(nx)$ = Bessel function of first kind of order n with argument nx . The first (or $n = 0$) term of this series I_o is the d-c beam current. The $n = 1$ term of the series, $2I_o J_1(x) \cos(\omega t - \theta_o)$, is the current at the fundamental frequency. The n^{th} term of this series, $2I_o J_n(nx) \cos n(\omega t - \theta_o)$, is the current at the n^{th} harmonic frequency, and the frequency of each current term of higher order is n times the fundamental frequency. If $nx \ll 1$, then

$$J_n(nx) \approx (nx)^n . \quad (2)$$

Under this condition, all terms in Equation (1) that are above the $n = 1$ term may be neglected; this is the condition of linear operation. For maximum efficiency, however, the fundamental-frequency current term

($n = 1$) must be maximized. The $n = 1$ term is a maximum when $J_1(x)$ takes on its greatest value; this occurs at $x = 1.84$. Thus, under the condition of maximum efficiency, it is not possible to neglect the $n = 2, 3, 4 \dots$ terms of the series, because the condition for linear operation as given by Equation (2) is violated. When operated at maximum efficiency, therefore, the klystron is a nonlinear device and the spurious signals are harmonically related to fundamental frequency. Since, for klystrons, the ballistic theory neglects space-charge forces, this discussion of the generation of harmonic signals is useful only as a first-order approximation. Several theories have been proposed to correct for space-charge debunching; however, none of these theories has been developed to provide a complete description of the modulated electron beam.

In this investigation, the first few harmonic signals generated by two klystrons (Sperry Model SAL-36 and Varian Model VA-87C) were measured in the laboratory. The equipment arrangement, measurement technique, and results of the measurements for both klystrons are discussed. In these measurements, both the r-f drive level and beam voltage were varied in order to determine the relative change in harmonic signal level as the bunching parameter was changed.

A. MEASUREMENTS ON SPERRY SAL-36

The equipment used to support the tube-under-test (SAL-36) consisted of the prototype AN/FPS-2 power supply and modulator. The SAL-36 is an experimental tube and is completely demountable. The signal-sampling network used to measure the second through the fifth

harmonic signals of the tube consisted of a small undercoupled loop in the output cavity, band-pass filters, and a receiver.

The measurements of the harmonic signals were made by sampling the harmonic power with the small undercoupled loop and feeding the signal through appropriate band-pass filters to a mixer, where it was combined with a local-oscillator signal to produce a 30 Mc/s signal that was first amplified by an i-f amplifier and then further amplified and detected by a receiver for display on an oscilloscope. The vertical displacement of the signal on the oscilloscope was kept constant in making the measurements. The relative change of the signal was measured by a calibrated attenuator in the output line of the harmonic signal, and by a calibrated attenuator in the receiver. The relative change in a harmonic signal in decibels was the amount that the attenuators had to be changed to keep the display on the oscilloscope constant. The circuit used to make these measurements is shown in Figures 1 and 2.

The relative change in the level of the second, third, fourth, and fifth harmonic signals of the SAL-36 is shown in Figures 3 and 4 for the indicated changes in beam voltage and r-f drive level. Specifically, Figure 3 shows the changes in the harmonics for a beam voltage of 65 kv as the r-f drive level is varied. Figure 4 shows the changes in the harmonics for a beam voltage of 80 kv as the r-f drive level is varied. The nominal operating beam voltage of the SAL-36 is 120 kv. From both Figures 3 and 4, it is seen that, in the small-signal case, the rate of change in the fundamental or in the harmonics with respect to r-f drive power is at the rate predicted by small-signal theory.⁴ The drive level for which

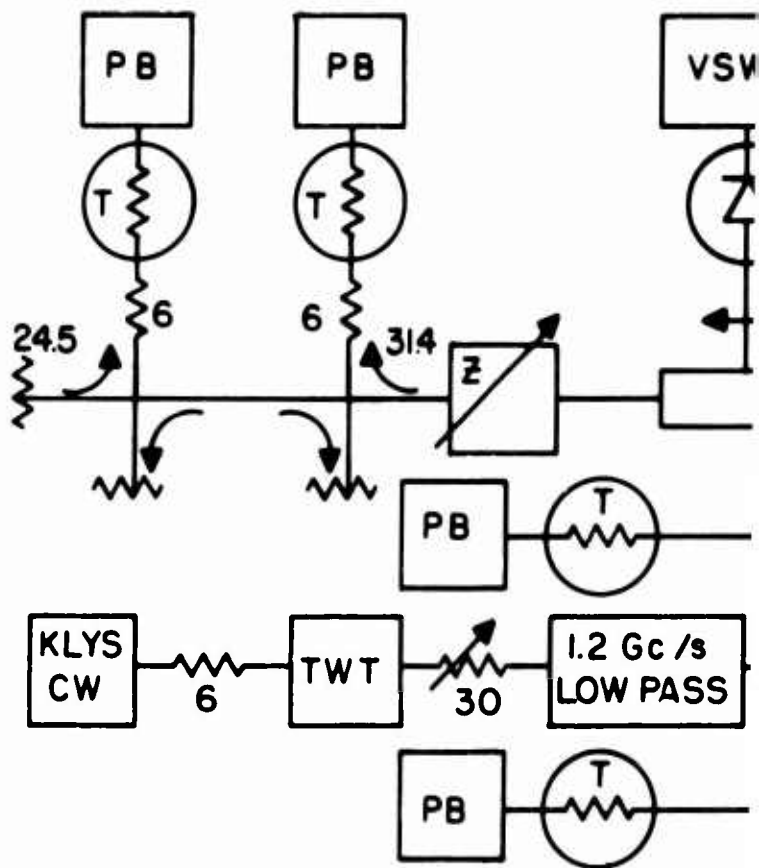


FIGURE 1. Circuit for Har

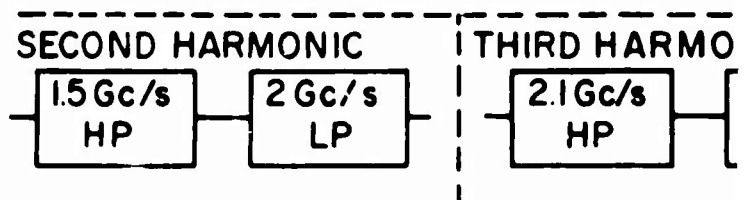
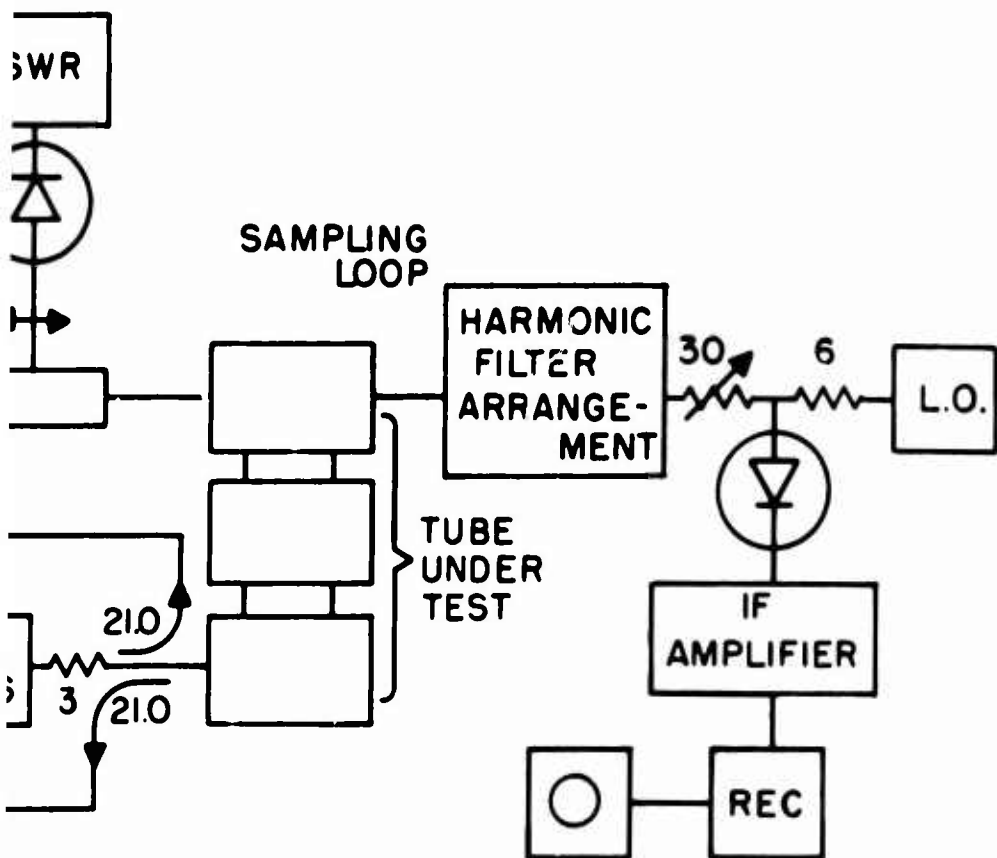
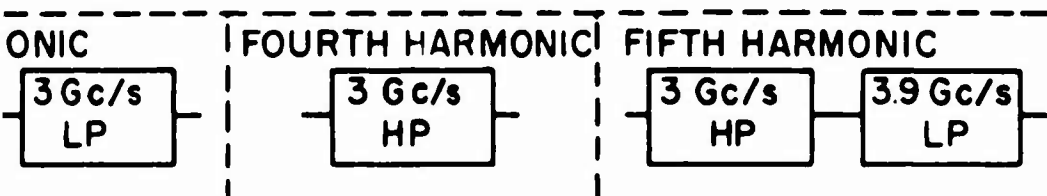


FIGURE 2. Ha



Harmonic Measurements on SAL-36 Klystron.



Harmonic Filter Arrangement.

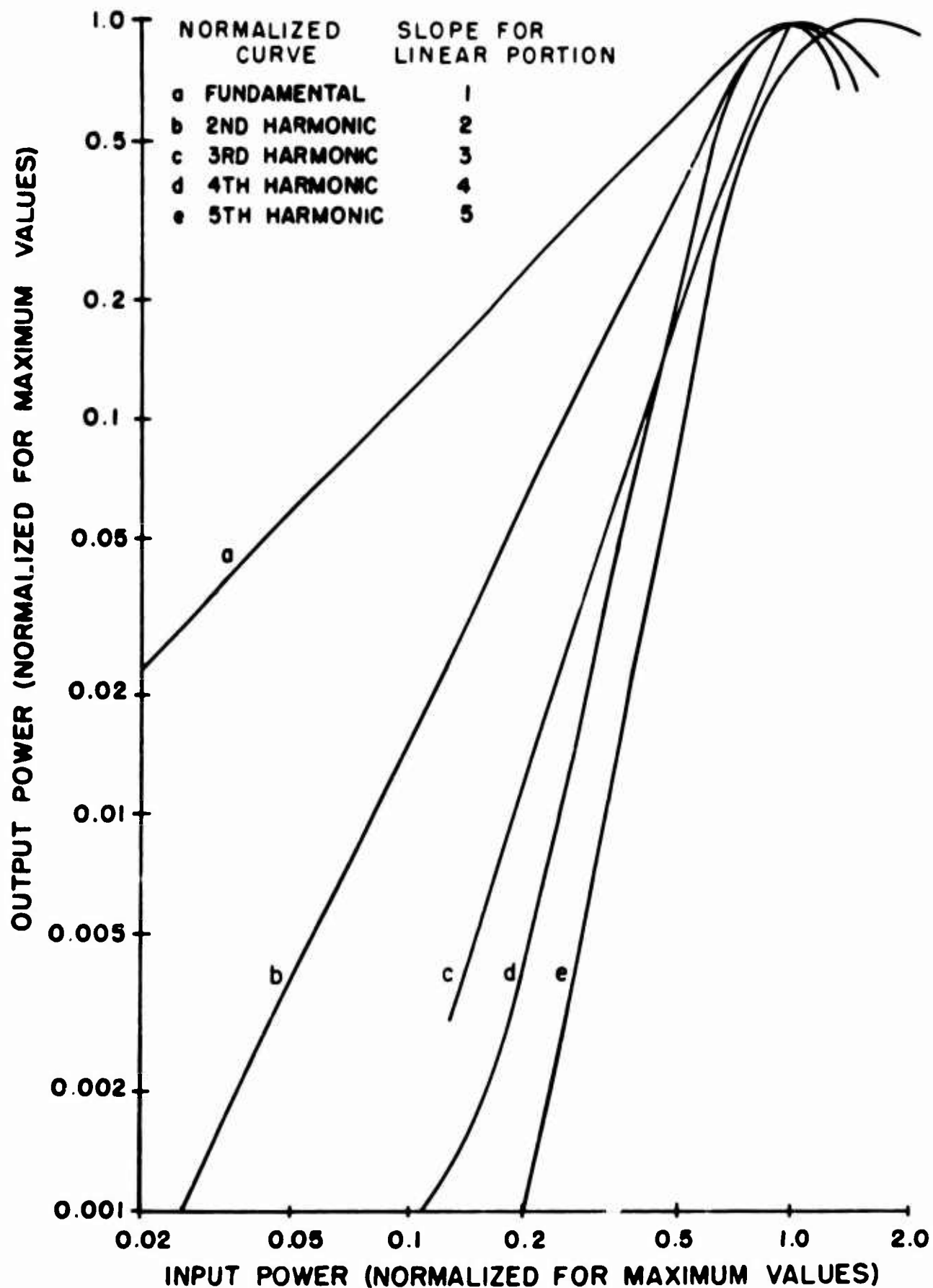


FIGURE 3. Variations of Fundamental and Harmonic Powers as a Function of Input Power for a Beam Voltage of 65 kv.

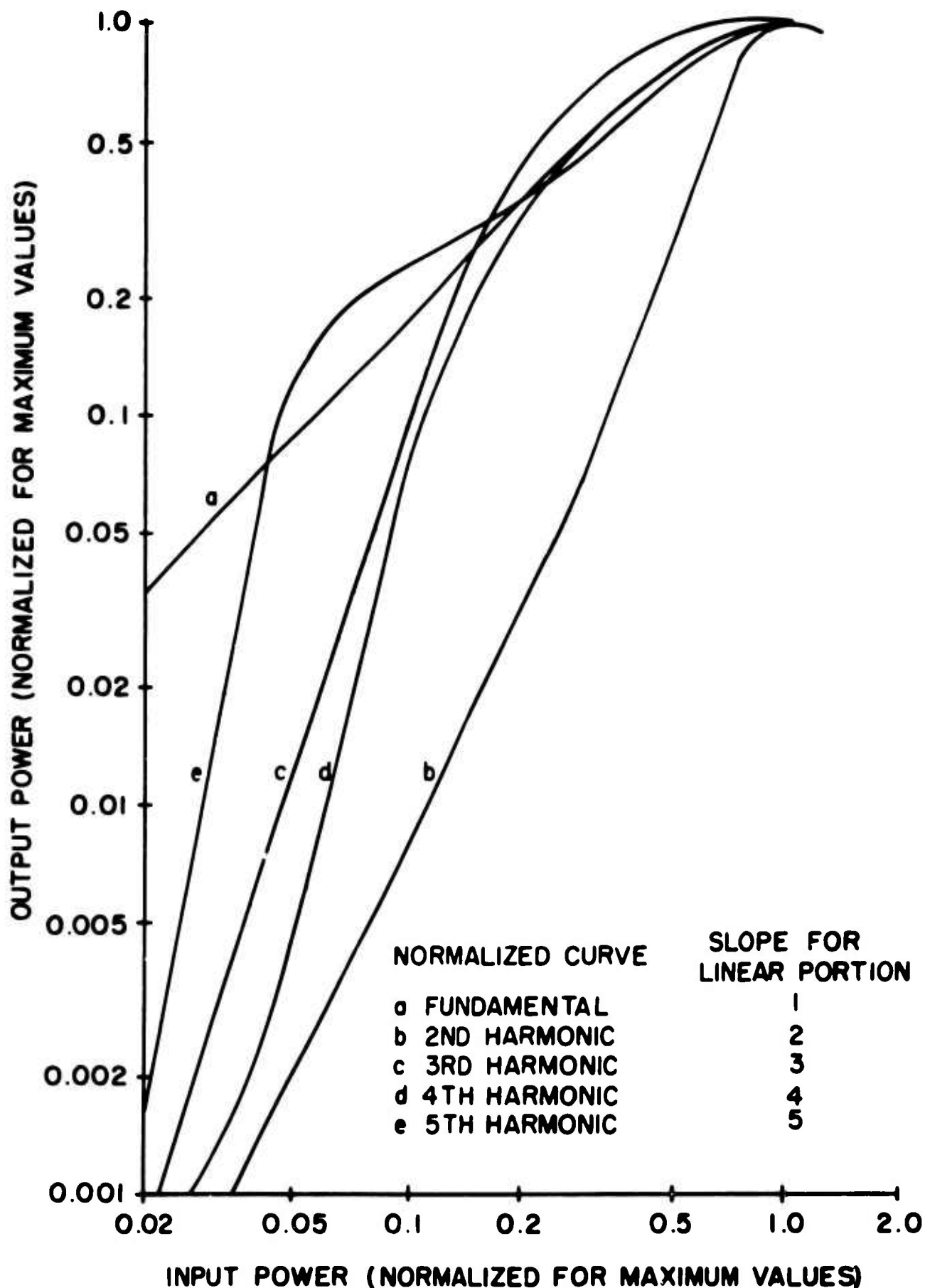


FIGURE 4. Variations of Fundamental and Harmonic Powers as a Function of Input Power for a Beam Voltage of 80 kv.

this small-signal analysis is valid as a function of the beam voltage of the tube-under-test, as shown by a comparison of Figures 3 and 4, where the beam voltage is the only parameter changed for the two sets of data. Note that as the beam voltage is increased, the harmonics saturate at a lower drive level.

These measurements of the second, third, fourth, and fifth harmonic signals in the output cavity of the SAL-36 show that as predicted by theory, spurious signals do indeed exist. The absolute power level of these spurious signals was not determined because only one small coupling loop was used. A number of small coupling loops would be required to determine the mode pattern present in the cavity at a specified frequency. If the cavity mode pattern were known and if the coupling coefficient of each loop to each mode were known as a function of frequency, then absolute power levels would be determined for the harmonic signals in the output cavity. Since the measurement of SAL-36 harmonic signals was one task of a general exploratory program, no effort was made to determine the absolute power level of the harmonic signals.

B. MEASUREMENTS ON THE VARIAN VA-87

Another klystron, the VA-87C, was obtained, together with the necessary power supplies, modulators, and signal generators and a wave-guide signal-sampling network. With this equipment, it was possible to measure the second and third harmonic signals that were coupled out of the tube into the output wave guide.

1. VA-87 Test Set

The VA-87 test set can be considered as three units: the support unit, the test instrument, and the measurement unit. A block diagram of the test set is shown in Figure 5 and a photograph of the system is shown in Figure 6. The support unit includes a high-power modulator and power supply, a r-f signal source, a r-f driver, a water-cooling system, associated power supplies, and necessary protective circuits. The unassembled test instrument, a portion of a modified four-cavity Varian VA-87C klystron, is shown in Figure 7. The test instrument consists of the electron gun, input cavity, second cavity, third cavity, and high-vacuum ball valve. The measurement unit consists of the Emtech signal-sampling network, filters, and power meters for the direct reading of the spurious energy level as a function of frequency.

The support unit provides d-c and r-f power for the test instrument. Water and protective circuits are provided for both the test instrument and measurement unit. Pulsed d-c power at 110 kv is required for the one-micropervance electron gun of the test instrument. This d-c power is obtained from an AN/FPS-6 power supply and modulator. The addition of a three-phase autotransformer (Variac) to the a-c input for the power supply permits a variation from zero to 110 kv in the beam voltage supplied to the test instrument. The r-f oscillator is a light-house tube in a cavity (part of the AN/TS-155E/UP signal generator), and the driver is a small three-cavity, c-w, space-charge-focused klystron (Sperry model SAS-60). The drive level of the r-f

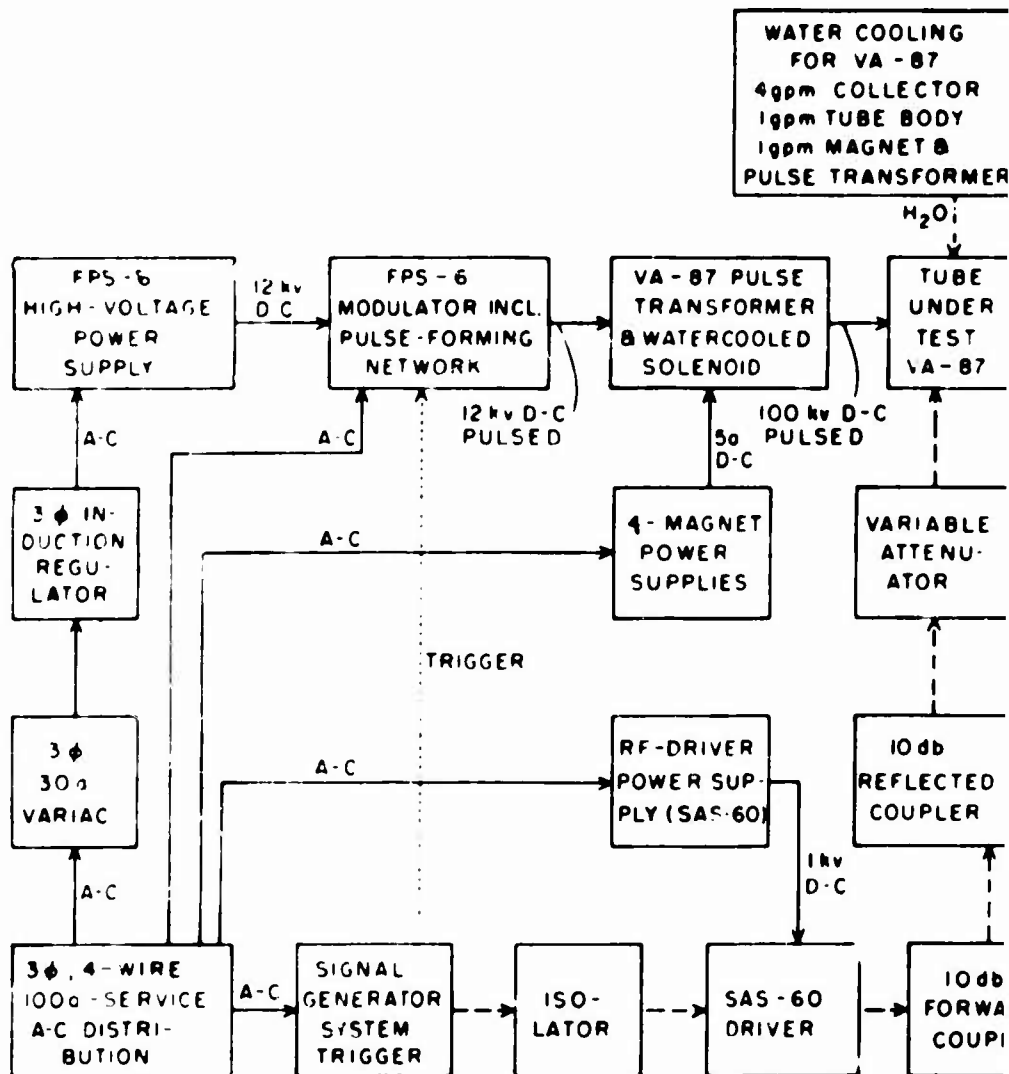
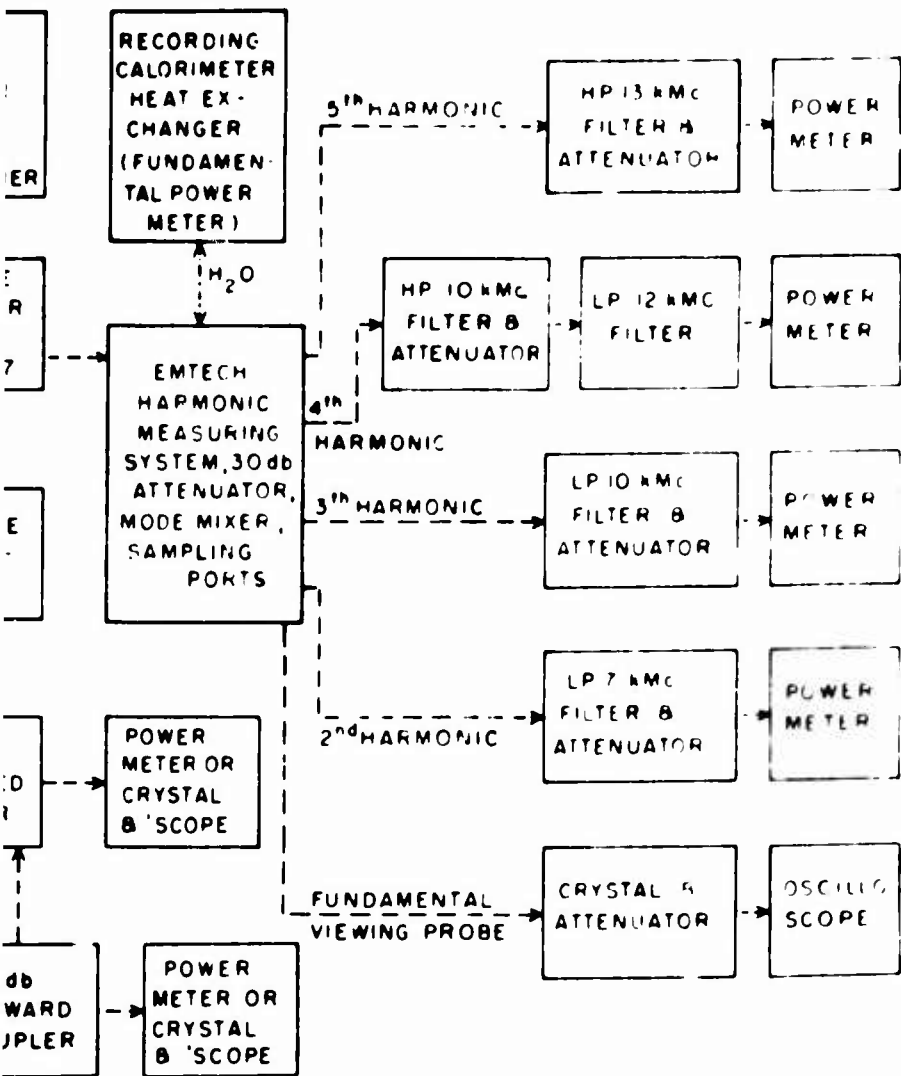


FIGURE 5. Block Diagram of VA-87 S



Spurious-Output Test Facility.

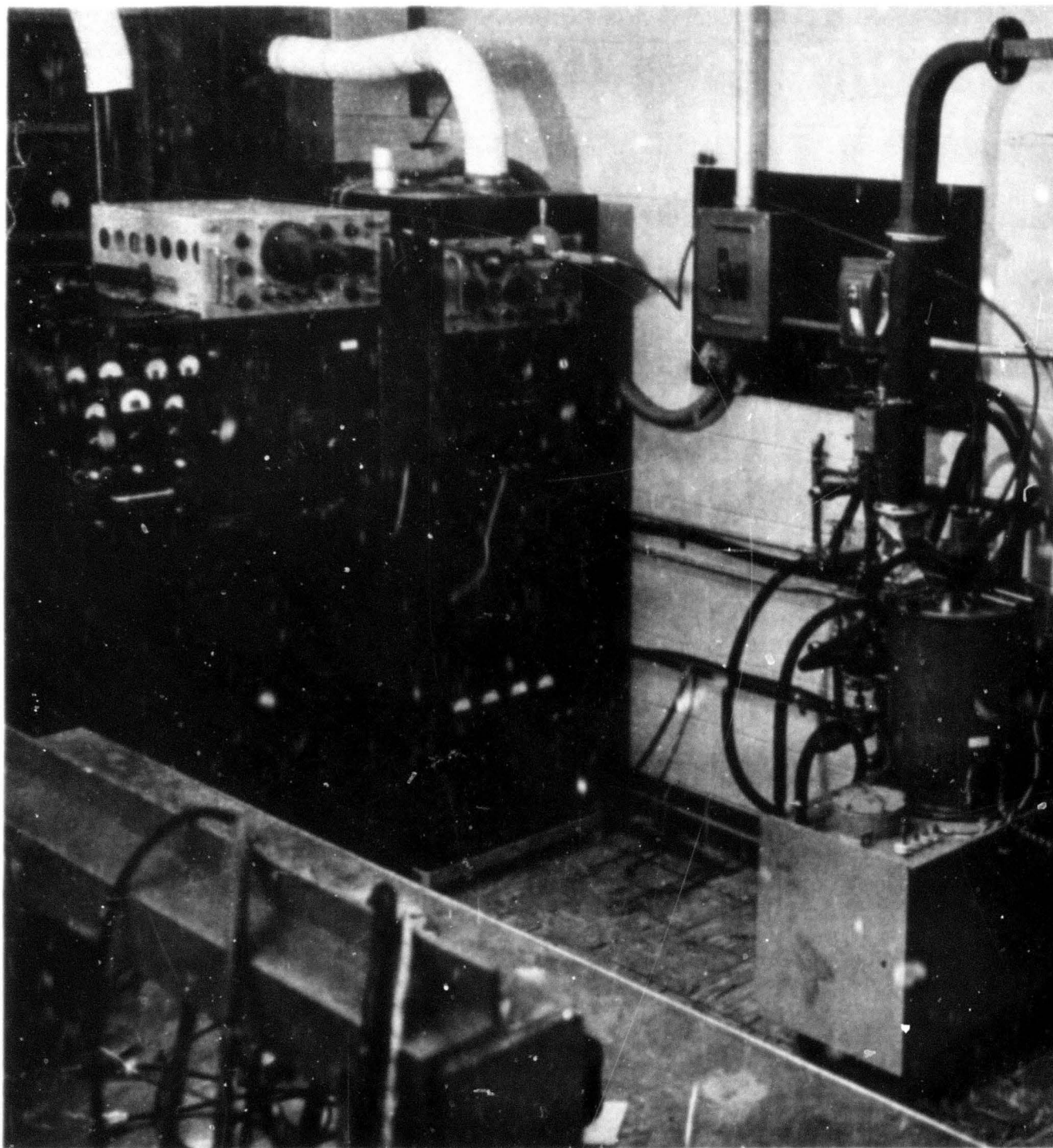
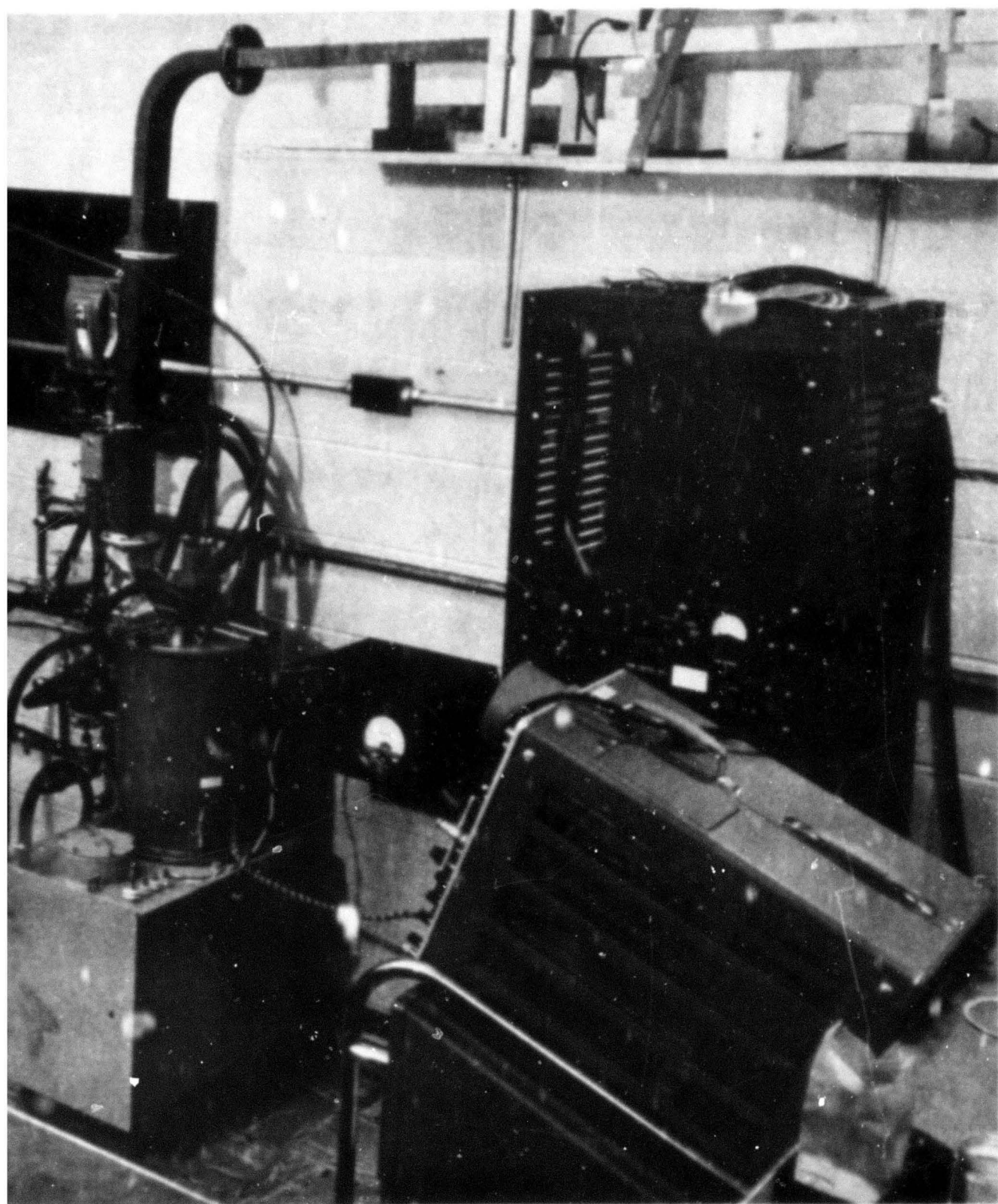


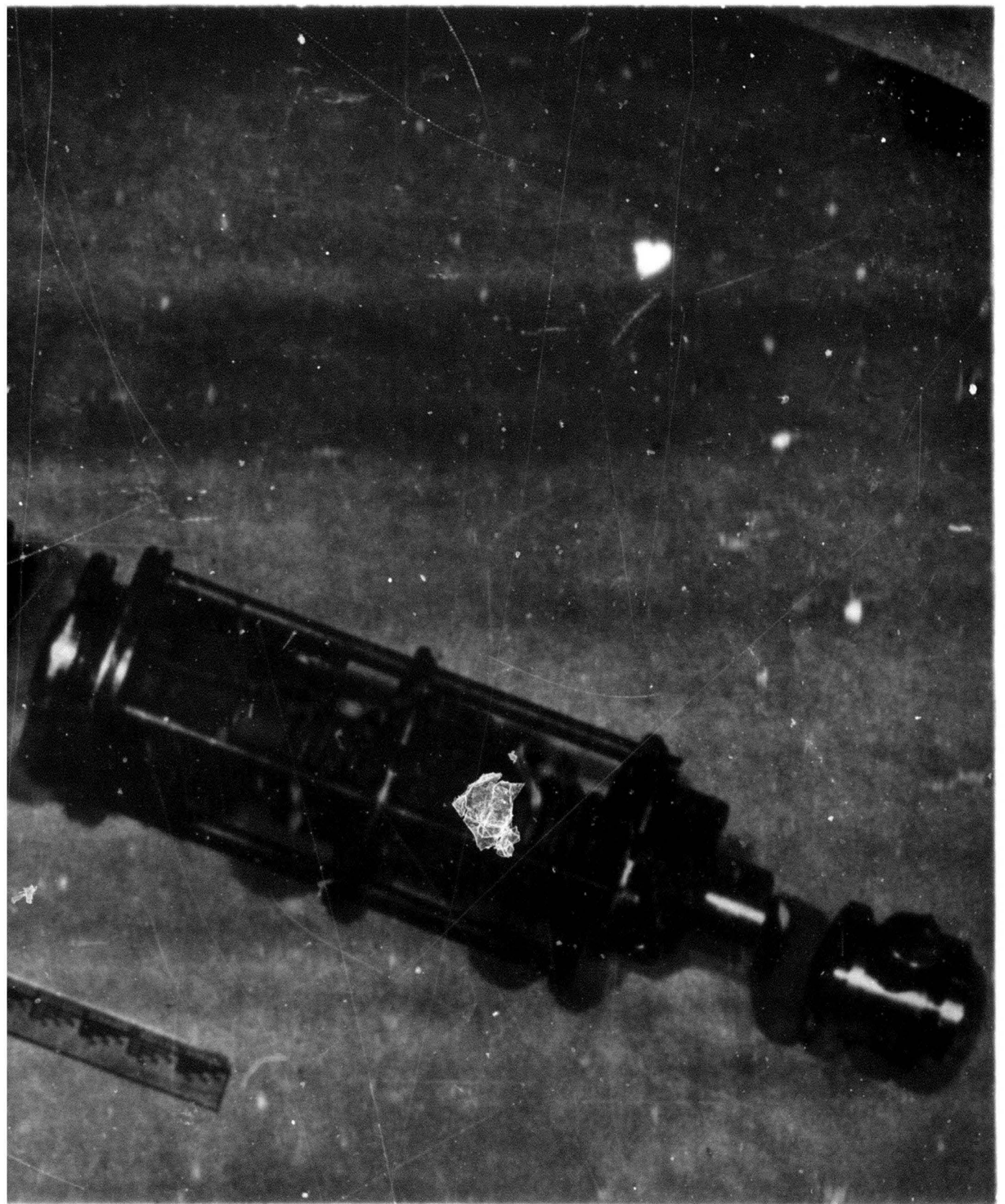
FIGURE 6. VA-87 Spurious-Output Test Facility



is-Output Test Facility.



FIGURE 7. VA-87, Test Instru



-87, Test Instrument.

input to the test instrument is continuously variable from zero to 6 w peak. This signal generator also contains the system trigger unit. It is possible to vary the r-f pulse width in this test set and to adjust the various timing circuits so that (1) the pulse envelope of the r-f signal is centered in the beam voltage pulse, (2) the pulse envelope of the r-f signal and the beam voltage pulse occur at the same time with equal pulse widths, and (3) the beam voltage pulse is centered inside the pulse envelope of the r-f signal. The pulse envelope of the r-f signal discussed here may be either the r-f drive signal or the fundamental output signal of the VA-87

The test instrument (electron gun and first three cavities of a VA-87C) was modified to permit recoating of the cathode, continuous pumping, and changing of the output structure under test without letting the electron gun down to air. Figure 7 shows (1) the vacuum flanges added to the electron gun, and (2) the ball valve added to the drift tube after the third cavity. Any output structure for which hot-test characteristics are desired can be connected to the test instrument at the flange on the ball valve. The system requires that the output structure include a collector, operate between 2.8 Gc/s and 2.9 Gc/s, and provide for the location of the "output cavity pole piece," but these requirements do not restrict the flexibility of the system.

The unit installed for measuring the spurious output signal in this test set was built by Emtech to Cornell specifications, and a block diagram of it is shown in Figure 8. This signal-sampling system can measure signals that are 60 db or more below a fundamental signal of 2 Mw peak power. These signals are two, three, four, five, and six times the

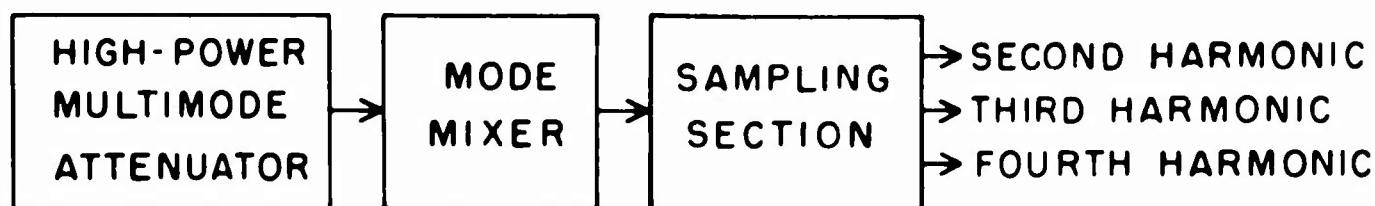


FIGURE 8. Block Diagram of VA-87, Signal-Sampling Device.

fundamental signal and are therefore propagated in the S-band waveguide outside of the usual frequency range (recommended operating range). This means that these signals will propagate in more than one mode.

In the measurement unit installed at Cornell (Figure 8), all the energy passes through the multimode attenuator and is reduced by a known amount. The mode mixer accepts the incoming modal distribution pattern and rearranges it to a known pattern. The sampling section and external band-pass filters provide for frequency separation of the signals as they leave the mode mixer and go to the power-measuring device. The measurement unit is calibrated by launching a known modal distribution at its input and by measuring its insertion loss as a function of frequency for several different mode distributions. The results make it possible to define the insertion loss as a function of frequency (independent of modal distribution). The range of these results defines the accuracy of the system. The unit is as precise as the power-measuring device, since the signal-sampling network is passive.

2. VA-87 Measurements

The Variat VA-87 klystrons are a series of S-band, four-cavity, pulsed klystrons. The only difference between tubes of this series is the

tuning range. The VA-87B can be tuned from 2.7 Gc/s to 2.8 Gc/s ; the VA-87C can be tuned from 2.8 Gc/s to 2.9 Gc/s . The second harmonic of a VA-87B and the second and third harmonics of a VA-87C were measured at the General Electric Microwave Laboratory using a multiprobe signal-sampling network. The second and third harmonics of a VA-87C were measured at Cornell using a mode-mixer signal-sampling network.

a. Multiprobe Measurements^{5,6} on VA-87

A signal-sampling network of the Forrer and Tomiyasu type (multiprobe system) was used to obtain measurements. This network gave modal power information, and the accuracy of the system is ± 1 db . The results shown in Figures 9 and 10 illustrate the variation in spurious output signal level at the second harmonic. The only changes made to the tube were "normal operating parameters" and were well within the specified operating range.

The limited number of measurements made at General Electric of spurious output signals generated by a VA-87C were made under the conditions of synchronous tuning at a fundamental power level of 1.33 Mw . The fundamental frequency was 2.798 Gc/s , which is just below the lower limit of the specified tuning range of 2.8 Gc/s to 2.9 Gc/s . The second harmonic signal level observed was 44.0 db below the fundamental signal level, and the third harmonic 50.4 db .

b. Measurements on the VA-87C

The limited number of measurements of spurious output signals

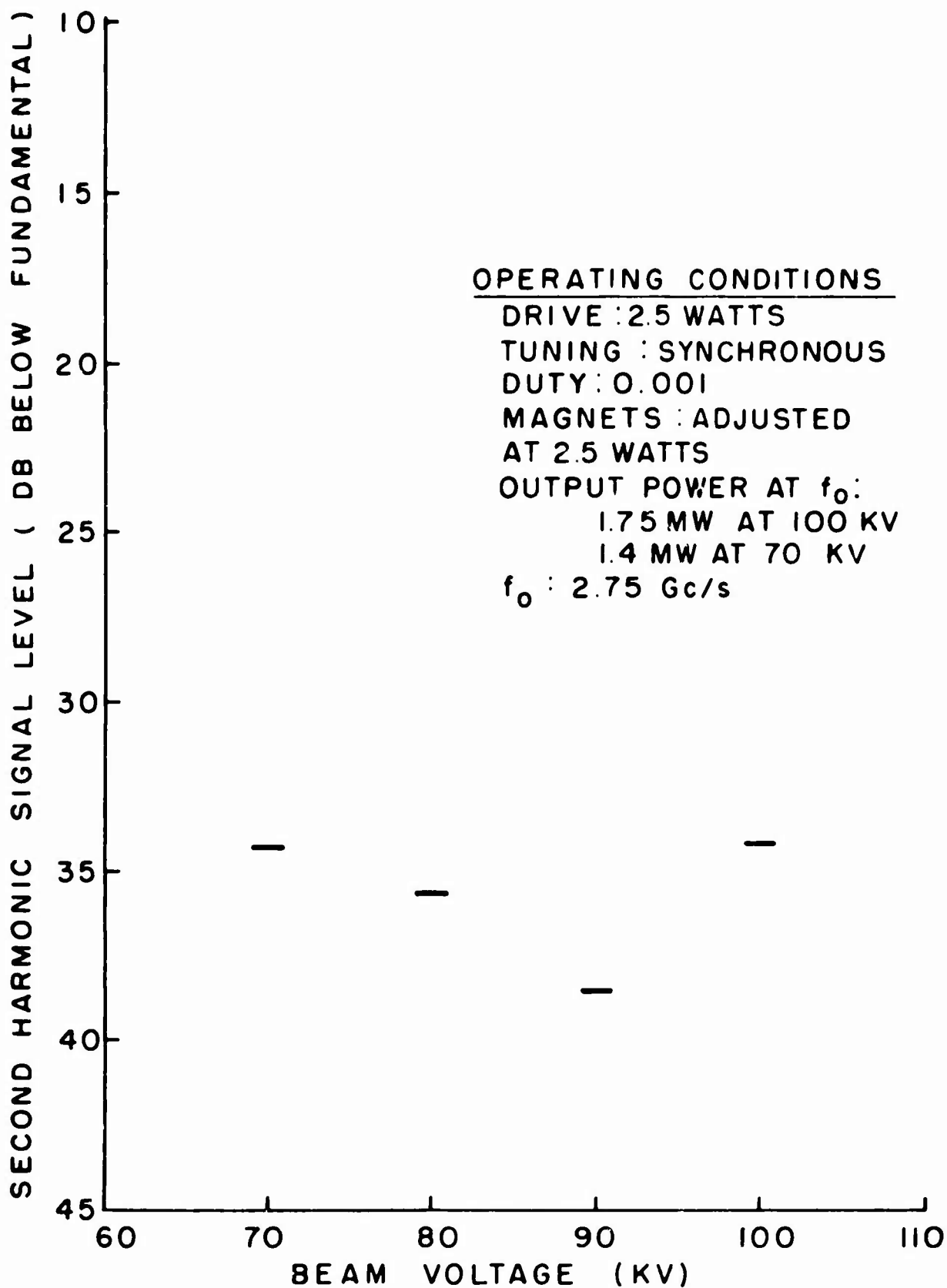


FIGURE 9. Variation of Second Harmonic Power in VA-87B as Beam Voltage Only is Changed.

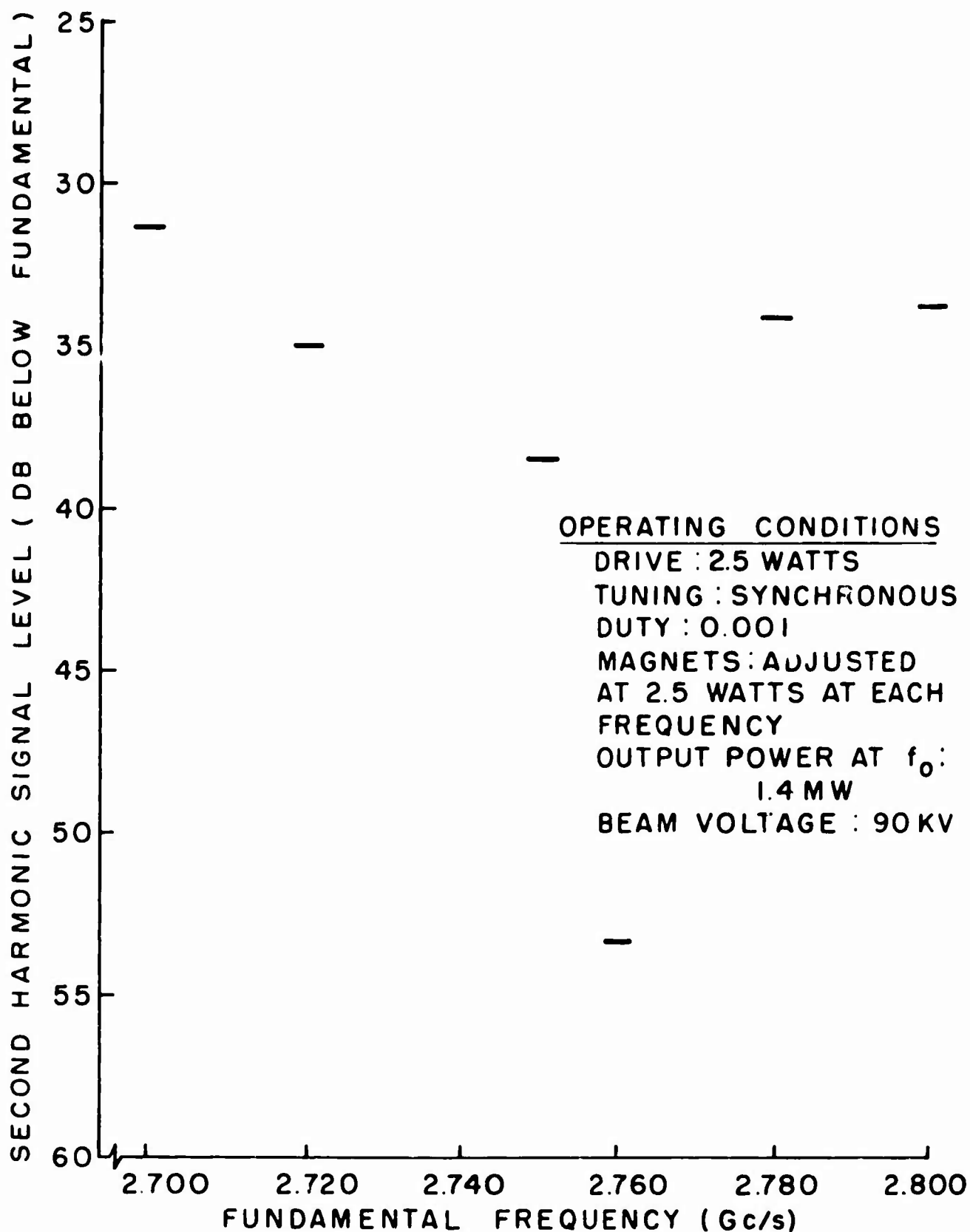


FIGURE 10. Variation of Second Harmonic Power in VA-87B as Fundamental Frequency Only is Changed.

generated by a VA-87C* at Cornell were made under the conditions of synchronous tuning at a fundamental frequency of 2.82 Gc/s and at a beam voltage of 100 kv. The magnets were adjusted at 3.0 w drive to give maximum output. Figure 11 shows the relative change in the fundamental, second harmonic, and third harmonic signals as the r-f drive level is changed. The maximum value of the fundamental signal is 2.1 Mw; the maximum value of the second harmonic is 46 db below this, while the maximum value of the third harmonic is 51 db below this.

C. COMPARISON OF RESULTS

Four sets of data on spurious output signals, taken on four different klystrons, and measured on three different signal sampling networks have been presented. Figures 3 and 4 and Figure 11 show that a relative change of spurious energy in a klystron output cavity is observed as a similar relative change of spurious energy in the klystron's output wave guide. The measurements on the various VA-87 klystrons provide information for a rough comparison between two types of transmission-line signal samplers. The multiprobe unit (G. E.) and the mode mixer unit (C. U.) under similar operating conditions for the VA-87C klystrons give results which compare with each other within the range

*There were two VA-87C klystrons. One VA-87C was modified and became the test instrument. The other VA-87C was not altered. These measurements were made on the unmodified VA-87C.

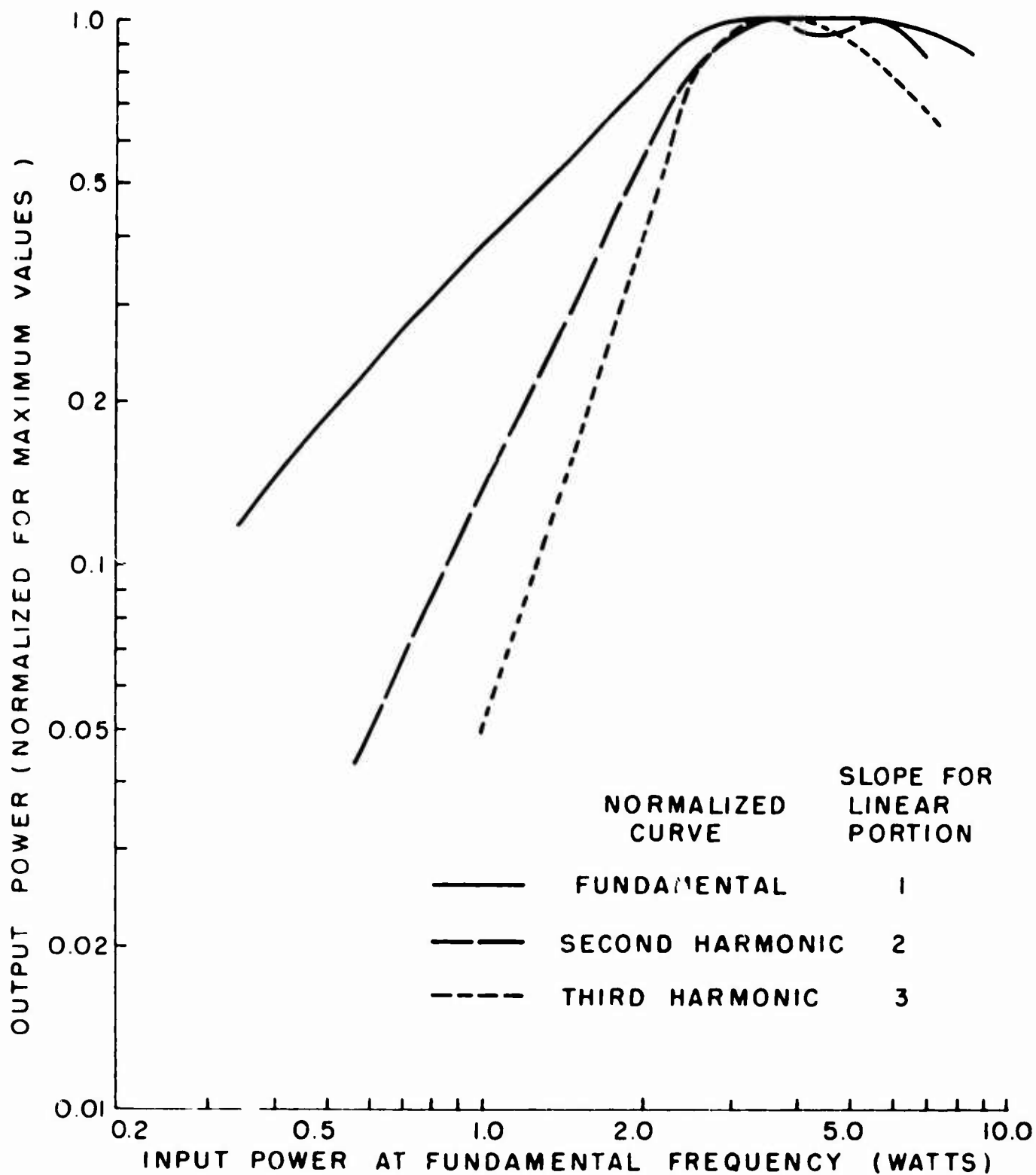


FIGURE 11. Variation of Output Power Level with a Change in Drive Power Only on the VA-87C.

of instrument accuracy, the multiprobe unit being accurate to within ± 1 db and the mode mixer unit to within ± 3 db .

In general, it is easier to obtain absolute power measurements in a transmission-line signal-sampling network than in the output cavity, because the number of independent measurements required in the transmission line are smaller than those required in the cavity. If the aim of a program is to determine the magnitude of the spurious signals on the electron beam, however, the coupling loop of the output cavity to the main output transmission line presents as many unknown coupling-loop coefficients (one for each mode) as the single small coupling loop placed on the SAL-36 did. In other words, if the klystron is considered as a black-box amplifier with an input and output, the measurements can be made in the output line. If the signal levels at various points inside the black box are to be determined, the signals must be sampled at these various points. Furthermore, for a unique solution, enough independent measurements must be made to obtain a set of n algebraic equations with n unknowns.

The measurements on the SAL-36 and VA-87 show that the harmonically related, spurious output signals are generated and coupled out of the cavity into the wave guide at sufficient power levels to reduce the number of systems that can be operated at the same time in the same general geographic location without creating electromagnetic spectrum problems. The signals measured during this investigation were all eventually fed into a dummy load; in an operational system, these signals would have been radiated into the surrounding environment by the system antenna.

IV. PROPOSED METHOD OF REDUCING THE SPURIOUS OUTPUT SIGNALS IN HIGH-POWER KLYSTRONS

The cavity design technique discussed here is a method of reducing the harmonically related, spurious output signals in multicavity klystrons, which solves one problem in electromagnetic compatibility analysis. The problems resulting from spurious emissions from klystrons are illustrated by the results of the measurements on the SAL-36 and VA-87 series klystrons discussed in Section III. There it was seen that even though a spurious signal might be very small when compared to the fundamental, the absolute power level of the spurious signal might be greater than the power level of the carrier of a communications system. For example, a spurious signal which is 50 db below a 2-Mw fundamental signal has an absolute power level of 20 w, which is four times greater than the absolute power level of 5 w (carrier power) used in many microwave point-to-point relay systems today.

This electromagnetic compatibility problem can be solved by eliminating the spurious output signals without degrading the performance of the klystron at the desired frequency of operation. Two different methods may be used to reduce the level of spurious output signals. One method is to suppress the spurious output signals after they have been generated in a nonlinear device and then coupled into the system's transmission line. While this can be done by filters, the method is inefficient, because the addition of filters gives no new information about the operating mechanism of a klystron, and there will always be some insertion loss at the fundamental frequency because of the filters. The other method, used here, is

to improve the design procedure for the devices that generate or amplify microwave signals. The design procedure must take into account the generation of spurious output signals as well as the fundamental output in a high-power microwave tube that would normally be used as the final or power-amplifier stage of a high-power radar transmitter.

In approaching the problem for microwave tubes, one can study either the active portion, i. e. the electron beam and interaction phenomena, or the passive portion, i. e. the tube circuitry. These approaches are not independent, but this study approaches the problem primarily from the passive standpoint.

The specific method used here to effect a reduction in the level of spurious output signals in a klystron is based upon two known facts: (1) All cavities will resonate at many frequencies, and the signals are not necessarily harmonically related. (2) There are many signals on the electron beam, and they are harmonically related. The impedance of a cavity as presented to the electron beam is a function of frequency. The transfer impedance, which relates the amount of energy transferred from the electron beam to the cavity, is high near a resonance and approaches zero away from any of the mode resonances of the cavity. The amount of energy transferred from the electron beam to the cavity increases as this impedance increases; therefore, if the harmonically related spurious signals on the electron beam occur at frequencies away from any mode resonance of the cavity, the impedance presented to the beam at the spurious signal frequency will be low and the transfer of energy from the beam to the cavity will be low. That is, the spurious

signals generated by the velocity modulation of the electron beam will stay on the beam and be absorbed by the collector. Thus, one method of reducing the spurious output signals in klystrons is to develop a cavity design technique that allows for the selective placement of the cavity's higher-order modes. This boundary value problem is the basis of the proposed solution.

The cavity analysis technique used in this study is the normal mode expansion of the given boundary value problem, where Maxwell's equations are to be satisfied. The normal mode expansion will contain all the desired information about the higher-order modes of the cavity. The usual coupling loop, probe, or wave-guide iris does not load the cavity symmetrically with respect to the electron beam. The presence of any of these couplers in a cavity creates problems in the mathematical formulation when higher-order mode information is to be retained because these couplers are unsymmetrical with respect to the electron beam. Therefore, a requirement of the cavity is that it have a coupling scheme that is symmetrical with respect to the electron beam. This requirement, of course, is important only for a cavity that is heavily loaded, as for the input and output cavities of a klystron. It is not important therefore for the intermediate cavities. MacKenzie's work^{1*} did not consider the presence of a coupling mechanism and is, there-

*The method of approach used to develop the design of the symmetrically loaded cavity is based upon MacKenzie's work. Many details of the boundary value problem solution, such as test for series convergence, are not repeated in this thesis.

fore, complete only for intermediate cavity analysis. Since there will be harmonic signals on the beam regardless of the input cavity construction, this study will deal with the design of a klystron output cavity that is heavily loaded, but the analysis technique is the same for an input cavity or any other externally loaded cavity.

A. PROPOSED OUTPUT STRUCTURE

The structure to be considered for this study (Figure 12) is a typical re-entrant, gridless-gap klystron cavity with an axially symmetric output-coupling iris that feeds a coaxial line. Since the klystron's collector is also the center conductor of the output coaxial line, some mechanical and water-cooling problems arise, but they can be solved. Since the majority of high-power radar systems use wave guide as the output transmission line, there will normally be a transition from the tube's coaxial line to the wave guide. This transition may be achieved in several different ways, where the primary electrical consideration is that the transition present a symmetrical load to the output cavity.

The structure used in the analysis is that shown in Figure 13. In going from Figure 12 to Figure 13, the effects of the annular admittance that is associated with the drift tube in the interaction gap and with the top of the cavity at the coupling iris have been removed by assuming that both the drift tube wall and the top of the cavity have zero thickness. The removal of these effects does not influence the basic solution of the mathematical model, because these two effects may each be considered as short transmission lines.

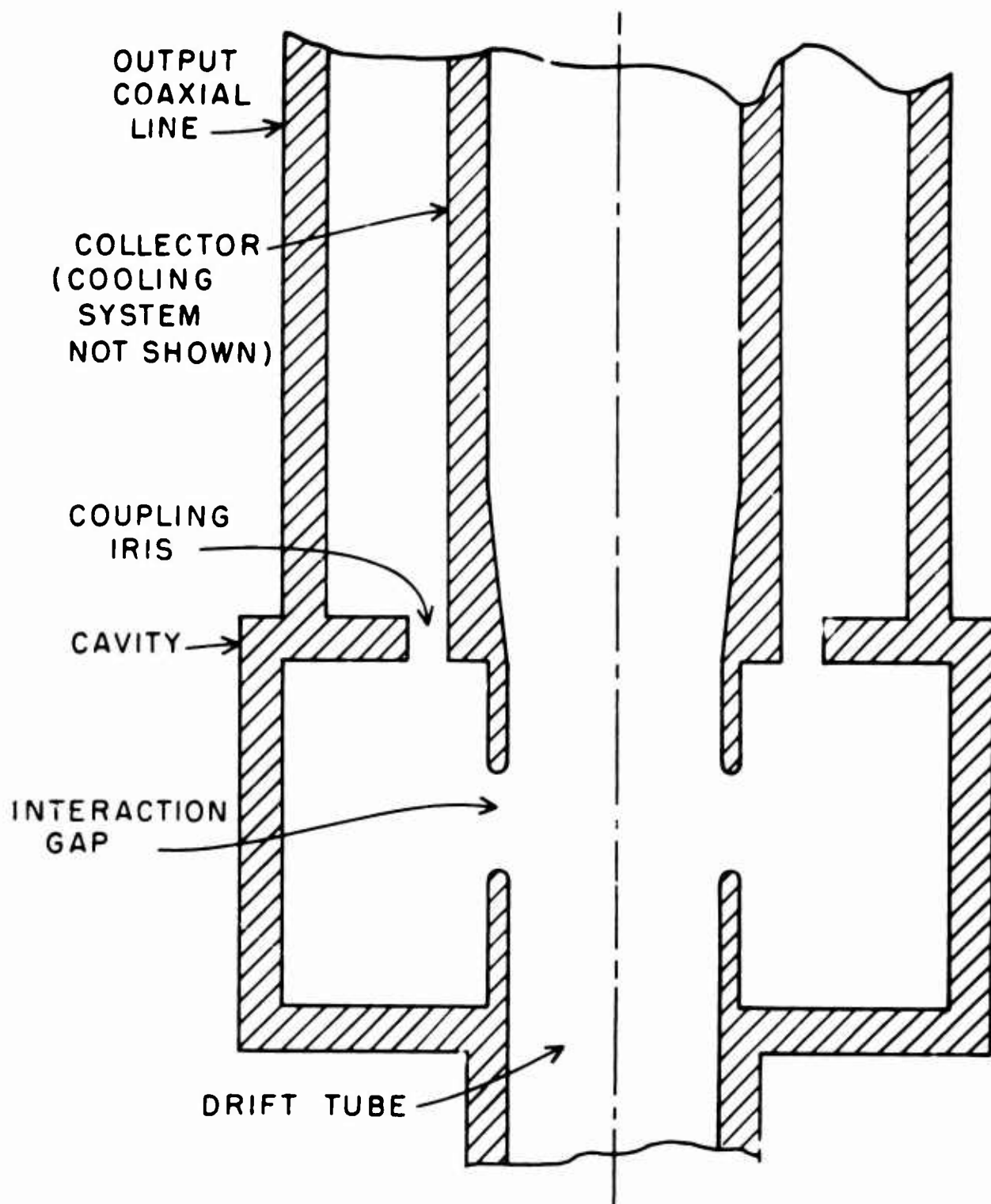


FIGURE 12. Cross Section of Cavity with Symmetrical Output Coupling Iris.

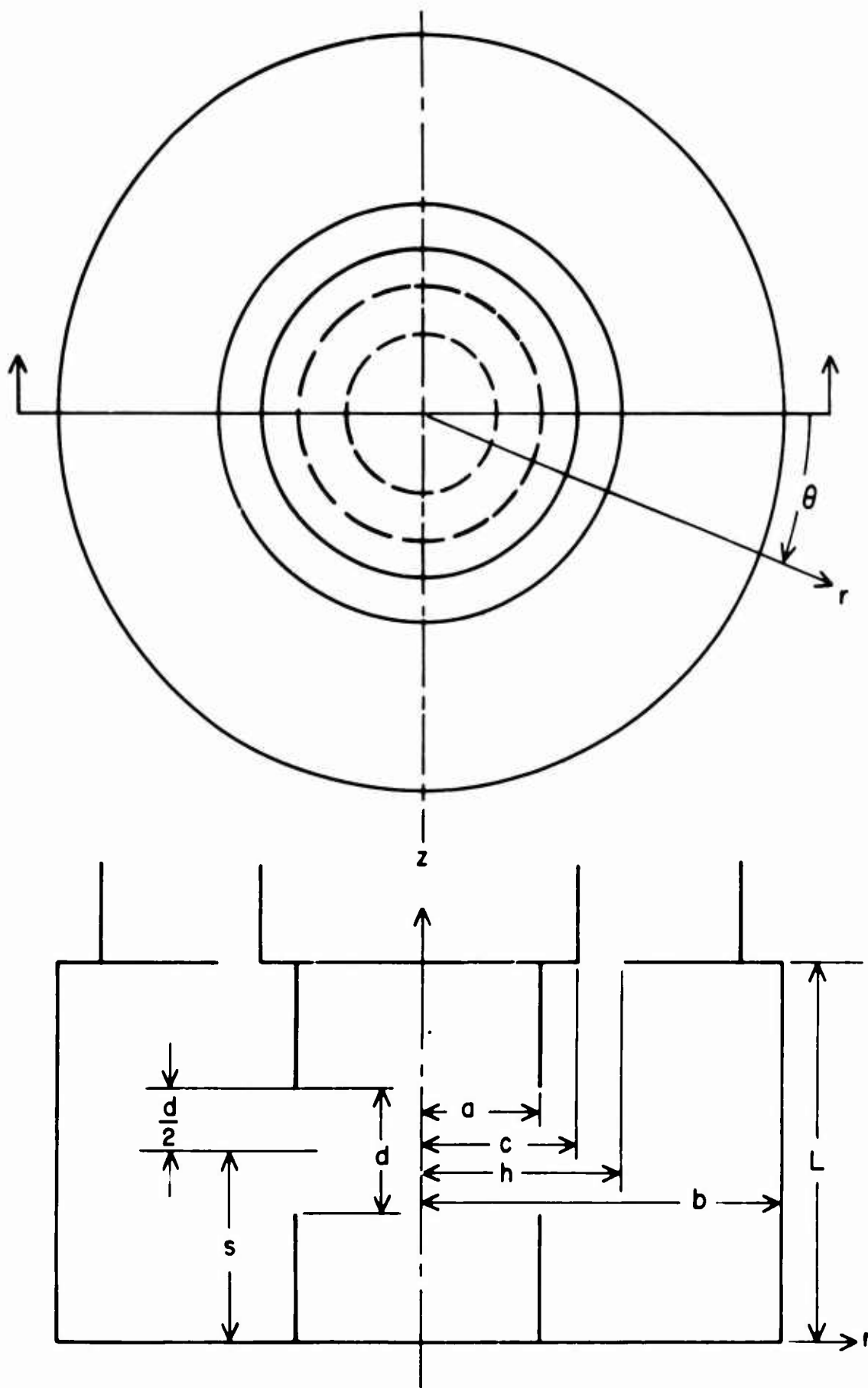


FIGURE 13. Co-ordinate System of Cavity with Symmetrical Coupling Iris.

B. SOLUTION OF THE BOUNDARY VALUE PROBLEM

The normal mode analysis will be used here to obtain a solution to the boundary value problem. From this analysis, an "equivalent" admittance will be defined for each region of the structure and will be expressed in the form of a Fourier (Fourier-Bessel) series. The total admittance function for the structure will be the sum of the admittance functions of all the regions. The absolute value of the total admittance function is a minimum at a cavity mode resonance. This means that the analytical model consists of a sequence of ideal, parallel, resonant, lumped-constant circuits.

For convenience in finding the field expansions, the structure shown in Figure 13 is divided into two cavities, shown in Figures 14 and 15, each of these cavities will in turn be divided into four regions. The regions are:

Region 1 - Interaction cavity (Figure 14), all of the cavity where the range of r is $a < r < b$.

Region 2 - Interaction cavity (Figure 14), all of the cavity where the range of r is $0 < r < a$.

Region 3 - Coupling cavity (Figure 15), all of the cavity where the range of z is $0 < z < L$.

Region 4 - Coupling cavity (Figure 15), the coaxial line, where the range of z is $z \geq L$.

The resultant admittance expressions for each of these regions will be added to give the total admittance function. Since the principle of super-

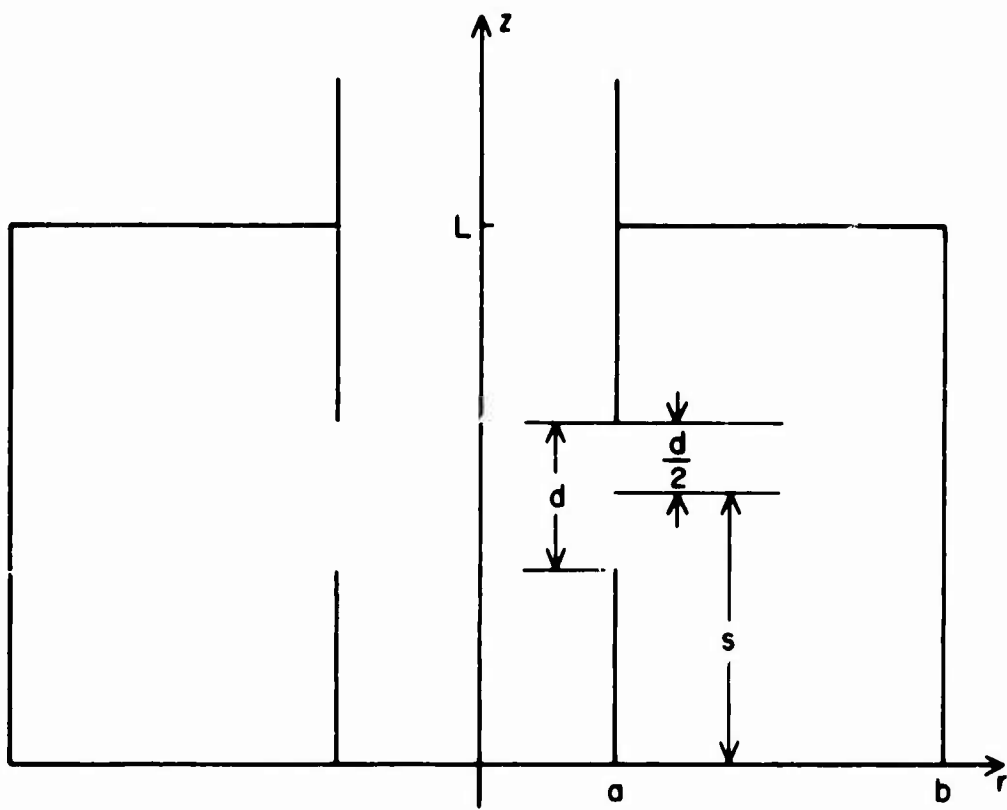


FIGURE 14. Interaction Cavity.

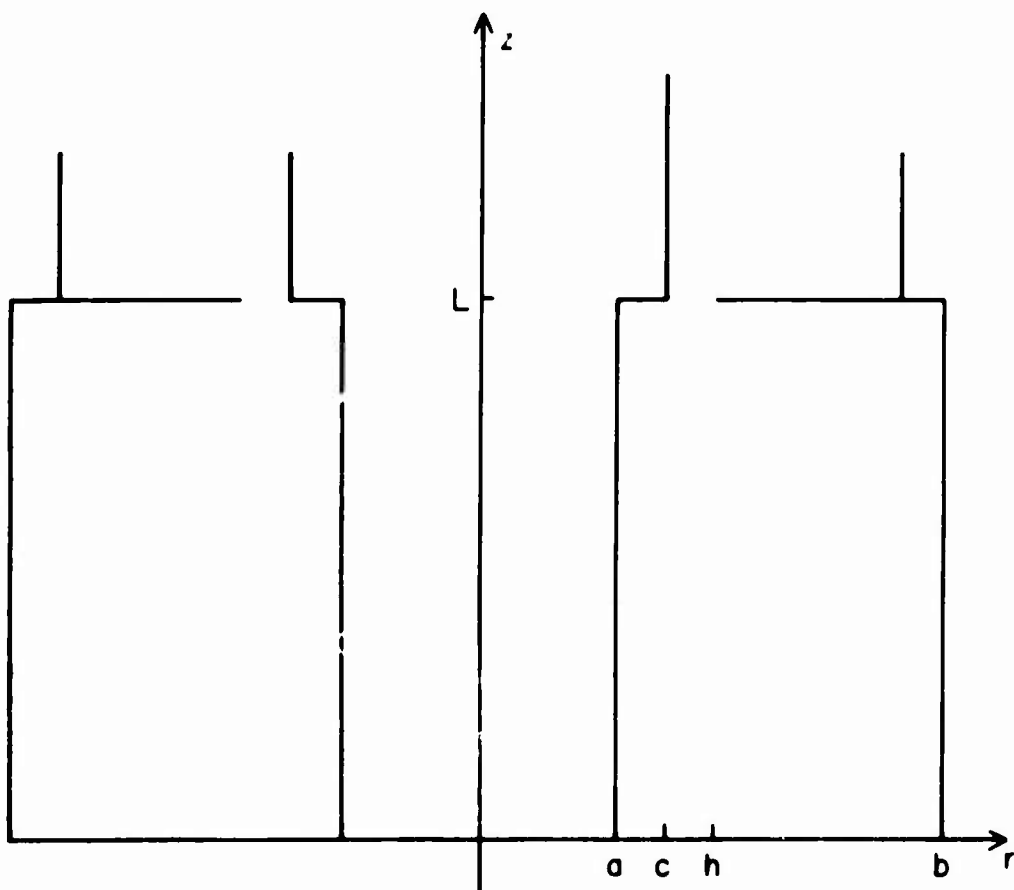


FIGURE 15. Coupling Cavity.

position is valid for Maxwell's equations, it is possible (but certainly not necessary) to follow this convenient procedure.

The procedure used to match the various boundary conditions follows. The field component equations for the cavities shown in Figures 14 and 15 are determined; then since E_z of Figure 15 (Region 3) is zero at $r = a$, the E fields which must be matched across the interaction gap are the E_z field components from Region 1 and Region 2 at $r = a$. Similarly at the coupling iris, the E fields which must be matched at $z = L$ are the E_r components of Region 3 and 4, because the E_r field component of Region 2 is zero at $z = L$. The field component equations for Regions 2 and 3 are then added. The H-field components are then matched at the interaction gap and the coupling iris by defining a gap voltage and gap current and determining an "equivalent" admittance. At $r = a$, we can determine Y_{g1} for Region 1, and Y_g for Regions 2 and 3. At $z = L$, we can determine Y_{c1} for Region 4, and Y_c for Regions 2 and 3. The effect of the system load on the electron beam is shown in these admittances through the H field component equations. The terms Y_g , Y_{g1} , Y_c , and Y_{c1} are defined in Equations (17), (21), (26), and (18) respectively.

The "equivalent" admittance functions of the interaction and coupling cavities can then be combined to form a set of two equations with two unknowns. Solutions to this set of equations will yield the resonant frequencies for the structure. The first zero or eigen value of this set of equations will be the desired fundamental resonance.

The normal mode definitions of the coaxial line are used in this study. The usual fundamental mode of oscillation of the cavity is the TM_{010} mode, where the subscripts refer to spatial variation of the field in the θ , r , and z directions respectively. In order that the desired signal produced by the interaction of the active (electron beam) portion and the passive (tube circuitry) portion of the microwave tube be capable of reaching the system load (antenna), neither E_z nor E_r can be identically zero. Thus, for a symmetrical mode (no variation in the θ direction) to be capable of transferring a useful signal from the electron beam of the klystron to the system load, the mode must be of the TM type and not of the TE type. This analysis assumes symmetry in the θ direction, since, in theory, this assumption is valid for the operation of these cavities. The conductivity of the metal walls is assumed infinite, and the drift tube wall and the top of the cavity ($z = L$) are assumed to have zero thickness. These assumptions are those usually made, and are good approximations for a symmetrically loaded cavity that is physically realizable.

The general field expressions for Regions 1, 2, 3, and 4 given below in Equations (4a) and (4b) are derived from the wave equation of the form

$$\nabla^2 E = \gamma_0^2 E \quad . \quad (3)$$

The general field expressions for TM_{onm} modes are

$$E_z = [A_m J_0(kr) + B_m N_0(kr)] \cos \beta_z z e^{j\omega t} \quad ,$$

$$\begin{aligned}
E_r &= \frac{\beta_z}{k} [A_m J_1(kr) + B_m N_1(kr)] \sin \beta_z z e^{j\omega t} , \\
H_\theta &= j \frac{\omega \epsilon}{k} [A_m J_1(kr) + B_m N_1(kr)] \cos \beta_z z e^{j\omega t} , \\
E_\theta &= H_r = H_z = 0 ,
\end{aligned} \tag{4a}$$

where

$$k^2 = -\beta_z^2 - \gamma_0^2 \quad \text{and} \quad \gamma_0 = j\omega \sqrt{\mu\epsilon} .$$

The general field expressions for the coaxial line TEM mode which will propagate in Regions 3 and 4 are

$$\begin{aligned}
E_r &= \sqrt{\frac{\mu}{\epsilon}} \frac{K}{2\pi r} e^{j(\omega t - \beta z)} , \\
H_\theta &= \frac{K}{2\pi r} e^{j(\omega t - \beta z)} ,
\end{aligned} \tag{4b}$$

where $\beta = \omega \sqrt{\mu\epsilon}$.

As the first step in the solution of this boundary value problem, a field will be assumed at the interaction gap (Figure 16) and also at the coupling iris (Figure 17) of the cavity. These fields are of the same form as those found in the TEM mode and are similar to the higher order TM_{omn} mode fields. They thus, provide a reasonable approximation of the actual fields at resonance, but are not as good approximations away from resonance. Since the location of the higher-order

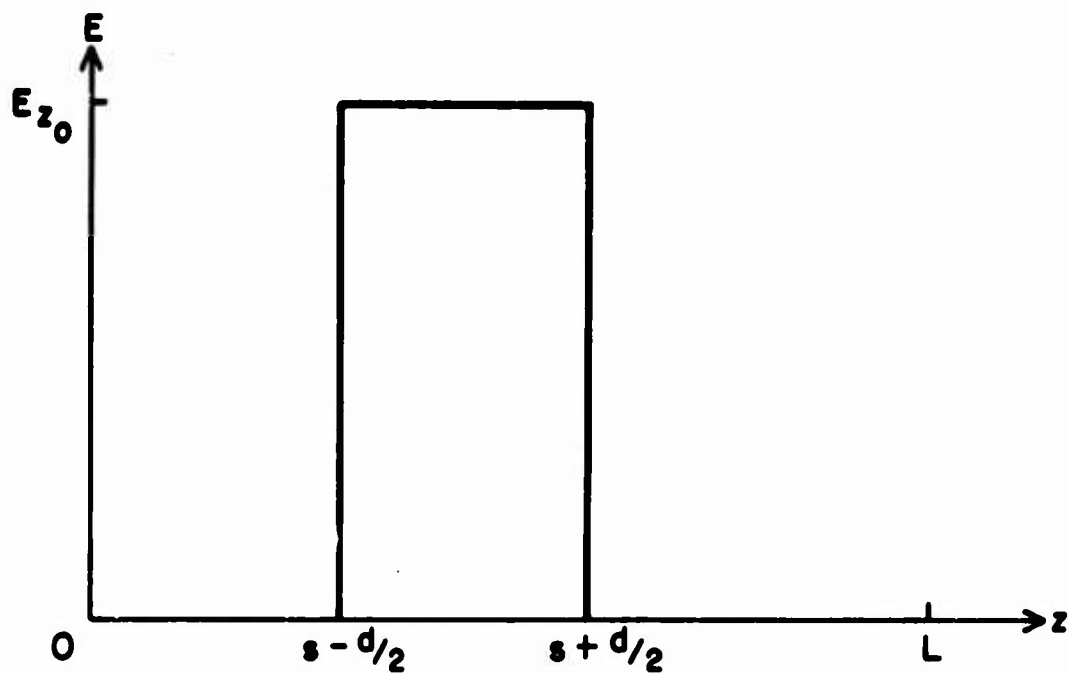


FIGURE 16. Assumed Interaction Gap Field ($r = a$).

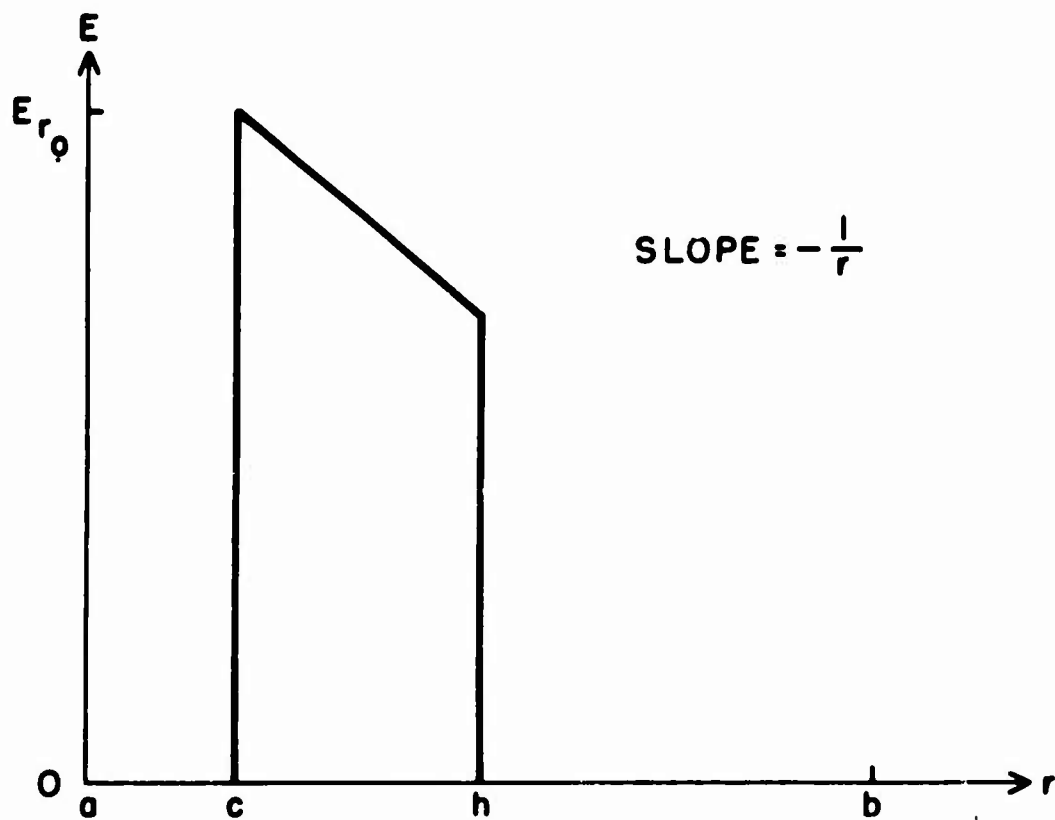


FIGURE 17. Assumed Coupling Iris Field ($z = L$).

resonances (zeros of the total admittance function) is the primary purpose of this analysis, these assumptions are not expected to alter the solution of the problem severely.

The E field boundary conditions that must be satisfied by the solution of this problem are:

$$\begin{aligned}
 E_r|_{z=0} &= 0, \\
 E_r|_{z=L} &= \begin{cases} 0 & a < r < c \\ \frac{c E_{r0}}{r} e^{j\omega t} & c < r < h \\ 0 & h < r < b \end{cases}, \\
 E_z|_{r=b} &= 0, \\
 E_z|_{r=a} &= \begin{cases} 0 & 0 < z < s - \frac{d}{2} \\ E_{z0} e^{j\omega t} & s - \frac{d}{2} < z < s + \frac{d}{2} \\ 0 & s + \frac{d}{2} < z < L \end{cases}. \quad (5)
 \end{aligned}$$

1. Analysis for Region 1

In the field component equations determined for Region 1 (interaction cavity), all field quantities associated with Region 1 are designated by a subscript or superscript 1. The boundary conditions for the interaction cavity (Figure 14) are

$$E_{r_1} \Big|_{\substack{z=0 \\ z=L}} = 0 ,$$

$$E_{z_1} \Big|_{r=b} = 0 ,$$

$$E_{z_1} \Big|_{r=a} = \begin{cases} 0 & 0 < z < s - \frac{d}{2} \\ E_{z_0} e^{j\omega t} & s - \frac{d}{2} < z < s + \frac{d}{2} \\ 0 & s + \frac{d}{2} < z < L \end{cases} . \quad (6)$$

From Equations (4) and (6) the Region 1 field component equations are found to be

$$E_{z_1} = \left\{ \frac{d D_0(k_0 r)}{L D_0(k_0 a)} + \sum_{m=1}^{\infty} \frac{4 \cos \beta_{z_m}^{(1)} s \sin \beta_{z_m}^{(1)} \frac{d}{2} D_0(k_m r) \cos \beta_{z_m}^{(1)} z}{L \beta_{z_m}^{(1)} D_0(k_m a)} \right\} E_{z_0} , \quad (7)$$

$$E_{r_1} = \sum_{m=1}^{\infty} \frac{4 \cos \beta_{z_m}^{(1)} s \sin \beta_{z_m}^{(1)} \frac{d}{2} D_1(k_m r) \sin \beta_{z_m}^{(1)} z}{L k_m D_0(k_m a)} E_{z_0} , \quad (8)$$

$$H_{\theta_1} = j\omega\epsilon \left\{ \frac{d D_1(k_0 r)}{k_0 L D_0(k_0 a)} + \sum_{m=1}^{\infty} \frac{4 \cos \beta_{z_m}^{(1)} \sin \beta_{z_m}^{(1)} \frac{d}{2} D_1(k_m r) \cos \beta_{z_m}^{(1)} z}{L k_m \beta_{z_m}^{(1)} D_0(k_m a)} \right\} E_{z_0}, \quad (9)$$

where in Equations (7), (8), and (9),

$$k_m^2 = -(\beta_{z_m}^{(1)})^2 - \gamma_0^2,$$

$$k_0 = \omega \sqrt{\mu\epsilon}, \quad \beta_{z_m}^{(1)} = \frac{m\pi}{L},$$

$$D_0(k_m r) = N_0(k_m b) J_0(k_m r) - J_0(k_m b) N_0(k_m r),$$

$$D_1(k_m r) = N_0(k_m b) J_1(k_m r) - J_0(k_m b) N_1(k_m r).$$

2. Analysis for Region 3

In the field component equations determined for Region 3 (Figure 15), all field quantities associated with Region 3 are designated by a subscript or superscript 3. The boundary conditions for the coupling cavity are

$$E_{z_3} \bigg|_{\substack{r=a \\ r=b}} = 0, \quad (10)$$

$$E_{r3} \Big|_{z=L} = \begin{cases} 0 & a < r < c \\ \frac{c E_{m0}}{r} & c < r < h \\ 0 & h < r < b \end{cases}$$

$$E_{r3} \Big|_{z=0} = 0 \quad (10)$$

From Equations (4) and (10), the Region 3 field component equations are found to be

$$E_{z3} = - \sum_{m=1}^{\infty} \frac{c \pi^2 \lambda_m^2 N_o^2(\lambda_m a) [D_o(\lambda_m h) - D_o(\lambda_m c)] D_o(\lambda_m r) \cos \beta_{zm}^{(3)} z}{2 \sin \beta_{zm}^{(3)} L [N_o^2(\lambda_m a) - N_o^2(\lambda_m b)] \beta_{zm}^{(3)}} E_{r0} \quad (11)$$

$$E_{r3} = \frac{c \ln \frac{h}{c} e^{j\beta_{z0}^{(3)}(L-z)}}{r \ln \frac{b}{a}} E_{r0}$$

$$- \sum_{m=1}^{\infty} \frac{c \pi^2 \lambda_m^2 N_o^2(\lambda_m a) [D_o(\lambda_m h) - D_o(\lambda_m c)] D_1(\lambda_m r) \sin \beta_{zm}^{(3)}}{2 \sin \beta_{zm}^{(3)} L [N_o^2(\lambda_m a) - N_o^2(\lambda_m b)]} E_{r0} \quad (12)$$

$$H_{\theta_3} = \sqrt{\frac{\epsilon}{\mu}} \frac{c \ln \frac{h}{c} e^{j\beta_{z_0}^{(3)}(L-z)}}{r \ln \frac{b}{a}} E_{r_0}$$

$$-j\omega \epsilon \sum_{m=1}^{\infty} \frac{c \pi^2 \lambda_m N_o^2(\lambda_m a) [D_o(\lambda_m h) - D_o(\lambda_m c)] D_1(\lambda_m r) \cos \beta_{z_m}^{(3)} z}{2 \beta_{z_m}^{(3)} \sin \beta_{z_m}^{(3)} L [N_o^2(\lambda_m a) - N_o^2(\lambda_m b)]} E_{r_0} \quad (13)$$

where for Equations (11), (12), and (13)

$$(\beta_{z_m}^{(3)})^2 = -\lambda_m^2 - \gamma_o^2 ; \quad \beta_{z_o}^{(3)} = \omega \sqrt{\mu \epsilon} \quad ..$$

$$D_o(\lambda_m r) = N_o(\lambda_m b) J_o(\lambda_m r) - J_o(\lambda_m b) N_o(\lambda_m r) \quad .$$

Note that $D_o(\lambda_m b) \equiv 0$ and that λ_m is the m^{th} root of $D_o(\lambda_m a) = 0$ and also that

$$D_1(\lambda_m r) = N_o(\lambda_m b) J_1(\lambda_m r) - J_o(\lambda_m b) N_1(\lambda_m r) \quad .$$

3. Analysis for Region 1 and 3

The field component equations and boundary conditions for the various regions have been developed so that

$$E_{r_1} \Big|_{z=L} = 0$$

and

$$E_{z_3} \Big|_{r=a} = 0$$

This is done in order to simplify the process of matching the E field boundary conditions for the structure shown in Figure 13. The expression $E_{r_1} \Big|_{z=L} = 0$ is an obvious boundary condition for the structures shown in Figure 15, likewise $E_{z_3} \Big|_{r=a} = 0$ corresponds to Figure 14.

Next, the "equivalent" admittance function for Regions 1 and 3 must be obtained together because $Y = f(I)$ and $I = f(H_\theta)$. The field component H_θ has a contribution from both the interaction and coupling cavities at both the interaction gap and the coupling iris. It is this H_θ field component which relates the effect of the system load to the electron beam (drift tube) and vice versa. The total field component equations for Regions 1 and 3 are given by adding the following equations:

$$E_z = \text{Equation (7)} + \text{Equation (11)} \quad , \quad (14)$$

$$E_r = \text{Equation (8)} + \text{Equation (12)} \quad , \quad (15)$$

$$H_\theta = \text{Equation (9)} + \text{Equation (13)} \quad . \quad (16)$$

The interaction gap voltage V_g , the interaction gap current I_g , the interaction gap admittance Y_g , the coupling iris voltage V_c , the coupling iris current I_c , and coupling iris admittance Y_c will be determined from

Equations (14), (15), and (16). The resultant equations for Y_g and Y_c are:

$$\begin{aligned}
 Y_g = & -j\omega\epsilon \left(\frac{2\pi a}{d^2} \right) \left\{ \frac{d^2 D_1(k_o a)}{k_o L D_o(k_o a)} \right. \\
 & + \frac{2c \ln \frac{h}{c} \cos \beta_{z_o}^{(3)} s \sin \beta_{z_o}^{(3)} \frac{d}{2}}{a \beta_{z_o}^{(3)2} \ln \frac{b}{a} \sin \beta_{z_o}^{(3)} L} \left(\frac{E_{r_o}}{E_{z_o}} \right) \\
 & + \frac{8L}{\pi^2} \sum_{m=1}^{\infty} \frac{D_1(k_m a) \left[\cos \beta_{z_m}^{(1)} s \sin \beta_{z_m}^{(1)} \frac{d}{2} \right]^2}{m^2 k_m D_o(k_m a)} \\
 & \left. - \pi^2 \sum_{m=1}^{\infty} \frac{c \lambda_m N_o^2(\lambda_m a) [D_o(\lambda_m h) - D_o(\lambda_m c)] \cos \beta_{z_m}^{(3)} s \sin \beta_{z_m}^{(3)} \frac{d}{2} D_1(\lambda_m a)}{\beta_{z_m}^{(3)2} [N_o^2(\lambda_m a) - N_o^2(\lambda_m b)] \sin \beta_{z_m}^{(3)} L} \left(\frac{E_{r_o}}{E_{z_o}} \right) \right\}
 \end{aligned}
 \tag{17}$$

where

$$I_g = \int_A \frac{H_\theta \big|_{r=a}}{d} dA$$

$$V_g = - \int_0^L E_z \big|_{r=a} dz$$

and

$$Y_g = \frac{I_g}{V_g}$$

$$Y_c = 2\pi \sqrt{\frac{\epsilon}{\mu}} \frac{1}{\ln \frac{b}{a}}$$

$$\begin{aligned}
 & + j\omega\epsilon \left[\frac{2\pi}{c(h-c) \ln \frac{h}{c}} \right] \left\{ \frac{d \int_c^h r D_1(k_0 r) dr}{L k_0 D_0(k_0 a)} \left(\frac{E_{z_0}}{E_{r_0}} \right) \right. \\
 & + \frac{4}{\pi} \sum_{m=1}^{\infty} \frac{(-1)^m \cos \beta_{z_m}^{(1)} \sin \beta_{z_m}^{(1)} \frac{d}{2} \int_c^h r D_1(k_m r) dr}{m k_m D_0(k_m a)} \left(\frac{E_{z_0}}{E_{r_0}} \right) \\
 & \left. - \frac{\pi^2}{2} \sum_{m=1}^{\infty} \frac{c \lambda_m N_0^2(\lambda_m a) [D_0(\lambda_m h) - D_0(\lambda_m c)] \cos \beta_{z_m}^{(3)} L \int_c^h r D_1(\lambda_m r) dr}{\beta_{z_m}^{(3)} [N_0^2(\lambda_m a) - N_0^2(\lambda_m b)] \sin \beta_{z_m}^{(3)} L} \right\} \quad (18)
 \end{aligned}$$

where

$$I_c = \int_A \frac{H_\theta|_{z=L}}{h-c} dA$$

$$V_c = \int_a^b E_r|_{z=L} dr$$

and

$$Y_c = \frac{I_c}{V_c}$$

For convenience in using these expressions in the subsequent discussion, each major term will be assigned a letter, for example, from Equation (17)

$$Y_g = A_1 + A_2 \left(\frac{E_{r_o}}{E_{z_o}} \right) + A_3 - A_4 \left(\frac{E_{r_o}}{E_{z_o}} \right) \quad (19)$$

The terms listed in Equations (17) and (19) are in the same order. Likewise from Equation (18)

$$Y_c = B_2 + B_1 \left(\frac{E_{z_o}}{E_{r_o}} \right) + B_3 \left(\frac{E_{z_o}}{E_{r_o}} \right) - B_4 \quad (20)$$

4. Analysis for Region 2

The "equivalent" admittance associated with Region 2 (inside the drift tube) is an inner storage admittance. It may be determined in the same manner that Y_g and Y_c have been found; however, the inner storage admittance has been calculated by C. C. Wang.⁷ In terms of the notation used here, the inner storage admittance Y_{g_1} (i. e., Region 2) is

$$Y_{g_1} = j \frac{2\pi a}{d} \sqrt{\frac{\epsilon}{\mu}} \left\{ \frac{J_1(k_o a)}{J_o(k_o a)} - \frac{2a}{d} \sum_{m=1}^{\infty} \frac{k_m a}{\xi^3} \left[1 - e^{-\frac{d}{a} \xi} \right] \right\} \quad (21)$$

where $\xi^2 = R_m^2 - (k_m a)^2$ and R_m is the m^{th} root of J_o . The assumptions made by Wang are used in this study. However, there is the

additional restriction that $k_m a < 2.405$ in order to eliminate modes that can propagate down the drift tube in the z direction, i.e., propagating modes of a circular wave guide. Wang also points out that, to be perfectly safe, one should have $k_m a < 1.84$ so that the circular wave guide TE_{11} mode will not propagate, since any dissymmetry may excite the mode. Neither of these restrictions gives any real difficulty, because no klystron would be operated with its fundamental frequency in this region. The restriction ($k_m a < 2.405$) does determine an upper frequency for a klystron above which the total admittance function is not a good approximation. This frequency limit is usually above the fourth harmonic of the fundamental frequency.

Again for convenience, Y_{g1} is rewritten from Equation (21) as

$$Y_{g1} = A_5 + A_6 \quad (22)$$

Here too the terms of Equations (21) and (22) are listed in the same order.

5. Analysis of Region 4

The "equivalent" admittance associated with Region 4 (Figure 18) is determined in the same manner as Y_g , Y_c , and Y_{g1} . The general field equations are the same as those for the cavity Equations (3) and (4). The boundary conditions of the coaxial line are

$$E_z \Big|_{\substack{r=c \\ r=\rho}} = 0 \quad (23)$$

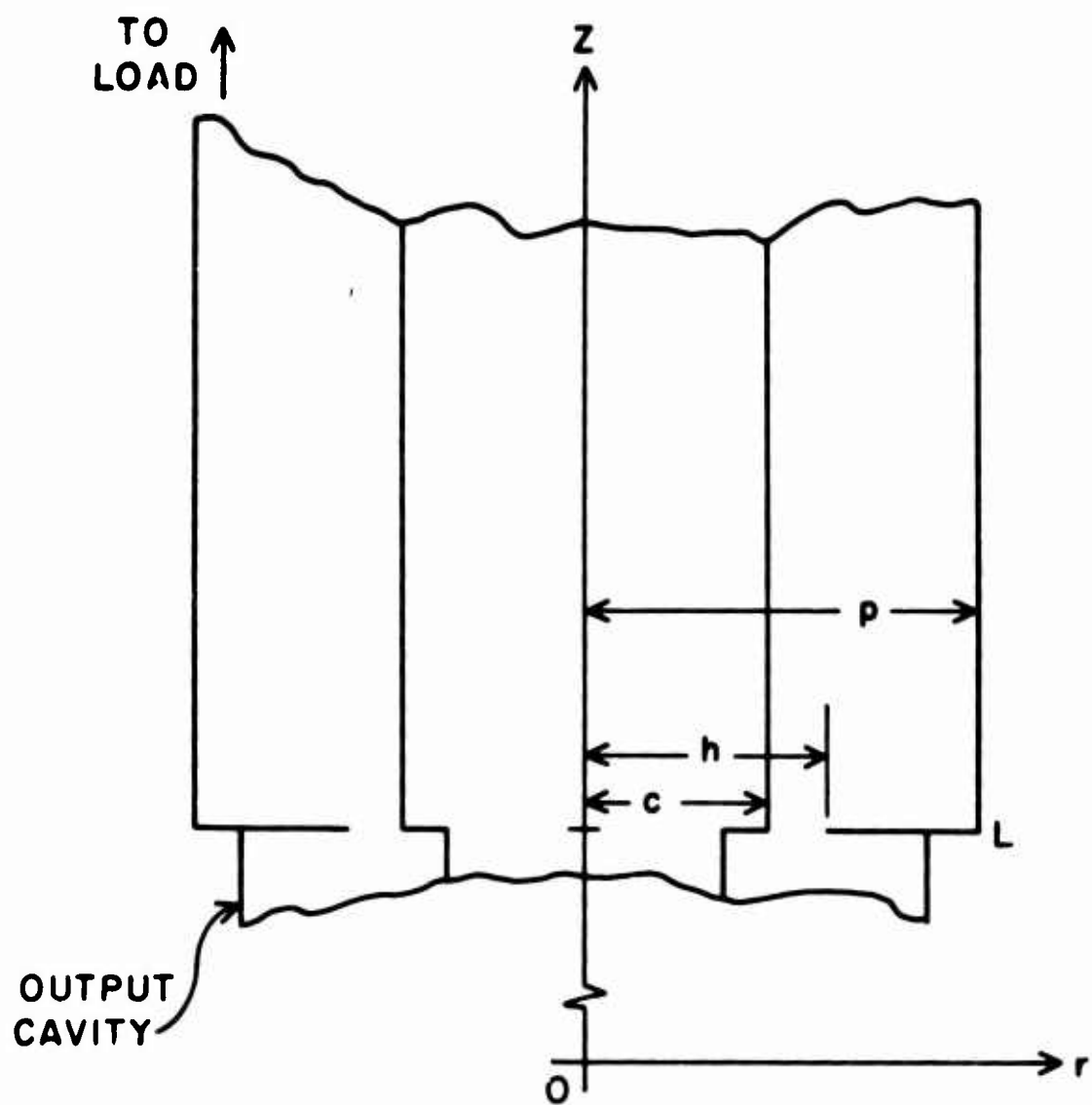


FIGURE 18. Coaxial Output Line.

$$E_r|_{z=L} = \begin{cases} \frac{c E_{r_0}}{r} & c < r < h \\ 0 & h < r < \rho \end{cases} \quad (23)$$

From Equations (4) and (23), the field component equations are

$$E_z = -\frac{\pi}{2} \sum_{m=1}^{\infty} \frac{c a_m^2 N_o^2(a_m c) D_o(a_m h) \cos \beta_m z D_o(a_m r)}{\beta_m [N_o^2(a_m c) - N_o^2(a_m \rho)] \sin \beta_m L} E_{r_0} ,$$

$$E_r = -\frac{\pi}{2} \sum_{m=1}^{\infty} \frac{c a_m N_o^2(a_m c) D_o(a_m h) \sin \beta_m z D_1(a_m r)}{[N_o^2(a_m c) - N_o^2(a_m \rho)] \sin \beta_m L} E_{r_0} ,$$

and

$$H_\theta = -j\omega\epsilon \frac{\pi}{2} \sum_{m=1}^{\infty} \frac{c a_m N_o^2(a_m c) D_o(a_m h) D_1(a_m r) \cos \beta_m z}{\beta_m [N_o^2(a_m c) - N_o^2(a_m \rho)] \sin \beta_m L} E_{r_0} , \quad (24)$$

where

$$D_o(a_m r) = N_o(a_m \rho) J_o(a_m r) - J_o(a_m \rho) N_o(a_m r) ,$$

$$D_o(a_m \rho) \equiv 0 ,$$

$$D_o(a_m c) = 0 , \text{ when } a_m \text{ is the } m^{\text{th}} \text{ root,}$$

$$\beta_m^2 = -a_m^2 + \omega^2 \mu \epsilon ,$$

and for the $m=0$ term of these series (coaxial TEM mode), the resultant field expressions are

$$E_r = \frac{c \ln \frac{h}{c}}{r \ln \frac{\rho}{c}} e^{j\beta(L-z)} E_{r_0} ,$$

$$H_\theta = \sqrt{\frac{\epsilon}{\mu}} \frac{c \ln \frac{h}{c}}{r \ln \frac{\rho}{c}} e^{j\beta(L-z)} E_{r_0} . \quad (25)$$

The "equivalent" admittance for the perfectly loaded coaxial line (Region 4) is found from Equations (24) and (25). It is

$$Y_{c_1} = -2\pi \sqrt{\frac{\epsilon}{\mu}} \frac{1}{\ln \frac{\rho}{c}} - j\omega\epsilon \left(\frac{\pi^3}{(h-c) \ln \frac{h}{c}} \right) \sum_{m=1}^{\infty} \frac{a_m N_o^2(a_m c) D_o(a_m h) \cos \beta_m L \int_c^h r D_1(a_m r) dr}{\beta_m [N_o^2(a_m c) - N_o^2(a_m \rho)] \sin \beta_m L} , \quad (26)$$

where

$$V_{c_1} = \int_c^\rho E_r \Big|_{z=L} dr ,$$

$$I_{c_1} = \int_A \frac{H_\theta \Big|_{z=L}}{h-c} dA ,$$

and

$$Y_{c_1} = \frac{I_{c_1}}{V_{c_1}} .$$

Again as before, Y_{c_1} is rewritten from Equation (26) as

$$Y_{c_1} = -B_5 - B_6 . \quad (27)$$

6. Analysis of Total Admittance Function

The admittance functions from Regions 1 and 3, Region 2, and Region 4 may now be combined to form the total admittance function. In Regions 1 and 3 and Region 2, the relationship between the magnetic fields is

$$H_{\theta}|_{\text{Region 2}} = -H_{\theta}|_{\text{Regions 1 and 3}}$$

Thus one of the two equations for resonance is

$$Y_g + Y_{g_1} = 0 \quad ;$$

or from Equations (19) and (22),

$$A_1 + A_2 \left(\frac{E_{r_o}}{E_{z_o}} \right) + A_3 - A_4 \left(\frac{E_{r_o}}{E_{z_o}} \right) + A_5 + A_6 = 0 \quad . \quad (28)$$

In Regions 1 and 3 and Region 4, the relationship between the respective magnetic fields is

$$H_{\theta}|_{\text{Region 4}} = -H_{\theta}|_{\text{Regions 1 and 3}} \quad .$$

Thus, the second resonance equation is

$$Y_c + Y_{c_1} = 0 \quad ;$$

or from Equations (20) and (27),

$$B_1 \left(\frac{E_{z_o}}{E_{r_o}} \right) + B_2 + B_3 \left(\frac{E_{z_o}}{E_{r_o}} \right) - B_4 - B_5 - B_6 = 0 \quad . \quad (29)$$

If $b/a = \rho/c$, then $B_2 - B_5 = 0$; that is, the characteristic impedance of the output coaxial line and the coupling cavity are equal. Through the remainder of this thesis, it is assumed that $a\rho = bc$.

7. Special-Case Checks of Solution

There are several special-case checks which may be used to determine necessary, but not sufficient, conditions for ascertaining the validity of Equations (28) and (29) as a solution to the boundary value problem. The three cases discussed can be more easily visualized from Figure 13.

a. Case 1

If $c = h$, then $Y_c = Y_{c_1} = 0$ and the cavity resonances are determined by

$$Y_{g_1} + Y_g = 0.$$

This is the "resonance equation" for the interaction cavity or MacKenzie's cavity.¹ The nomenclature used in this study is slightly different from that used by MacKenzie, but the equation for the interaction cavity resonance is the same. Thus, the solution as presented in Equations (28) and (29) is consistent with previous work.

b. Case 2

If $d = 0$, then $Y_g = 0$ and Y_{g_1} is not defined, because in the formulation of the problem to determine Y_{g_1} , it is assumed that $d \neq 0$. Thus, the resonance equation becomes

$$Y_c + Y_{c_1} = 0,$$

as expected. If in addition, $\rho = h$, the equations now express a jump discontinuity between two coaxial lines where the characteristic impedance of the coaxial lines is the same if $a/b = c/\rho$ and is different if $a/b \neq c/\rho$.

c. Case 3

If $d = 0$, $a = c$, and $b = p = h$, the equation,

$$Y_c + Y_{c_1} = 0$$

expresses the admittance of a short-circuited coaxial line as viewed from the point $z = L$ (Y_g and Y_{g_1} are still equal to zero as in Case 2).

Thus, all the special-case checks are satisfied and the solution of the problem as given in Equations (28) and (29) is at least a solution for these special configurations. The complete check on the validity of this solution would be determined when a comparison of analytical and experimental results is made. Some of the necessary laboratory equipment required to make this check has been constructed, although there are no definite plans to complete the study at the present time.

C. CONSTRUCTION OF PROPOSED OUTPUT STRUCTURE

Part of the proposed output structure based on the solution of the boundary value problem has been constructed. The entire output structure is illustrated in Figure 19. The output cavity of this structure is as shown in Figure 13. Figure 20 shows the constructed output structure minus the output cavity. The wave-guide window, vacuum-pump connection, collector water connection, the arm of the sliding short circuit, and the coaxial output line can be seen in Figure 20. This structure may be used

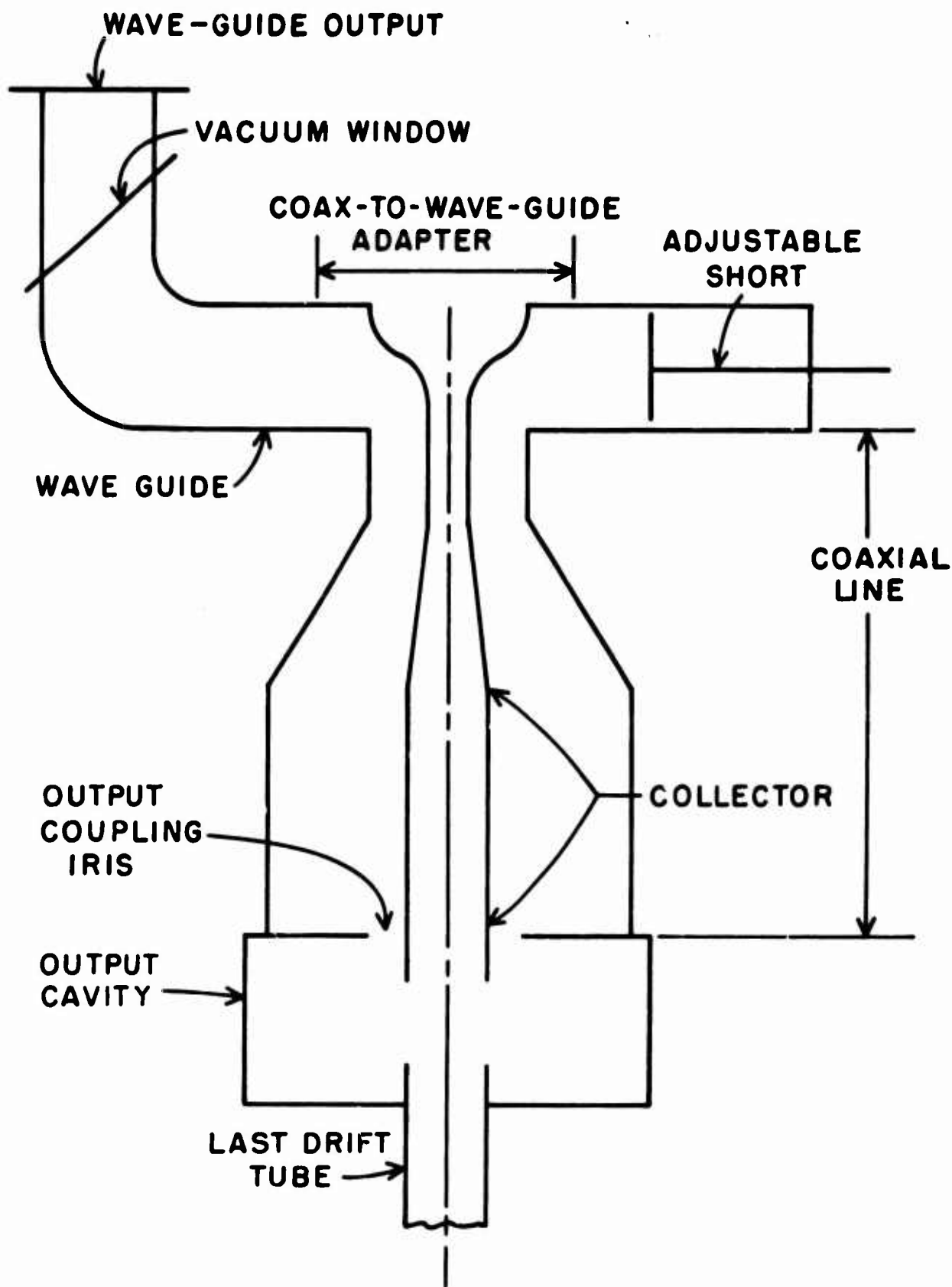


FIGURE 19. New Output Structure for VA-87.

for a variety of cavities, but the output cavity must be added to the structure. The structure as shown in Figure 20 has been vacuum leak tested down to a pressure of 2×10^{-7} Torr.

Construction of the test instrument (electron gun and first three cavities of a VA-87C) described in Section III. B.1 has been completed and vacuum leak tested to a pressure of 2×10^{-8} Torr. The cathode must be activated before the test instrument is put into operating condition. Some limited cathode activation was done. A dummy collector was placed on the ball valve, since the test instrument does not include a collector. During this work, it was determined that the perveance of the rebuilt electron gun had not been changed and that the electron beam passed through the ball valve into the dummy collector without drift tube interception.

-55-

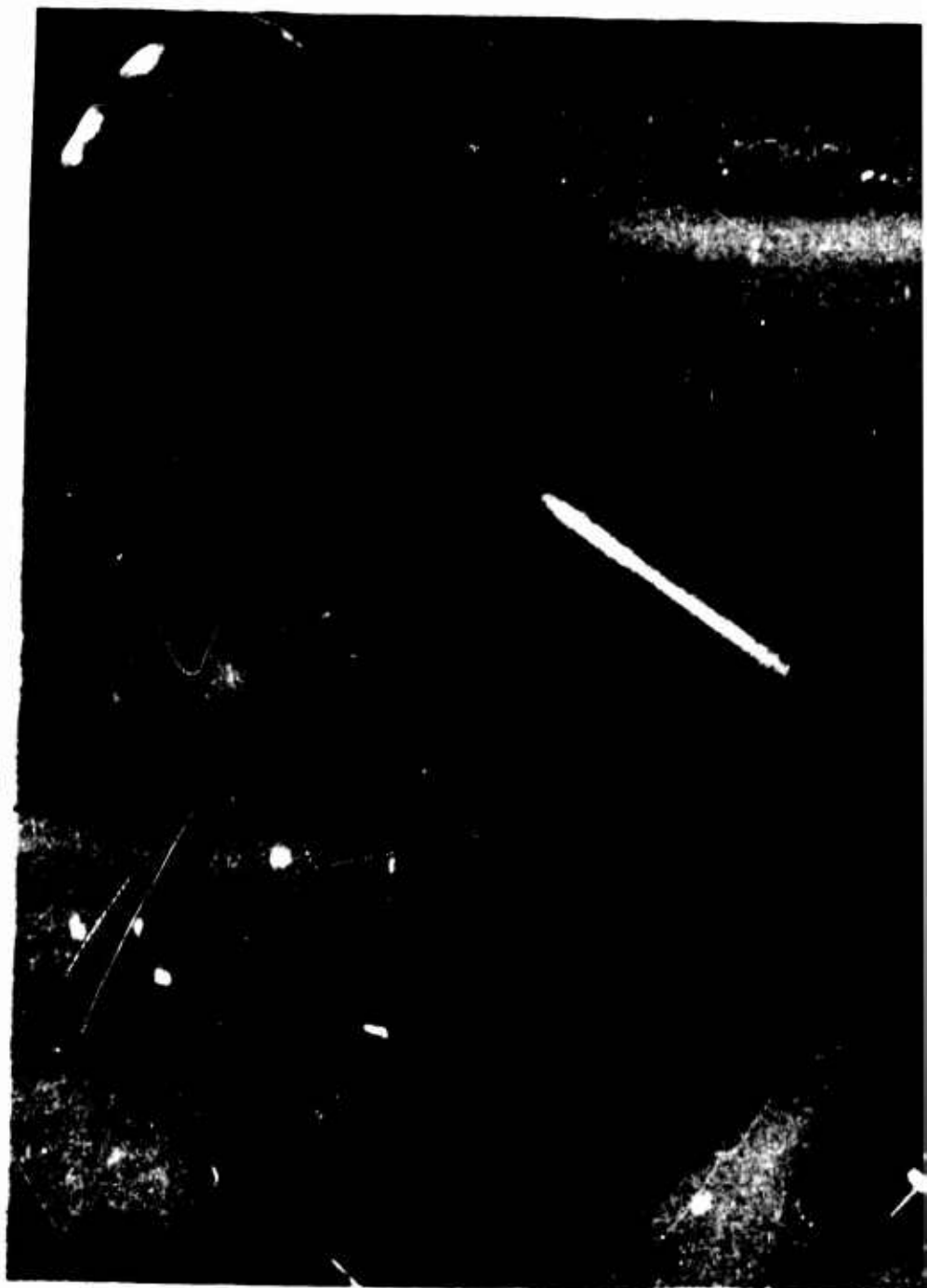
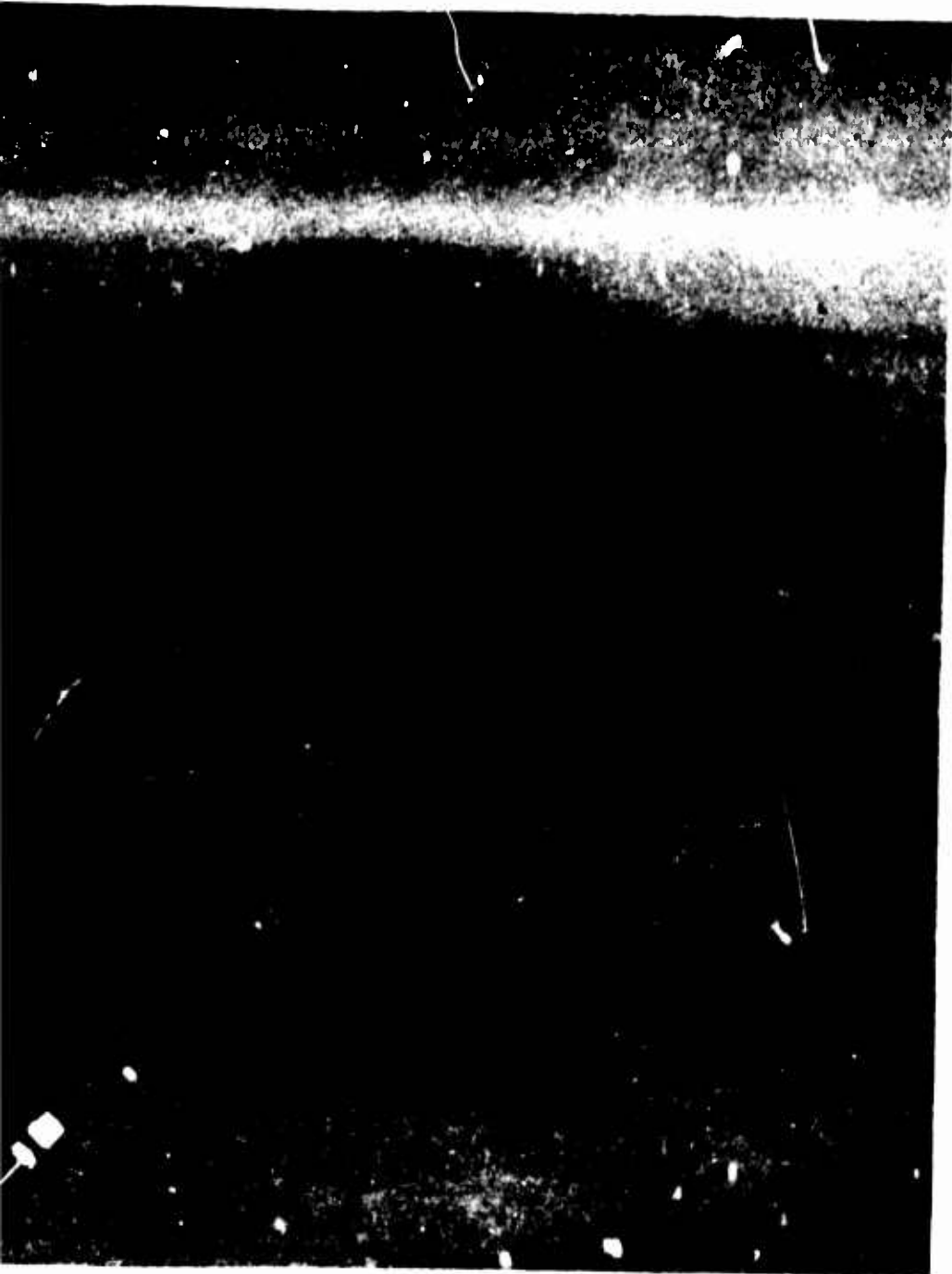


FIGURE 20. New Output Struc



Structure for VA-87 Minus Output Cavity.

V. SUMMARY AND RECOMMENDATIONS

The design of the general, symmetrically loaded, double re-entrant, high-power, coaxial klystron cavity has been specified. The background, the requirement, the reduction to system specifications, and the construction of a high power spurious output test facility is described. Measurements on this system as well as measurements made on other systems, are reported and compared with other available pertinent data. The design techniques used in solving the cavity's boundary value problem are general, and the general formulation of the problem (but not necessarily the specific results) may be used if a special structure is to be considered. All the signal-sampling networks discussed in this study have their application. The best network to use in a given case depends upon the nature of the required information. The most economical transmission line network, in both initial investment and time required per test, is the mode mixer system; however, other systems will provide greater accuracy and modal power information. The comparison of spurious output signal measurement results demonstrates that all these signal-sampling networks provide for general agreement between systems.

Effort on mechanical design, other cavity configurations, and other coax-to-waveguide transitions are recommended as future work areas. All these structures and the proposed structure discussed in this thesis should be built and undergo hot-test.

VI. REFERENCES

1. L. A. MacKenzie, "Klystron Cavities for Minimum Spurious Output Power," Research Report EE 418, Cornell Univ., January 1959.
2. R. D. Campbell, "Radar Interference to Microwave Communications Services," Electrical Engineering (October 1958).
3. Delmar C. Ports, et al., "Interference Prediction Study," Jansky and Bailey, Contract AF 30(602)-1934, Wash., D. C., January 1960.
4. W. E. Blair, "Harmonic Analysis of Electron Beams in Klystrons," Research Report EE 458, Cornell Univ., January 1960.
5. V. Price, J. P. Rooney, and C. Milazzo, "Measurement and Control of Harmonic and Spurious Microwave Energy," Gen. Elec. Microwave Lab., Report No. TIS R58ELM 112-1, Contract No. AF 30(602)-1670, Palo Alto, Calif., July 8, 1958.
6. V. G. Price and G. Novick, "Measurement and Control of Harmonic and Spurious Microwave Energy," Gen. Elec. Microwave Lab., Report No. TIS R59ELM 112-3, Contract AF 30(602)-1670, Palo Alto, Calif., May 15, 1959.
7. C. C. Wang, "Electromagnetic Field Inside a Cylinder with a Gap," Jour. Appl. Phys., 16 (June 1945), p. 351.

PART II

**A STUDY OF SPACE-CHARGE WAVE PROPAGATION
ALONG A PERIODICALLY VARYING ELECTRON BEAM**

M. Roberts

I. INTRODUCTION

Periodic structures are of considerable importance in much of engineering and physics. The fact that the periodicity of most manufactured and naturally occurring structures, such as wave guides or crystals, is fixed makes studies of periodicity-dependent effects impractical. The electron beam, however, is an excellent study vehicle because its periodicity is directly controlled by its constraining magnetic field.

In the years 1952 to 1954, much theoretical work and some experimental work was done concerning the effects of periodic interactions with space-charge waves in beam tubes. Rydbeck and Agdur¹ presented a general treatment of periodic interactions of space-charge waves which showed that the behavior of the waves is described by solutions of Mathieu's Equation. About the same time, Birdsall^{1a} reported that a simple theory could be used to predict gain with either a velocity jump, a rippled-wall or a rippled-stream type of periodic interaction, and that some experimental evidence of rippled-wall amplification was observed. Bloom² analyzed the problem of space-charge waves on a scalloping beam in detail, including the effect of confined beam-reduction factors. Shortly afterward, Rich³ presented a rigorous mathematical treatment of the same problem to explain the gain experimentally observed on a scalloping beam by Mihran.⁴ In recent studies of a Brillouin beam, Gilmour⁵ reported experimental evidence of a "locking" phenomenon between

the plasma half-wavelength and the scallop wavelength at magnetic fields below the Brillouin value. This experiment is designed to verify quantitatively the applicability of the Mathieu-Equation model, and with the highly controlled environment available, determine the effects of any imperfections on the beam, if possible. Although the detailed calculations and experimentation here apply solely to Brillouin beams, the same analysis is valid for any beam in which there is a periodic density variation caused by improper focusing conditions.

In any practical situation where Brillouin focus conditions are being used, some scalloping of the beam is likely to occur. Thus, either gain or some other effect of the scalloped-beam amplification mechanism is a real possibility in beam tubes.

To verify the model, a complete study of the effect of the plane of excitation was made using a sliding input cavity. The ratio of plasma-to-scallop wavelengths was continuously varied giving rise to a transition between stable and unstable solutions of the Mathieu Equation. The question of saturation levels and effects was briefly explored.

As the interaction phenomenon can take on the properties of either amplification or attenuation, it is possible to exploit this inherent beam property for either signal enhancement or, under certain conditions, for reduction of a properly launched noise wave. It is also conceivable that this ever-present interaction is the cause of second-order effects in beam tubes where even a slight radial motion of the beam is possible.

II. STATEMENT OF THE PROBLEM

The problem under consideration is to determine what effect the scalloping of an electron beam has on the propagation of space-charge waves along the electron beam. In this particular case of a Brillouin beam, the electron beam emerges from a shielded cathode gun into a drift region and is constrained by an axial magnetic field. Generally, the balance of forces - space charge, magnetic, and centripetal - will not be exact and an oscillatory radial motion, i. e. scalloping, of the beam will result. As can be shown,⁶ for a moderate force imbalance, the radius of the beam can be described as a sinusoidal function yielding a wave number. This scallop wave number is proportional to the axial magnetic-field strength. This condition of force imbalance violates one of the standard conditions of Brillouin flow; however, for lack of a better name we consider this beam to be a scalloping Brillouin beam.

If a modulating cavity is placed along the beam and r-f bunches formed by the action of the r-f fields, how is the propagation of these space-charge waves affected by the various parameters describing the electron beam-space charge-wave situation? In particular, what is the effect or importance of the ratio of effective-plasma wave numbers to scallop wave numbers, and of the depth of scalloping, modulation frequency, cavity position, magnetic field, power level, beam voltage, or perveance? This study is designed to answer these questions.

III. PHYSICAL EXPLANATION

A simple physical explanation for the interaction phenomenon can be given for the case of optimum-gain conditions; other conditions between optimum gain and pure attenuation can be understood by extension of this explanation.

The most important feature contrasting a scalloping beam with the ideal Brillouin beam is the periodic change in electron density. This density variation will be shown to cause the interesting gain phenomena observed. It is convenient to use the standing-wave concept of space-charge waves with the current and velocity waves in space quadrature. Associating the current wave with potential energy, and the velocity wave with kinetic energy will aid in understanding the processes involved.

On an ideal Brillouin beam, energy is given to the beam by the velocity-modulating cavity in the form of an ordering of the electrons against a space-charge force. This kinetic energy is transformed into the potential energy of a current bunch after a quarter plasma cycle, and the transfer of energy between kinetic and potential forms persists until the signal energy is abstracted from the beam. As the density in this ideal beam is constant with distance, an exact interchange of energy results each quarter cycle; i.e. the beam acts as a passive, lossless medium of transmission only.

The case of the scalloped beam with the periodically varying electron density is fundamentally different in that this beam is a possible energy source, an active device. The source of energy is the radial motion of the electrons which are travelling along what has been described⁷ as a

potential trough. (This description is based upon the use of a generalized potential involving all the energy of radial motion.) The electron in a scalloped beam continually rolls up and down both sides of this trough as it moves along the force-free drift region; the outer side corresponds to the higher energy of rotation at radii greater than the equilibrium value, and the inner barrier corresponds to the greater energy needed to overcome the repulsive space-charge forces. It is this energy of radial oscillation which is tapped by the interaction process and converted to axial energy in the form of an ordering of the electrons into growing r-f waves. It follows directly that as the forward "r-f energy" is enhanced, the radial excess "d-c energy" will decrease, and hence the amplitude of the scallops must be reduced by some small amount.

In the optimum case for scalloped beam amplification, the scallop wavelength and the half-plasma wavelength are nearly identical. The velocity-modulating cavity is at the plane where the radius is increasing and at the equilibrium value. In the quarter plasma wavelength that is required for the current bunch to form, the density of the beam is always lower than average. This average density represents an equivalent unscalloped beam that would exist were the magnetic field adjusted to the proper value. Thus, for a given modulating field strength, higher-level bunches can be obtained as the resisting space-charge force is lower. Corresponding to the higher level bunch, the bunching distance increases beyond the usual quarter plasma wavelength. As the bunch is drifting and beginning to dissipate, the density is always higher than average, making the bunch more dense throughout this entire half-cycle. This compression of the bunch is, in effect, an addition of potential energy to

the space-charge wave with the accompanying loss of transverse energy to the beam. The higher-energy bunch is transferring this additional energy to the kinetic form, and the velocity standing wave consequently reaches a higher amplitude than it would on the corresponding non-scalloping beam. This two-stage process of weak space-charge forces during bunching and strong compressive forces during debunching provides an energy-pumping mechanism analogous to a parametric amplifier and results in exponential growth.

As might be expected, more efficient energy transfer would result if compression of the bunch were applied at a constant level over a full half-cycle rather than with the sinusoidal variation applied by a scalloped beam. This condition is met in the two region, stepped-beam discussed by Mihran.⁴ He showed that for the same ratio of densities in the two regions the stepped beam is $4/\pi$ times as effective as the scalloped beam. This factor corresponds to the fundamental component in the stepped beam and shows the null role played by higher-periodicity density variations.

It is also interesting to note that this explanation can be applied to any type beam, whether Brillouin or confined, pointing up the apparent insensitivity of this mechanism to a particular type of electron dynamics.

IV. THEORY

A. MODEL

The development of the theory proceeds as follows: The beam is thought to be characterized by its envelope (all assumptions are clearly stated in the next section), and the envelope in turn is typified by one electron. The dynamical motion of this edge electron is examined using the force equation, the continuity equation, the definition of current density, and knowledge of the boundary values. The conditions used in this analysis are those for a one-dimensional problem, even though the essence of this phenomenon is in the radial motion of the beam. The results of this analysis, which look like transmission-line equations, are generalized to include a sinusoidal density variation and also to account for the consequences of a beam of finite extent in a finite magnetic field. In this process, one is led to a Mathieu-Equation relationship for the a-c current or a-c potential along this "transmission line" formed by the beam. The r-f current and velocity are connected to the transmission-line variable by a traveling-wave exponential factor and the Chu⁸ equivalent kinetic potential.

This model is admirable for its simplicity and ability to predict essentially all the observable phenomena with only small quantitative errors. The major drawback lies in the fact that it is a linear theory capable of treating only first-order effects. The second-order effects of power saturation and the means of energy exchange are not included in this model. A more extensive study allowing for a slow change in the density variation would probably show the energy-exchange mechanism with some clarity.

B. ASSUMPTIONS

The assumptions made in the course of the argument in the next section are discussed here in the order of appearance. A discussion of the validity of these assumptions in this particular experimental situation is contained in section VB.

1. **Laminar Flow.** This statement of axial symmetry and non-interacting layer-like behavior of the beam allows us to generalize from the behavior of one electron to the behavior of the entire beam. By eliminating crossovers and other multivalued conditions, much simplicity is gained in the analysis.

2. **Single Axial Velocity.** This requirement refers to the average drift velocity of the beam and implies a negligible velocity spread. This simplification permits the use of straightforward differential equations.

3. **Sinusoidal Perturbation.** This form of time variation, (imaginary part of) $\exp(j\omega t)$, is not actually restrictive, although practical in allowing the time-derivative operator to be handled as a simple multiplicative factor. More complicated time variations can be treated by using Fourier methods which then reduce the problem to summing solutions of this sinusoidal form.

4. **Small Signal Level.** This requirement does not allow any saturation effects to enter, but does allow linearization of the various equations. The separation of d-c and a-c parts leads to simple closed-form results.

5. **Strong Magnetic Field.** This assumption, prohibiting any transverse motion, appears to be out of place in this discussion of radial

interactions. It is, however, a major simplifying step and is relaxed by Assumption 10 at a later step.

6. The Beam is Open Circuited to a-c Current. This boundary condition means the total a-c current is zero initially. It also implies that the modulating cavity applies only longitudinal accelerating fields and no transverse fields. This requirement is also part of the one-dimensional approach to the analysis.

7. Small Scalping. This condition on the allowable variation of the cross-sectional area is used to generalize the one-dimensional analysis. This relaxation of Assumption 5 allows finite magnetic fields, and is analogous to the requirement of a sinusoidal time variation. The use of sinusoidal space functions puts the equations in the form of Mathieu's Equation, permitting use of the substantial body of work done on this subject. For moderate values of scalping, even up to three-to-one ratios of diameters, the trajectory, in theory, departs very slowly from a simple sine wave.⁶ Higher order density variations do not enter into the interaction because their effect over a full period of the fundamental variation is zero.

8. Lossless System. This restriction does not affect the results in any substantial fashion. It does, certainly, obscure the energy-exchange mechanism and is probably the first assumption to be relaxed in an expansion of this theory. Making the assumption reduces the equations to elementary forms.

9. Traveling Waves. This statement of spatial dependence of the form $\exp(-j\beta z)$ is certainly not exact for the Brillouin case, in which the r-f current travels as ripples along the surface. A more exact treatment would need a spatial dependence of the form $\exp(-j\vec{\beta} \cdot \vec{r})$. Introduction of

the simpler factor permits the analysis to proceed using the envelope function of the current and not the entire solution.

10. $\omega_q = p\omega_p$. The effective plasma frequency is given by the plasma-frequency reduction factor times the plasma frequency calculated on the basis of an infinite beam. This relation introduces the plasma-reduction factor and brings into the theory the effect of a beam of finite extent in a finite metal tunnel. This situation of a beam in a tunnel is characterized by fringing electric-field lines which reduce the longitudinal field strength. As the axial field is less strong, the beam is more compliant, the plasma frequency correspondingly lower, and the plasma wavelength longer. Assumptions 7 and 10 serve to make this analysis a generalized one-dimensional approach capable of describing the interaction under investigation.

11. A Drifting Beam. This condition provides that the average forward velocity be constant throughout the drift region and unaffected by the interchange of energy expected in this amplification process. By requiring constant velocity, it is possible to associate the forward a-c velocity with an equivalent a-c potential leading to the transmission-line equations.

The three remaining assumptions must be made to obtain numerical results in a particular beam dynamics problem:

12. Brillouin-Flow Beam. By this less than standard use of the term Brillouin flow is meant: a) no flux threads the cathode, and b) the force balance is attainable by proper adjustment of the magnetic field. The extension of the terminology is required when the magnetic field is deliberately varied from the Brillouin value to cause scalloping. The

essence of the assumption is that the published reduction factors for a strictly Brillouin beam are applicable to this generalized Brillouin beam. This requirement also eliminates positive ions from the beam.

13. A Large Ratio of Wall-to-Beam Radii. This condition is necessary to obtain a value of p , the plasma-reduction factor, versus βb , the argument of the field variation. This assumption is certainly not restrictive since this ratio parameter ceases to have any importance above the value of two.

14. Lowest Radial Mode of Propagation. This requirement is also necessary to identify a particular p versus βb curve, and otherwise should not affect the results.

C. FORM OF THE ARGUMENT

This discussion is based upon the work of Bloom and Peter,⁹ and Bloom.²

1. Notation

All the pertinent variables can be written in the form of a d-c and an a-c term; the a-c term is written as

$$v_{ac}(z, t) = v'(z) e^{j\omega t}$$

where the time dependence is separated from the spatial dependence.

2. Analysis

The analysis begins with the a-c force equation for a beam electron

$$eE = F = m \frac{dv}{dt} \quad , \quad (1)$$

where e is the algebraic charge of the electron; m , the mass; E , the axial electric field; F , the force on the electron; t , the time variable; and the subscript ac has been dropped. Equation (1) can be rewritten expanding the derivative and using the charge-to-mass ratio of the electron η and the d-c axial velocity v_0 as

$$\eta E = \frac{dv}{dt} = \frac{\partial v}{\partial t} + v_0 \frac{\partial v}{\partial z} \quad .$$

Performing the time-derivative operation and cancelling the time factor, the force equation takes the final form:

$$\eta E' = j\omega v' + v_0 \frac{\partial v'}{\partial x} \quad , \quad (2)$$

where ω is the excitation radian frequency. Assumptions 1 to 5 involving laminarity, monoenergetic electrons, sinusoidal time variation, linearity and one-dimensional flow have been used in deriving this expression.

The second important expression, using Assumption 6 that the total beam current is zero, is

$$J + \frac{\partial D}{\partial t} = 0 = J' + j\omega \epsilon_0 E' \quad ,$$

where J is the current density; D , the electric flux density; ϵ_0 , the permittivity of free space; and j is the complex number $\sqrt{-1}$. Writing the current density in terms of the a-c convection current I' , and the cross-sectional area σ as $J' = I'/\sigma$, the relation between current and electric field is

$$I' + j\omega\epsilon_0\sigma E' = 0 \quad (3)$$

The third important equation is written as the definition of current density in terms of the d-c space-charge density ρ_0 and the a-c space charge density ρ' :

$$J' = \rho_0 v' + v_0 \rho' \quad , \quad (4)$$

where Assumption 4 has been used to linearize this equation.

The fourth necessary relationship is the continuity equation:

$$\text{DIV } J + \frac{\partial \rho}{\partial t} = 0 \quad ,$$

which reduces to

$$\frac{\partial}{\partial z} \left(\frac{I'}{\sigma} \right) + j\omega\rho' = 0 \quad ,$$

where the divergence operator becomes the axial differential operator by virtue of Assumption 5 concerning transverse motions. This equation can be simplified by saying that the fractional change in cross-sectional area is much less than the fractional change in convection current. This assumption, number 7, is expressed as

$$\frac{\frac{\partial \sigma}{\partial z}}{\sigma} \ll \frac{\frac{\partial I'}{\partial z}}{I'} \quad ,$$

and except for the current nodes, is certainly valid since the area varies as $A + B \cos \phi(z)$ and the current varies directly as a sinusoidal function. The continuity equation can now be written as

$$\frac{1}{\sigma} \frac{\partial I'}{\partial z} + j\omega \rho' = 0 \quad (5)$$

Since the time dependence has been removed, the partial derivatives can now be written as total derivatives.

Equations (2), (3), (4), and (5) relate the four variables E' , v' , I' , and ρ' . E' can be eliminated from Equation (2) and (3) to yield:

$$E' = \frac{-I'}{j\omega \epsilon_0 \sigma} = \frac{j\omega v'}{\eta} + \frac{v_o}{\eta} \frac{dv'}{dz},$$

which can be rewritten as

$$\left(\frac{j}{\omega \epsilon_0 \sigma} \right) I' = \frac{j\omega v'}{\eta} + \frac{v_o}{\eta} \frac{dv'}{dz} \quad (6)$$

The ρ' term can be eliminated from Equations (4) and (5) to yield:

$$\rho' = \frac{J' - \rho_o v'}{v_o} = \frac{j}{\omega \sigma} \frac{dI'}{dz}$$

which can be rewritten as

$$\frac{dI'}{dz} + \frac{j\omega I'}{v_o} = \frac{j\omega \rho_o v'}{v_o} \quad (7)$$

There are now two equations, (6) and (7), for the quantities I' and v' . These two equations can now be put into forms analogous to those describing a transmission line. The traveling-wave space factor of Assumption 9 is introduced as

$$v' = v(z) e^{-j \frac{\omega}{v_o} z} = v(z) e^{-j\beta z} \quad (8)$$

where

$$\beta = \frac{\omega}{v_0}$$

It is convenient to write an expression relating the total potential and the total velocity of the beam as

$$2\eta(V_0 + V) = (v_0 + v)^2 = v_0^2 + 2v_0 v,$$

where only linear terms are kept. V_0 and V are the d-c and a-c potentials. A relation for the equivalent a-c potential on the beam in terms of the velocities describing the beam is now

$$V = -\frac{v_0 v}{\eta}$$

If now Equation (8) is differentiated and multiplied by v_0/η ,

$$\frac{v_0}{\eta} \frac{dv}{dz} = \frac{v_0}{\eta} e^{j\beta z} \frac{dv'}{dz} + j\beta v_0 \frac{v'}{\eta} e^{j\beta z}$$

Multiplying Equation (6) by $e^{j\beta z}$, and noticing that

$$\frac{v_0}{\eta} \frac{dv}{dz} = \frac{jI'}{\omega \epsilon_0 \sigma} e^{j\beta z} = \frac{jI}{\omega \epsilon_0 \sigma}$$

yields the compact equation:

$$\frac{dV}{dz} = \frac{jI}{\omega \epsilon_0 \sigma} \quad (9)$$

Similarly, differentiating the relation between I and I' ,

$$\frac{dI}{dz} = j\beta e^{j\beta z} I' + \frac{dI'}{dz} e^{j\beta z},$$

and multiplying Equation (7) by $e^{j\beta z}$, it is seen that

$$\frac{dI}{dz} = \frac{j\omega \rho_o v}{v_o} e^{j\beta z} = \frac{j\omega \rho_o v}{v_o}$$

But some of the factors can be rearranged as

$$\frac{\sigma \rho_o}{v_o} = \frac{J_o \sigma}{v_o^2} = \frac{I_o}{v_o^2} = \frac{I_o}{2\eta V_o}$$

where I_o is the total d-c current. Using

$$v = \frac{\eta V}{v_o},$$

the second compact equation,

$$\frac{dI}{dz} = \left(\frac{j\omega I_o}{2v_o V_o} \right) v, \quad (10)$$

can be obtained.

At this point the one-dimensional analysis can be generalized to include the effects of both finite beams and finite magnetic confining fields. The finite beam is introduced by means of the plasma reduction factor, Assumption 10, which can be thought of as generalizing the permittivity. This procedure is first:

$$\omega_p = \left(\frac{\eta \rho_o}{\epsilon_o} \right)^{\frac{1}{2}} \left(\frac{\eta I_o}{\epsilon_o v_o \sigma} \right)^{\frac{1}{2}}$$

and then:

$$\omega_q = p\omega_p = \left(\frac{\eta I_o}{\epsilon v_o \sigma} \right)^{\frac{1}{2}} = \left(\frac{p^2 \eta I_o}{\epsilon_o v_o \sigma} \right)^{\frac{1}{2}},$$

where $p = p(\beta L, r_{\text{wall}}/r_{\text{beam}}, \text{radial mode of propagation})$. The finite magnetic field can be introduced simply by permitting the hitherto constant cross-sectional area to be a sinusoidally varying quantity in all subsequent equations. It is here that Assumption 8 is relevant, since σ is not allowed to have any slow decrease or increase corresponding to gain or attenuation of the space-charge waves. Equations (9) and (10) are the envelope functions of traveling waves having oscillatory factors of $e^{j\omega t - j\beta z}$. These envelope equations look like the transmission-line equation

$$\frac{dV}{dz} = jXI, \quad \frac{dI}{dz} = jBV; \quad (11)$$

if the reactance X and the susceptance B are written as

$$X = \frac{p^2}{\omega \epsilon_o \sigma} = - \frac{p^2}{\omega_o \pi b^2},$$

$$B = \frac{\omega I_o}{2v_o V_o} = \frac{\omega I_o \eta}{v_o^3} \quad (12)$$

Since the drifting beam has constant average axial velocity by Assumption 11, B is a constant. The reactance, however, is a complicated function of distance because both σ and p vary along the axis.

Thus,

$$B = B_0, \quad X = X_0 \left(1 + k \cos 2\pi \frac{z}{\lambda_s}\right), \quad (13)$$

where again the small scalloping assumption is used and the reactance modulation index k , which is different than the scallop percentage index Δ , is introduced.

Combining Equations (11) yields

$$\frac{dI}{dz} = jBV, \quad \frac{d^2 I}{dz^2} = jB \frac{dV}{dz} - BXI; \quad (14)$$

substituting Equations (13) into Equation (14), it is found that

$$\frac{d^2 I}{dz^2} + B_0 X_0 \left(1 + k \cos 2\pi \frac{z}{\lambda_s}\right) I = 0,$$

but

$$B_0 X_0 = \frac{\omega I_0 \eta}{v_0^3} \frac{p^2}{\omega \epsilon_0 \pi b^2} = \frac{I_0 p^2 \eta}{v_0^3 \epsilon_0 \pi b^2} = \frac{p^2 \rho_0 \eta}{v_0^2 \epsilon_0} \cdot \frac{p^2 \omega p}{v_0^2} = \frac{\omega q}{v_0^2} = \left(\frac{2\pi}{\lambda_q}\right)^2. \quad (15)$$

Using Equations (15) and the definitions

$$A \equiv \left(\frac{2\lambda_s}{\lambda_q}\right)^2, \quad q \equiv \frac{kA}{2}, \quad x \equiv \frac{\pi z}{\lambda_s},$$

(where λ_s and λ_q are the scallop and reduced-plasma wavelengths)

the resultant equation for the a-c current is

$$\frac{d^2 I}{dx^2} + (A + 2q \cos 2x)I = 0. \quad (16)$$

Equation (16) is a form of Mathieu's Equation, the behavior of which has been thoroughly studied.¹⁰

The solutions to the Mathieu Equation take the forms $e^{\pm\mu x}\phi(x, A, q)$, where μ is a constant determined by the values of A and q , and $\phi(x, A, q)$ is a periodic function of sines and cosines. If μ is imaginary, the solutions are oscillatory and stable; if μ is real, the solutions are unstable and either grow or decay. The dependence of the growth factor μ upon A and q is shown in the Mathieu diagram, Figure 1, which is a small portion of the complete map of the Mathieu solutions.

The physical boundary condition that k_{\max} be unity limits possible solutions to the left of the line $A = 2q$. It is shown later that for a Brillouin beam, A is always less than two, further restricting the possible values of the solution.

The regions of instability occurring on the Mathieu diagram are centered about the values $A = n^2$, where n is a non-zero integer. These unstable regions for n greater than unity are progressively narrower with respect to the variation in A ; the growth factor also gets smaller as n gets larger. Although it might be possible to use the higher regions under other conditions, it is only the first and broadest instability region that is of interest in this study.

The stable regions give rise to space-charge wave solutions whose envelopes are periodic; the solutions are perturbed from the unscalloped-type waves by a phase factor, $\exp(j|\mu|x)$. These waves are not considered in the following discussion which concerns only μ real.

It can be noticed that the value of A for maximum growth rates is exactly unity for vanishingly small values of q , but is slightly greater

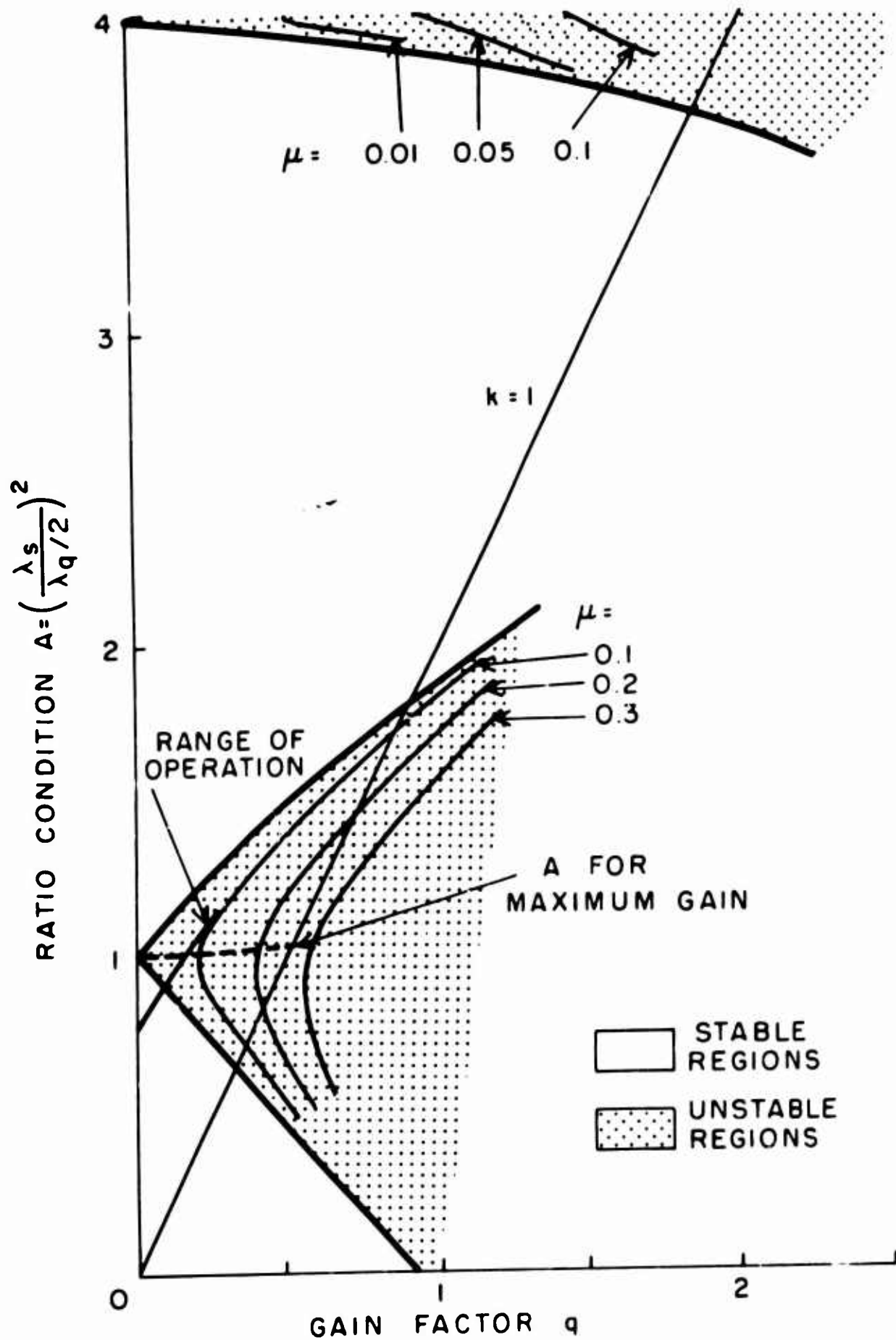


FIGURE 1. The A, q Stability Chart of Mathieu Equation: $d^2I/dx^2 + (A + 2q \cos 2x)I = 0$.

than unity for finite values of q . There is no clear physical reason for this slight deviation, which appears in the mathematical expressions for the diagram in Figure 1.

As the general solution to the Mathieu Equation is rather involved, it is convenient to investigate the solution in the major region of interest, i.e. where A is approximately unity. The solutions in any part of the unstable region are of the same form, but the multiplying constants are simplest for $A = 1$. Considering $A = 1$, the approximate solution¹⁰ can be written as a combination of the two linearly independent solutions:

$$I(x, q) = a_1 e^{-\mu x} \left[ce_1(x, q) - \left(\frac{8-3q}{8+3q} \right)^{\frac{1}{2}} se_1(x, q) \right] \\ + a_2 e^{+\mu x} \left[ce_1(x, q) + \left(\frac{8-3q}{8+3q} \right)^{\frac{1}{2}} se_1(x, q) \right],$$

where a_1 and a_2 are arbitrary constants to be fixed with initial conditions; and ce_1 and se_1 are the first cosine and sine Mathieu functions, which take the following form (se_1 , in terms of sines, is similar):

$$ce_1 = \cos x - \frac{q}{8} \cos 3x - \frac{q^2}{64} \left(\cos 3x - \frac{1}{3} \cos 5x \right) + \dots$$

Since Equation (16) could have been written in terms of the a -c potential V , and V and I are related by Equations (11), it is seen that V and I have the same form. By replacing the arbitrary constants with the initial conditions we can write the matrix of the transmission line as

$$\begin{bmatrix} I(x, q) \\ V(x, q) \end{bmatrix} = \begin{bmatrix} \bar{A}(x_0, x, \mu) & \bar{B}(x_0, x, \mu) \\ \bar{C}(x_0, x, \mu) & \bar{D}(x_0, x, \mu) \end{bmatrix} \begin{bmatrix} I^\circ \\ V^\circ \end{bmatrix}$$

where x_0 is the point of excitation; I° and V° , the initial excitations; and \bar{A} , \bar{B} , \bar{C} , \bar{D} are combinations of Mathieu functions and growth factors. For the specific case involved in this experiment, the excitation was pure velocity modulation or

$$I^\circ(x_0) = 0, \quad I(x, q) = \bar{B} V^\circ,$$

where the coefficient is expressed:

$$\bar{B} = G(x_0, x) e^{+\mu x} - H(x_0, x) e^{-\mu x} \quad (17)$$

Finally the normalized current after $n + 1/2$ scallops can be written as

$$\frac{I\left(x_0 + \left(n + \frac{1}{2}\right) \pi, q\right)}{\frac{\beta_s}{X} V^\circ} = \frac{e^{-\left(n + \frac{1}{2}\right) \pi \mu}}{1 + \frac{1}{f}} + \frac{e^{+\left(n + \frac{1}{2}\right) \pi \mu}}{1 + f} \quad (18)$$

where $f(x_0, q)$ is the function describing the effects of the cavity position relative to the scalloping beam. The function f and its correlation with the radius of the beam are shown in Figure 2. It should be noticed that only for $q = 0$ and $x_0 = \text{either } \pi/4 \text{ or } 3\pi/4$ is the solution strictly growing or decaying; $f(q, x_0)$ is actually $f(q^2, x_0)$ and becomes very small or very large, but finite. These statements say that in general the solution is a mixture of the growing and decaying solutions with the

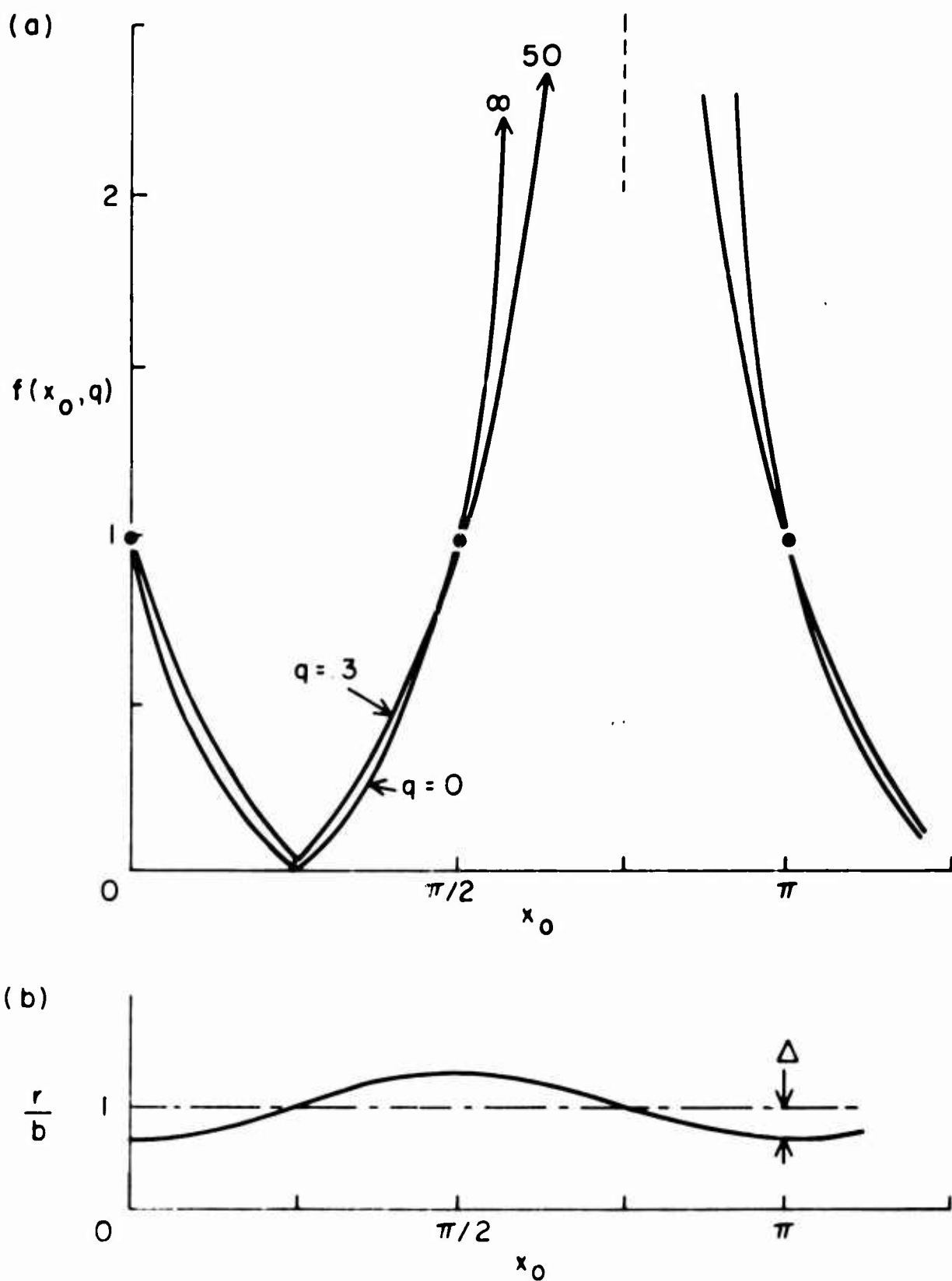


FIGURE 2. (a) Weighting Function $f(x_0, q)$ Versus Cavity Position x_0 , Showing Variation with Gain Factor q . (b) Normalized Radius r/b Corresponding to Cavity Position x_0 . (Taken From Bloom.²)

growing solution dominant after some large number of scallops.

The last analytical step is to relate the reactance modulation index k and the gain factor q to the physical quantity Δ , the percentage scalloping. The relation between k and Δ is not direct because of the form of the reduction factor. The nonlinear behavior of the reduction-factor curve causes a given amount of scalloping to be less effective for low βb beams than for high βb beams.

Recalling the expression for the reactance of the beam

$$X = X_0 \left(1 + k \cos 2\pi \frac{z}{\lambda_s} \right) ,$$

an analogous statement for the radius of the beam can be written using the same sinusoidal approximation,

$$r = b \left(1 - \Delta \cos 2\pi \frac{z}{\lambda_s} \right) ,$$

where b is the equilibrium radius and Δ the scallop-modulation index of the beam. The reactance can be presented in a more advantageous form than Equation (12) as

$$X = \frac{P^2}{\omega \epsilon_0 \pi r^2} = \frac{\beta^2}{\omega \epsilon_0 \pi} \left(\frac{P}{\beta r} \right)^2 .$$

Using the restriction for a Brillouin-beam reduction factor as stated in Assumptions 12, 13, and 14 yields the relation as given by Beck¹¹ and taken from Rigrod and Lewis¹²:

$$p = \left\{ \beta b I_1(\beta b) \left[K_0(\beta b) - \frac{I_0(\beta b) K_0(\beta r_w)}{I_0(\beta r_w)} \right] \right\}^{\frac{1}{2}}$$

This equation and the reciprocal factor (originally defined by Rigrod and Lewis) are plotted in Figure 3. In order to proceed, the normalized-plasma reduction-factor curve (also plotted in Figure 3) must be approximated by the linear relation

$$\frac{p}{\beta r} = a - m \beta r \quad ,$$

where the small-scallop assumption has been invoked, and m is the slope of the normalized p curve. But this can be expanded in terms of the scallop percentage Δ as

$$\begin{aligned} \frac{p}{\beta r} &= a - m \beta b (1 - \Delta \cos 2x) = a - m \beta b + m \beta b \Delta \cos 2x \\ &= \left(\frac{p}{\beta r} \right)_0 \left(1 + m \frac{\beta b \Delta \cos 2x}{\left(\frac{p}{\beta r} \right)_0} \right) \quad , \end{aligned}$$

where the subscript o indicates the quiescent value of the normalized reduction factor. The reactance can now be written in two ways:

$$\begin{aligned} X &= \frac{\beta^2}{\omega \epsilon_0 \pi} \left(\frac{p}{\beta r} \right)_0^2 \left(1 + \frac{m \Delta \beta b}{\left(\frac{p}{\beta r} \right)_0} \cos 2x \right)^2 \\ &= X_0 (1 + k \cos 2x) \quad . \end{aligned}$$

The correspondence between the first-order terms is made giving this important relation:

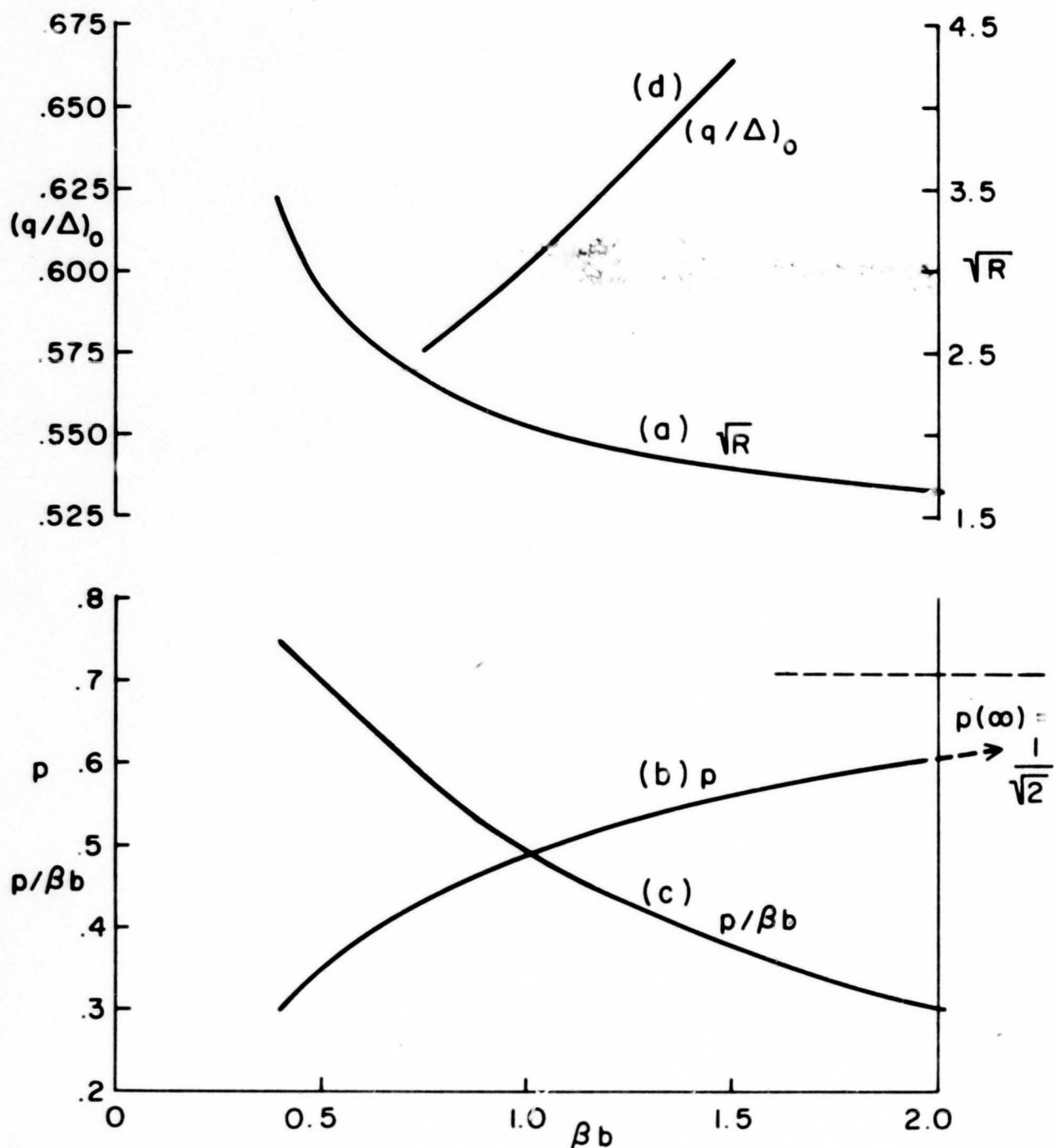


FIGURE 3. Curves Used in the Calculation of the Growth Factor μ :

(a) Dimensionless parameter $R^{\frac{1}{2}}$ defined by $R^{\frac{1}{2}} = \frac{\lambda q}{\lambda_p}$ from Rigrod and Lewis,¹² (b) Plasma reduction factor p given by $p = \frac{1}{R^{\frac{1}{2}}} = \frac{\omega q}{\omega_p}$, (c) Normalized plasma reduction factor $\frac{p}{\beta b}$, (d) Synchronous value of the ratio of gain factor to percentage scallop $\left(\frac{q}{\Delta}\right)_0$.

$$k = 2\Delta m \frac{\beta b}{\left(\frac{p}{\beta r}\right)_0} \quad \text{or} \quad q = \frac{kA}{2} = \Delta A m \frac{\beta b}{\left(\frac{p}{\beta r}\right)_0}$$

We can then write the expression for the quantity q/Δ as

$$\frac{q}{\Delta} = A m \frac{\beta b}{\left(\frac{p}{\beta r}\right)_0}$$

whose synchronous value $(q/\Delta)_0 = (q/\Delta)/A$ is plotted in Figure 3 also.

In summary, it has been shown that once the entrance conditions are known, and the equilibrium radius and percentage scallop calculated or measured, one can compute q since the ratio $(q/\Delta)_0$ is calculated once for all cases. Also, A can now be calculated from the known reduction factor and beam parameters - plasma frequency and magnetic field. Therefore, μ can be computed from the relation

$$\mu = \frac{\pm \{ [(1-A) + q] [(A-1) + q] \}^{\frac{1}{2}}}{2}$$

given by McLachlan¹⁰ from the theory of Mathieu-Equation solutions. Once μ is computed from the given parameters in the situation and the excitation plane known, the problem is solved. A fuller discussion of the theoretical predictions of this analysis follows in the next section.

D. PREDICTIONS

Nearly all the phenomena of importance are contained within the framework of the Mathieu Equation and the behavior of its solutions. In

this small-signal linear theory, there is no treatment of second-order or nonlinear effects. Thus, the energy-exchange mechanism (a second-order effect) and the power-saturation characteristic (a nonlinear phenomenon) cannot be analytically covered here.

1. Growing Solutions

Many physically realizable paths of operation on the Mathieu diagram will give rise to a region of stable solutions and a region of unstable solutions. The maximum growth rate possible is $\mu = .25$ corresponding to 6.8 db gain per scallop. This figure is suspect, however, as the small-signal as well as the small-scallop assumptions would quickly be violated.

2. Effect of Initial Conditions

As there is always a nonzero component of the growing solution, this solution must dominate after some large number of scallops. In practice, the number of scallops is usually on the order of ten; thus, this paper is only concerned with situations involving a small number of scallops.

For a very small degree of scalloping in the unstable region, low gain rates will prevail with the plane of excitation placed anywhere in the low-density half-cycle. Conversely, low decay rates will prevail with the cavity placed anywhere in the high-density half-cycle. As the product nq is raised by more scallops or greater scalloping, the region of initial conditions yielding growing solutions increases. In the high-gain limit,

nearly the full cycle with the exception of an attenuation "resonance" at $x_0 = 3\pi/4$ yields growing solutions.

It is seen, then, that under high-gain conditions the cavity position is not critical. Only if the deamplification feature is desired must care be taken in fixing the excitation plane. The quantitative effect of the excitation-plane position on the gain rate is calculated using the function f and the parameters A and q . One particular case is shown with the corresponding experimental results in Section VC.

3. Relative Periods of Plasma and Scallop Waves

Associated with the possibilities of exciting unstable waves on the beam is the matter of the relative periods of the plasma wave and the scallop wave. This subject is related to the interpretation of the parameter A and to the nature of the periodic Mathieu functions themselves where A represents the square of the ratio of the scallop wavelength to the unperturbed effective plasma half-wavelength. As will be shown, however, under certain conditions the unperturbed plasma wavelength is a mathematical fiction used for calculation purposes only and does not exist on the electron beam.

The solutions of the Mathieu Equation become particularly simple when the conditions $A \gg q > 0$ and A non-integer hold. In this limit, the cosinusoidal term can be taken over to the right-hand side and considered a small perturbing term to the homogeneous equation. The solution to the homogeneous equation has the form $\exp jA^{1/2}x$ which is equal to $\exp j\beta_q z$. This is a solution with the periodicity of the plasma

wave such as one would expect. As the forcing term becomes larger, the periodicity of the solution is altered by an increasing phase term until the parameters are such that μ becomes real. For μ real, either $A \gg q^*$ or $A \sim 1$, and the periodicity is that of the forcing function $\cos 2x$, which is equal to $\cos(2\pi z/\lambda_s)$.

The result of this interesting behavior is that excitation placed at the position of optimum gain will lead to a plasma wave having the periodicity of the scallop. This wave can be thought of as the unperturbed space-charge wave with a continually increasing phase shift. Excitation placed at the position of maximum attenuation also gives rise to a periodicity of the scallop wavelength. For any other cavity position, the total solution is aperiodic. This solution can be interpreted as the sum of contributions from the two periodic waves, one growing and the other decaying. Therefore, as the growing solution dominates, the total solution becomes more the variation $\exp + \mu x$, and the minima shift to the position $x_0 = \pi/4$. This locking of the phase to the optimum condition can be shown analytically by writing the general solution, Equation (17), with the actual Mathieu functions. Now, let $x = x_0 + (n+1)\pi + \delta_n$ and calculate the shift in the argument δ_n of the Mathieu functions for a null. That this is reasonable can be seen from the fact that the total solution, Equation (17), is the difference of two terms. The first term is a growing exponential times a periodic function of x , and the other term is a decaying exponential times a similar

* A is no longer much greater than q .

periodic function of x . Thus, the total solution is slightly aperiodic until equilibrium is reached, whereupon the periodicity is that of the scallop, and the minima fall at $x_0 = \pi/4$. Two effects are involved here. The first is a synchronizing of periods occurring whenever the factor μ is real, and the second is a phase locking dependent upon initial conditions.

It is seen from the Mathieu diagram that for small scalloping (small q), the unstable region is narrow about $A = 1$, and the locking phenomenon is not possible far from synchronism. The locking does, however, become possible far from synchronism at moderate scalloping. This tends to give the physical interpretation that the fields associated with a moderate scallop are strong enough to warp the space-charge waves into the periodicity of the scallop. The plasma frequency is related to the density, which is varying constantly, so that the usual definition of a plasma wave seems to lose its straightforward meaning.

4. Nonsinusoidal Shape of the Envelope

As a direct consequence of the density variation, one would expect a non-sinusoidal shape to $\phi(x, A, q)$, the periodic part of the solution. The standing wave of current or velocity whose phase is initially optimum (starting with velocity modulation) would then have the first quarter-wave in a region of low density and the second quarter-wave in a region of high density. This would cause a standing wave cycle asymmetric about the maximum amplitude. It is this change in curvature that necessitates a more general interpretation of the term

"plasma wavelength" to mean only the distance and not the wave form between the nulls.

5. Relation Between Experimental and Mathematical Parameters

Now that the behavior of the solutions has been discussed, it is important to relate the experimental parameters to μ , A , and q . It is clear from previous discussions that the most desirable case would be with moderate scalloping and synchronism between the unperturbed effective plasma wavelength and the scallop wavelength. For a Brillouin beam, the scallop wavelength is proportional to the square root of the beam voltage and inversely proportional to the magnetic field; the effective plasma wavelength is proportional to the square root of the voltage and inversely proportional to the magnetic field and the plasma-reduction factor. Thus, the parameter A is proportional to the square of the plasma-reduction factor only. The plasma-reduction factor, in turn, is a function of the excitation frequency, and the square root of the perveance, and is inversely proportional to the magnetic field.

The other parameter needed in the analysis is q , which is a function of both k and A . And k is a complicated function of the plasma-reduction factor and also proportional to the percentage scalloping. Scalloping can be induced by varying the magnetic field, the accelerating voltage, the perveance, or the beam-focusing conditions, i.e., by varying one condition with the others adjusted for possible Brillouin conditions.

Thus, the only parameters that can be adjusted to give independent motion on the Mathieu diagram are the voltage and the focusing-field conditions. Since the reduction factor is proportional to βb , and β is proportional to $V^{-\frac{1}{2}}$ and b to $V^{\frac{1}{2}}$, there should be no change in the value of A as q is varied. This feature should allow a simple control of the possible gain by changing either the design ~~voltage~~ ~~of~~ gun configuration.

Variation of any other parameter is seen to affect both A and q and generates motion along some diagonal on the plane. For example, decreasing the magnetic field from the Brillouin value serves to increase the equilibrium radius b and hence raises the reduction factor p , which in turn raises both A and q . Thus, lowering B , the magnetic flux density, should move the operating point along an upward diagonal on the Mathieu diagram.

The special properties of the Brillouin beam in this connection are interesting. The plasma-reduction factor for a Brillouin beam approaches 0.707, as opposed to unity for a confined beam, limiting the range of operation of the Brillouin beam on the Mathieu diagram to somewhat less than that for a confined beam. Reference to the values of A versus p^2 shows that the maximum value of A for this type of beam is approximately 2.0, indicating that only the first unstable region can be attained in Brillouin flow.

Motion on a positive diagonal line does not necessarily imply increasing gain rates, as can be shown by a consideration of the instability region. If the path runs parallel to the μ contours there is no enhancement of the gain rate; if the path runs across the μ contours,

however, an increase in the gain rate can be expected. Therefore, the gain rate is always increased by raising the voltage and can be increased by raising the perveance or frequency, or by decreasing the magnetic field.

In summary, a change in the frequency, which affects μ only through the reduction factor, is seen as reasonably critical for $\beta b \lesssim 1$ and essentially unimportant for $\beta b > 1$. As will be shown, the curve of effective plasma half-wavelength intersects the curve of scallop wavelengths (both versus magnetic field) at a small angle. Thus, a change in frequency shifts the point of synchronism, which in turn effects μ . Under a given set of conditions, increasing the frequency will shift the possible gain region to higher magnetic fields. In the limit of very high frequencies (above 10 kMc/s), p becomes equal to 0.707 and $\lambda_q/2 = \lambda_c$. However, $\lambda_s = 1.414\lambda_c$, and there can be no gain as $A = 2$.

The magnetic field also influences μ through the reduction factor as well as through Δ . Like the frequency, its effects on μ would be more noticeable for $\beta b \lesssim 1$ and less noticeable for $\beta b > 1$.

6. Importance of Factors Suppressed by the Theory

The final part of this discussion concerns four factors that were assumed not present, but which do appear in many practical situations. The first is the presence of a slight amount of cathode flux; the second, the possibility of some translaminar electrons; the third, the influence of positive ions on the beam; and the fourth, the possibility of a limitation on the gain mechanism by saturation. It has been shown¹³ using

the laminar theory that flux threading the cathode will shorten the scallop wavelength on the beam. Thus, it is possible that the inclusion in the cathode of a fraction of a percent of the axial flux could bring A closer to unity for a given percentage scalloping. This change in A would cause a higher gain than anticipated with the simple theory presented here. Thus, the unavoidable result of a difficult shielding problem can in some cases be used advantageously for increased amplification.

Similarly, translaminar currents can affect the scallop wavelength and, therefore, the ratio A . Translaminar electrons can be considered as streams of particles violently scalloping and periodically going from beam edge to beam axis and back.¹⁴ These small streams move in the nearly force-free (depending upon the extent of the departure from Brillouin flow) region of the interior of the beam and take on a wavelength shorter than that of the scallop. The translaminar electrons affect the remainder of the beam by "pulling" the scallop wavelength of the majority of electrons slightly toward a shorter wavelength.

On the other hand, the inclusion of positive ions in the beam tends to neutralize the space-charge force and create more scalloping for a given set of conditions. It is, therefore, possible that the presence of ions can enhance the gain in a given situation.

Although it will become clearer with the presentation of the curves $\lambda_s(B)$, $\lambda_q(B)$, and $\Delta(B)$ in Chapter V, it is helpful to summarize the effects of the various parameters at this point. It is the interrelationships between $\lambda_s(B)$, $\lambda_q(B)$, $\Delta(B)$, and $p(\beta b)$ that determine μ . To make this more meaningful, one can say that ω affects only $\lambda_q(B)$,

cathode flux and translaminar electrons affect $\lambda_s(B)$, and positive ions affect only $\Delta(B)$. The parameters involved in the simple theory affect more than one of these curves.

The question of saturation, as mentioned above, is not explicitly covered by this simple theory. The analysis is dependent upon the ratio of a-c to d-c quantities being small, usually taken to be about 0.1. Even though the solutions for the unlinearized equations would not be the same as for the Mathieu Equation, it is not certain that the behavior would be qualitatively different.

V. EXPERIMENT

A. METHODS

In this experiment the behavior of r-f current and velocity waves propagating along a periodically varying (scallop) electron beam was investigated. Three parameters were varied during the course of the experiment: the magnetic field, allowing motion on the Mathieu diagram; the position of the exciting cavity, permitting complete investigation of initial conditions; and lastly, the power parameter, for possible saturation effects.

1. Experimental Conditions

The excitation frequency was 2917 Mc/s, and the power levels for most of the data were 8 mw for current and 1 w for velocity profiles. The 8-mw level was chosen as a compromise between the power available and the linearity characteristic of the detection equipment. The 1-w level was similarly chosen for suitable definition in the curves without incurring saturation effects.

Most of the basic components of the electron-beam analyzer used in obtaining the data for this report were those described by Gilmour¹⁵ and Hallock.¹³ The electron beam was electrostatically formed with an area convergence of 50:1 before it entered the magnetic field region. The beam emerged from a magnetically shielded gun with a leakage ratio of approximately $.004 (B_{\text{cathode}}/B_{\text{axial}})$. The cathode was pulsed negatively at a rate of 60 pps with a 16.7- μ s pulse width for a duty

cycle of .001. The accelerating voltage was 5200 v, and the peak power in this 1.15- μ perv beam was 2 kw.

Measurements were generally made with the pressure in the drift tube below 1×10^{-7} Torr. The chamber was maintained at these pressures by two VacIon pumps. It was constructed to permit the scanning mechanism on its set of two stainless-steel rods and the modulating cavity on its rods to be moved in and out of the vacuum chamber. There was no appreciable rise in the pressure and no waiting period between data runs.

The voltage pulse was adjusted to coincide with the zero of the filament current, eliminating effects of stray magnetic fields at the cathode. Even though the heater was a bifilar, non-inductively wound filament, Gilmour found disturbing effects on the otherwise perfectly uniform electron-beam cross-section for arbitrary phasing conditions.¹⁵

The fixed-frequency, doubly re-entrant cavity was attached to two rods enabling it to be moved along the scallop. Thus, excitation could be placed at any plane up to about 8 in. from the beginning of the drift tube, which is 1.25 in. from the anode exit of the gun. The drift tube was separated from the anode exit by a quarter turn 5/16-in. ID ball valve; in this manner, the gun region, pumped with a small VacIon pump, was continuously evacuated while the drift tube was opened for changes or repairs.

The magnetic field rose to its full value within a distance on the order of the beam diameter and was constant along the length of the drift tube whose usable length was 17 in. and diameter 4 1/4 in. Very

little scalloping, as low as a few per cent, was achieved near the Brillouin field of 285 gauss. The range of variation of the magnetic field in the experiment was from 180 to more than 550 gauss produced in the solenoid.

After passing through the cavity, the beam drifted along the tube until it impinged upon the combination scanner-collector mechanism. The scanner could be moved the entire length of the drift tube on its two 5/8-in. rods. The surface struck by the beam was carbonized to prevent secondary emission and had at its center a .010-in. hole. The Faraday cage, located about 1/32 in. behind the pinhole, was insulated from ground by a ceramic sleeve and received the minute portion of the beam which passed through the pinhole. The Faraday cage was attached by a flexible connection to a 50-ohm line formed by the stainless-steel rod and an inner copper rod. The cage entrance together with the pinhole formed a gap to detect r-f currents as well as d-c currents. The gap coupling coefficient was essentially unity, and the coaxial line was nonresonant for signal frequencies up to 6000 Mc/s. A schematic diagram of the electron-beam analyzer is shown in Figure 4.

2. Means of Taking Data

The untuned probe (pinhole and Faraday cage) could be positioned anywhere in the beam cross-section and was automatically driven through various sequential operations. R-f current data was taken by scanning horizontally across the beam, indexing the supporting

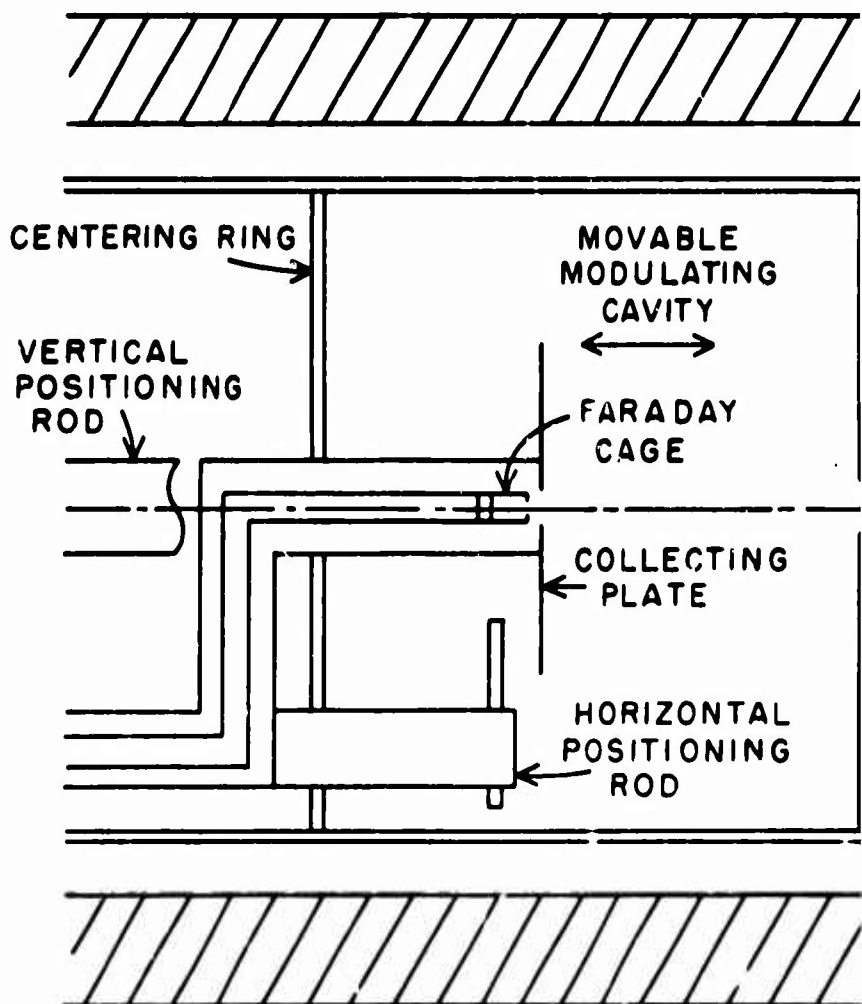
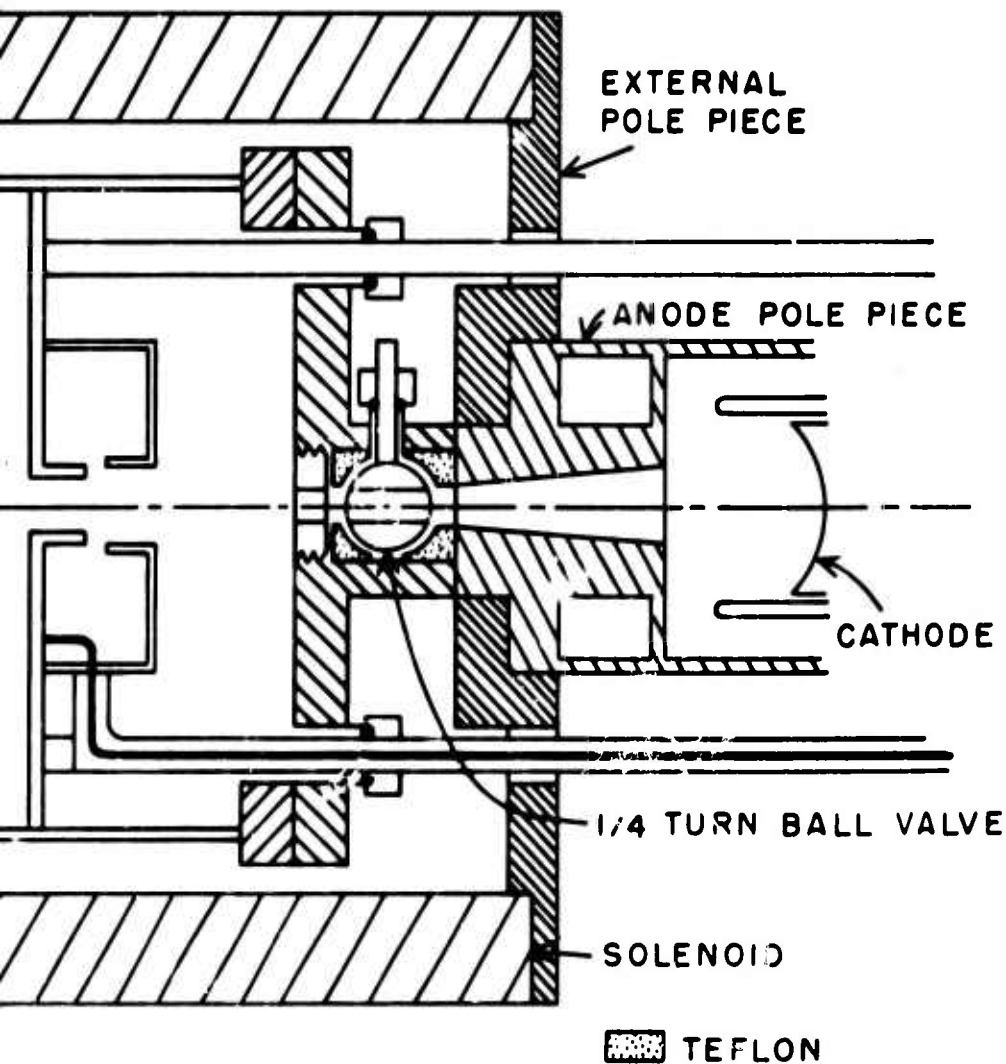


FIGURE 4. Schematic Diagram



m of Electron-Beam Analyzer.

carriage along the axis 0.4 in. and again scanning horizontally. This procedure was repeated along the entire length of the drift tube and took some fifteen minutes. D-c beam profiles were also taken in this automatic sequence to determine beam shapes. Most of the d-c current data used for scallop percentages were taken from scans at the center of the beam along the axis. From space-charge wave theory, it is known that the peak velocity with r-f drive applied varies as $I_0(\beta r)$. This function varies slightly for $\beta b \leq 1$. For this reason the velocity data from center-line scans was considered representative of the beam cross-section.

Measurements of d-c current were made by viewing the voltage developed across a termination resistor. R-f currents were first amplified in a low-noise TWT,* then mixed down to 30 Mc/s and amplified in two stages at this i-f frequency. The i-f signal was rectified, detected, and then displayed on an oscilloscope.

Velocity measurements were made using the technique of retarding field potentials. A voltage, approximately 5000 v in batteries, was applied to the cage allowing discrimination between small values of voltage at the 5200-v level. The current overcoming this bias passed through a 10-kM Ω resistor into an electrometer in which the input impedance was set at 10 M Ω . The voltage across the 10-kM Ω resistor

*Donated by RCA.

increased the bias, preventing the electrons with lesser energy from entering the Faraday cage. The electrometer amplified the .1 per cent of the bias appearing across its input; this output was then displayed on an XY recorder as a function of position. There was no difference in this procedure for measuring d-c or r-f potentials, as only peak velocities were measured. This measurement was interpreted as an indicator of the extent to which the velocity distribution had been altered. Only a small fraction of the high-energy tail on the distribution was collected. Knowledge of the velocity distribution could not be gotten from this measurement. The additional measurement of velocity distribution should be made for completeness, but is by its nature only a point determination. Because of the time needed for this type of measurement, velocity distributions were not measured in this experiment.

The current measurements on the other hand were more refined after detection and yielded much more information. The r-f or d-c current signals were displayed as time functions on an oscilloscope. An oscilloscope plug-in unit had as its output the trace amplitude at any desired 5-nanosecond interval along the pulse. Using this piece of apparatus, it was possible to display the current on an XY recorder as a function of two spatial dimensions (continuous in x and stepped in z) at any desired time in the pulse. With this technique, the effects of ions, pulse ringing, or finite rise and fall times could be eliminated. Conversely, it was possible to study in detail a spatial oscillation as a time function, or the effects of ions, if necessary.

Ion effects were easily detected if the pulse length was increased up to the limit of the pulser, $30 \mu\text{s}$. The data were taken at a time of $6 \mu\text{s}$ after the beginning of the $16.7\text{-}\mu\text{s}$ pulse used in the experiment. Voltages proportional to either the horizontal or axial positions were developed across helipot and were used to provide the two spatial dimensions on the XY recorder.

The velocity data, averaged over the pulse cycle, was reduced by measuring wavelengths and amplitudes directly from the XY recorder plots. The current data, however, had to be reduced by integrating the XY recorder plots to find the area representing a slice of the annular current. The total annular current was finally obtained by multiplying each annular slice by the radius extending to its centroid.

Because of the formidable task of reducing the r-f current data, a decision was made to use the more readily obtained velocity data if possible. Extensive r-f current data were taken at one value of magnetic field and many cavity positions (at each $1/8$ th of the cycle) and compared to velocity data taken under the same conditions. As the optimum growth rate and the effects of varying the excitation plane were essentially the same, it was concluded that a comprehensive study of velocity distributions (in co-ordinate space and not in velocity space) on the beam would be sufficient to characterize the general problem.

The experimental procedure for measuring gain rates was to vary the magnetic field in steps of approximately 7 gauss, with the cavity placed at the optimum growth position in each case. Investigation of position effects was made at certain magnetic fields with cavity increments of about $1/32$ nd of the scallop wavelength.

3. Sample Data

Sample data of r-f current distributions are shown in Figure 5. Figures 5a and 5b present the growing and decaying conditions on a scalloping beam; Figure 5c shows the stable propagation of space-charge waves on the Brillouin beam (in the strict sense). Figure 6 gives a detailed plot of the d-c current density on the beam used for the data in Figures 5a and 5b. The r-f current data actually used were recorded at much higher sensitivities to facilitate accurate readings on the integrating planimeter used for data reduction.

Most of the gain rates and scallop percentages were determined from the data shown in Figure 7. The interesting growth of the velocity profiles at the end of the drift tube for the higher values of magnetic field is actually an increase in the no-signal peak velocity. The last curve in Figure 7a is taken with no signal applied to the cavity and shows the growth of the peak velocity of the beam. This phenomenon is discussed more fully in section VD. The data shown in Figure 7b are the d-c currents at the center of the beam as a function of distance along the drift tube for different magnetic fields.

Data showing the distribution of r-f and d-c current across the cross-section of a beam are given in Figure 8. It is seen that the r-f current does lie in the annulus described by the outer shell of the beam and that the d-c current is uniform across the beam. (This data was taken by the author using an identical gun which did not have provisions for a sliding input cavity.)

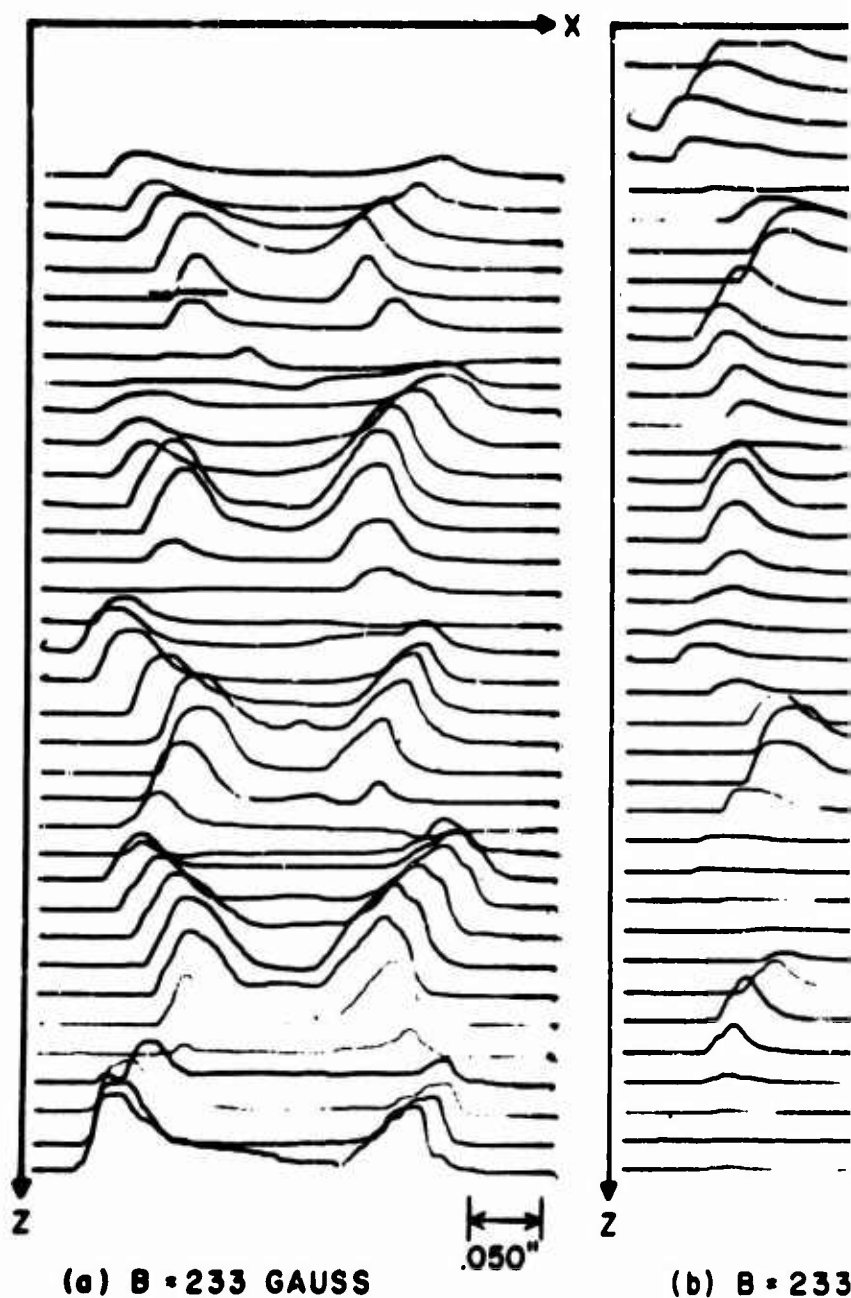
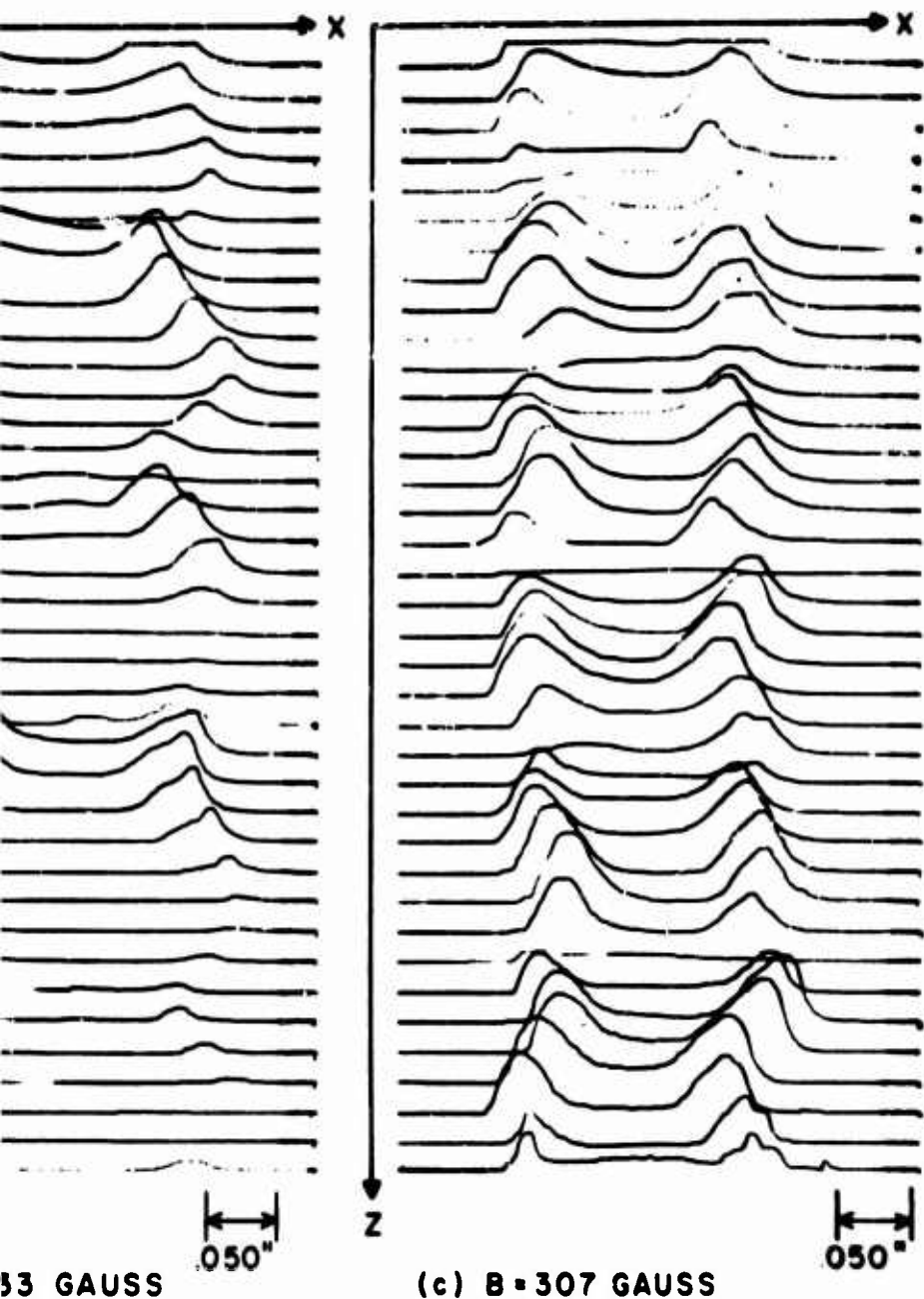


FIGURE 5. Sample Data of r-f C. Optimum Position for Amplification, Attenuation, c) Space-Charge Wave



Current Distributions. a) Cavity Placed at
 ion, b) Cavity Placed at Optimum Position for
 ave Propagation on the Strict Brillouin Beam.

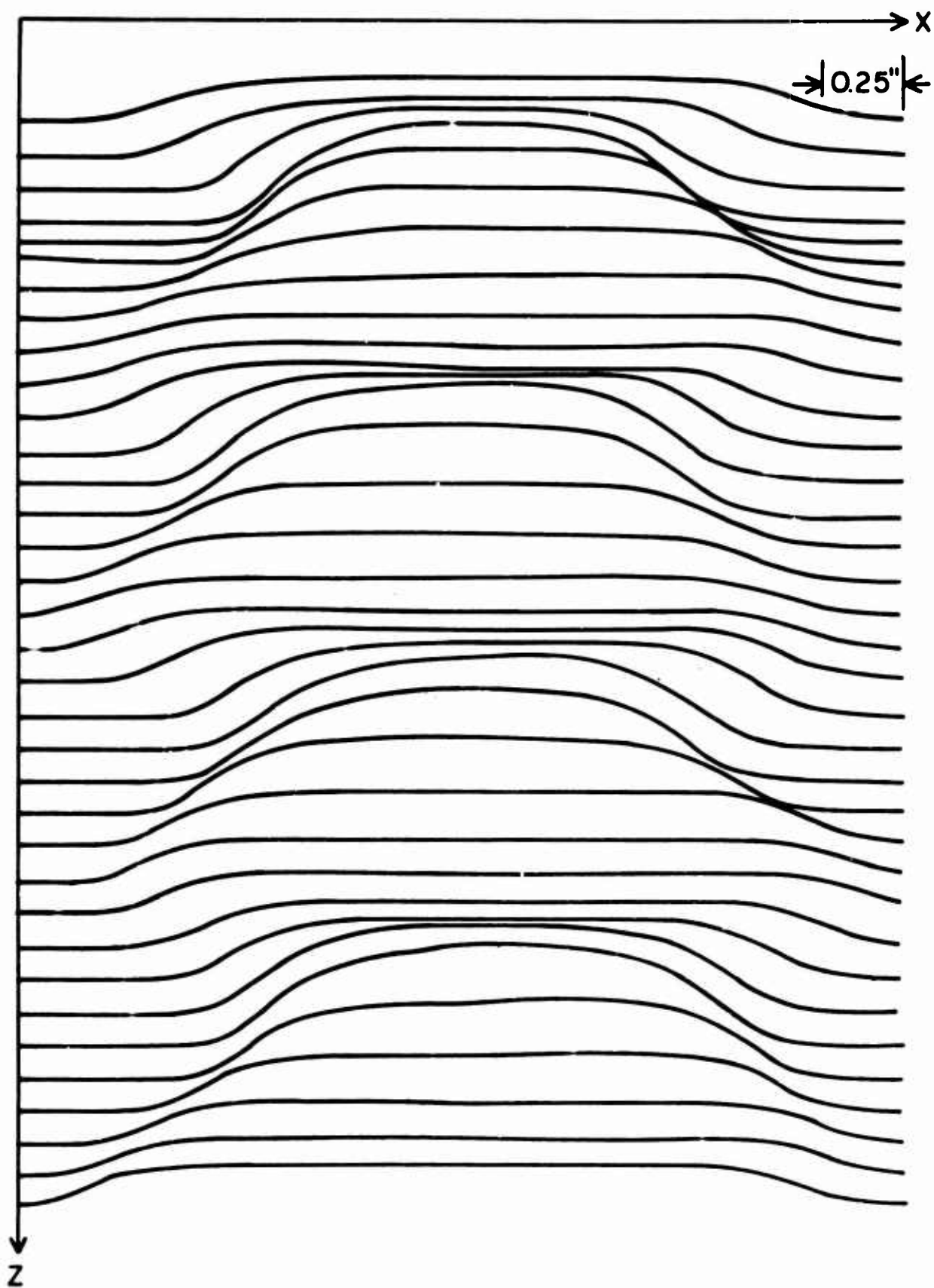


FIGURE 6. Sample Data of D-C Current Distribution on Scalloping Beam.

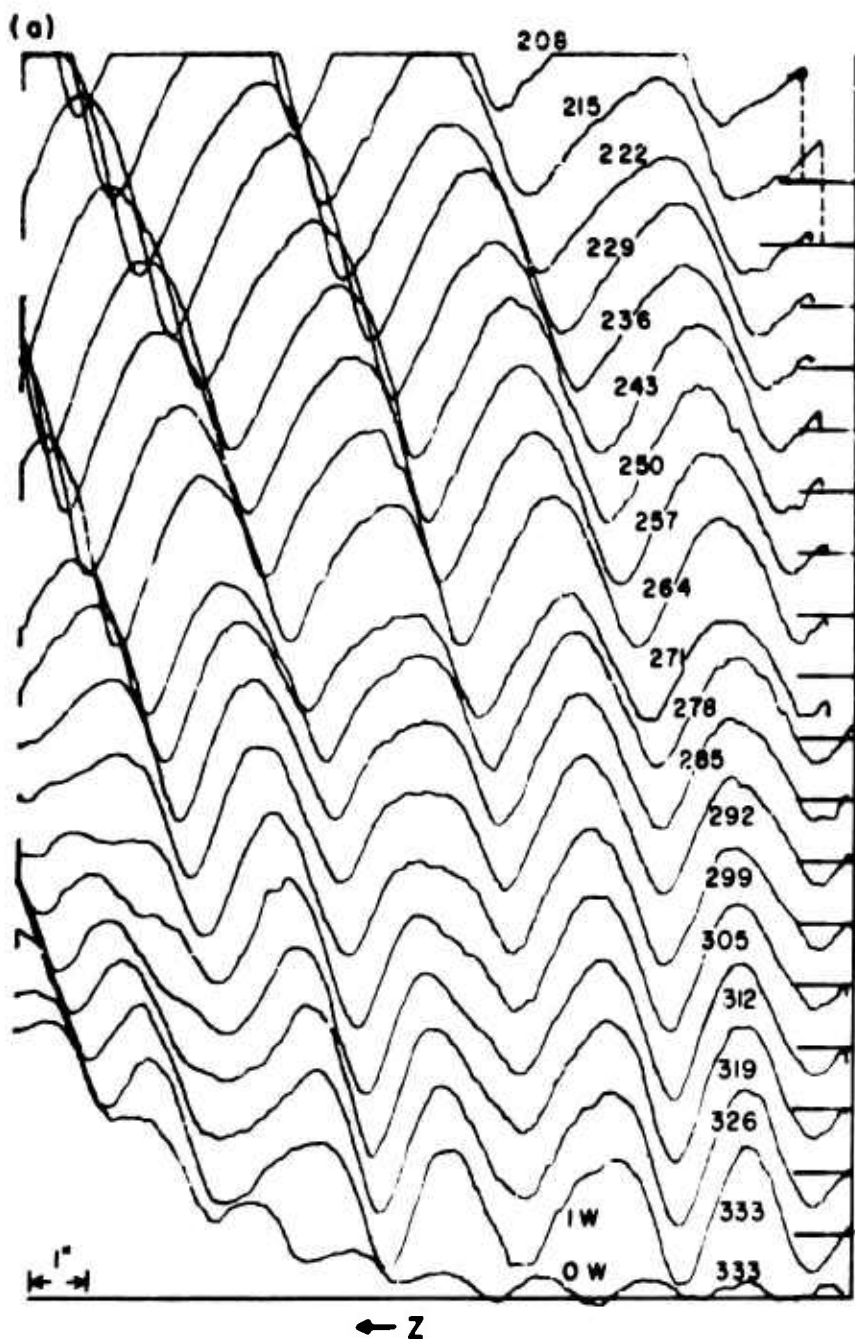


FIGURE 7. Peak Velocity and D-C Current (a) Placed at Optimum Position for Amplification (signal peak velocity), b) D-C Current a

(b)

B (GAUSS) •

208

215

222

229

236

243

250

257

264

271

278

285

292

299

305

312

319

326

333

PEAK R-F VELOCITY

← Z

current along the Axis. a) Peak Velocity with Cavity
location in each Case (Last curve shows growth in no-
along the Axis for Corresponding Magnetic Fields.

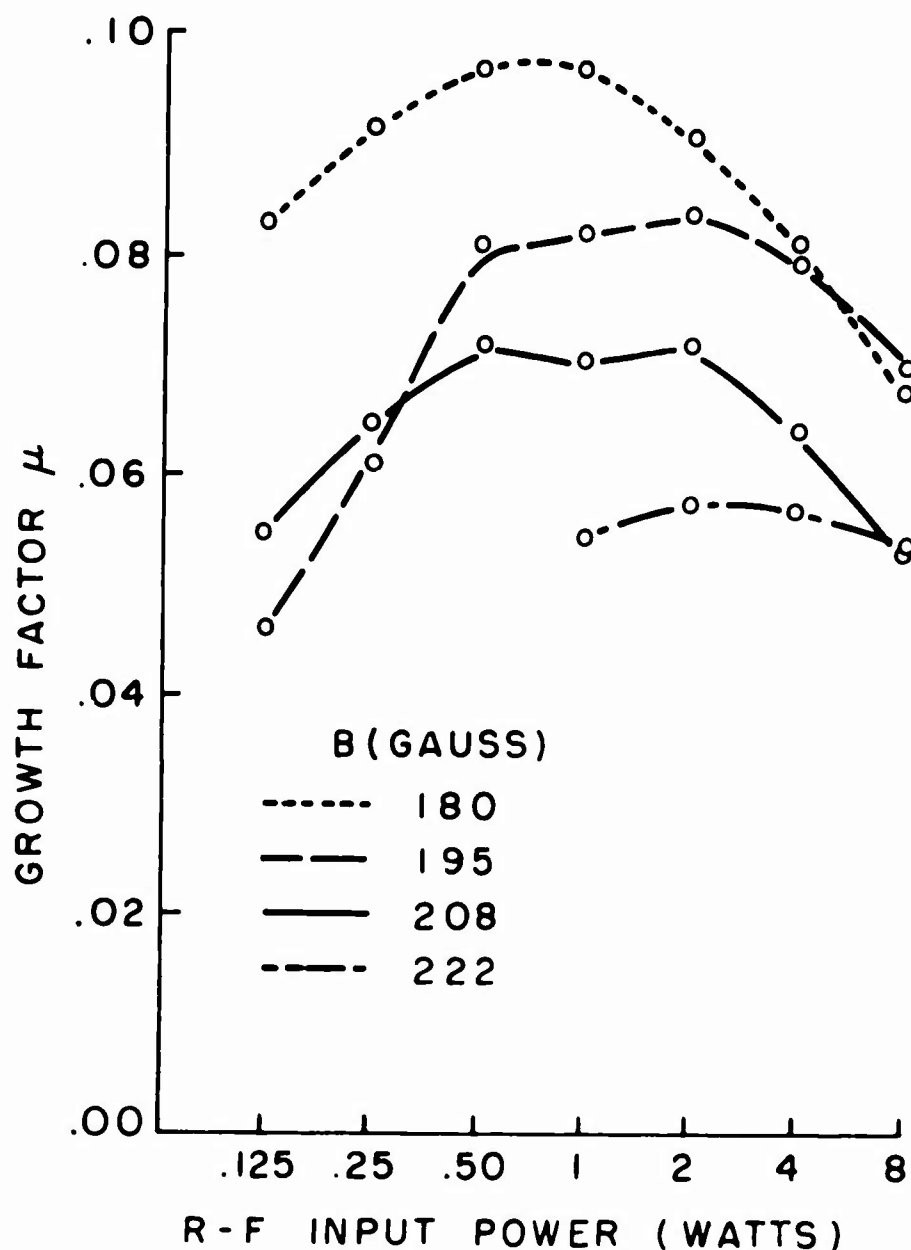


FIGURE 8. R-F and D-C Current Distributions at a Beam Cross-Section.

4. Experimental Difficulties

The electron-gun assembly built for this experiment became misaligned during the final stage of construction. External machining was done to restore the tolerances, but the resultant beam entered the field at some angle causing a cyclotron spiral. After some investigation, it was concluded that the mechanical warping altered the symmetry of

the magnetic field paths in the interior of the gun and could not be repaired. Eliminating the construction faults of the previous gun, a design for a new gun assembly was prepared and executed. The new gun was accurately aligned mechanically, but still produced a spiraling beam. Electromagnetic degaussing reduced the amplitude of the spiral, but a residual level could not be eliminated. In this case it was concluded that an asymmetry in the magnetic material of the gun near the cathode was probably at fault.

Lesser difficulties were experienced with the vacuum system, the scanning mechanism, the detection equipment, the r-f shielding, and the secondary emission problem.

B. VALIDITY OF THE ASSUMPTIONS

The validity of the various assumptions made in the analysis is discussed in terms of the actual conditions of this experiment.

1. Laminar Flow. The question of laminarity was the subject of a report by Hallock¹³ on the Sperry STL-100 TWT gun. The general result was verification that the optics of this gun were reasonably good. The calculated Brillouin field did provide the least amount of scalloping (a few percent), within the experimental accuracy. Small translaminar streaming was detected, however, and its effect appeared to be a shortening of λ_s by a few per cent from the predicted laminar value. The design for the gun used in this experiment incorporated the critical dimensions of the STL-100 gun. However, difficulties arose with the appearance of aberrations that seemed to be large translaminar currents.

These disturbing electrons were eliminated by recarbonizing the collector plate to suppress secondary emission. Thus, the assumption seems justified for all but a few percent of the electrons in the beam. The discussion below shows that the small translaminar currents play an important role in determining accurate quantitative results.

2. Single Velocity. Although there was no actual check on the velocity spread of the quiescent beam in this experiment, previous measurements of this type¹⁶ have shown the spread about the nominal beam voltage to be less than 5 percent. Further experimental work is necessary to determine the actual effect of the small velocity spread.

3. Sinusoidal Perturbation. Since the excitation was from a stable klystron feeding a sharply resonant cavity, this assumption can safely be considered valid here.

4. Small-Signal Level. For the current and velocity data, the powers used were 8 mw and 1 w, respectively, on the 2-kw beam. These ratios would appear to insure small-signal behavior. As is discussed below, however, saturation effects were observed when the input power was on the order of 8 w.

5. Strong Magnetic Field. This assumption was made for the initial analysis and was relaxed subsequently so that it has no bearing on the experiment. Implicit in the notation was the constancy of many quantities with axial position, in particular, the magnetic field. This property was measured by Gilmour¹⁵ on this apparatus and found to be constant along the entire usable drift tube.

6. Beam Open Circuit to a-c Currents. This requirement is in two parts, the first with respect to a-c current on the beam before

modulation, and the second regarding transverse modulating fields.

There are certainly no r-f currents on the beam prior to the cavity other than the possible noise components at this frequency. Perturbation measurements of the field were not made on this cavity, and one can only take this part of the assumption as possible if detailed calculations are not made. In fact, Beck¹¹ proceeds with the analysis in a different fashion in which there is no requirement for a vanishing transverse field.

7. Small Scalping. Experimental determinations showed the maximum degree of scalping to be about 35 per cent, where by this is meant the deviation of the normalized maximum or minimum radius from unity. This measurement was made by taking the square root of the axial current-density variation. Reduction of the continuous axial current-density plots, as in Figure 7b, was more accurate than reduction of the stepped plots of $I(x, z)$, as in Figure 6, showing the variation of the radius. Even for scallops as large as 35 per cent, the edge equations (solved to third order by iteration procedures⁶) predict sinusoidal behavior. Although the radius varied essentially as a sine wave, the current density for the large scallops was departing from simple sinusoidal behavior. This assumption has questionable validity and would certainly be difficult to justify for any larger scalping.

8. Lossless System. Small systematic changes in the scallop amplitude could not be detected because of the small cyclotron spiral of the beam. The saturation or lessening of the gain rate observed at r-f signal levels of 20 w implies the validity of this assumption for smaller signal levels. As the probable cause of the saturation is the

r-f signal level being an appreciable fraction of the transverse energy, this assumption must be relaxed if the saturation effect is to be analytically treated.

9. Traveling Waves. Phase measurements were not made during this experiment. It is taken as a matter of fact, along with the existence of the standing waves, that this assumption is valid.

10. Plasma-Reduction Factor. The reduced wavelengths calculated with the published reduction factors¹² agree well with the experimental findings over most of the stable region of operation. Throughout the unstable region, the plasma wavelengths were identically equal to the scallop wavelengths; therefore no direct check on these values could be made. The predicted wavelengths were, however, used as the unperturbed wavelengths in the theoretical gain rate calculations, and one can say the assumption is justified in the general success of the model.

11. Drifting Beam. Peak velocity measurements taken along the axis with no signal applied to the cavity showed only a variation of a few volts in 5200. This variation was traced to the slight skew caused by the cyclotron spiral. Thus, this assumption is acceptable.

12. Brillouin Beam. This assumption implies no positive ion neutralization, an exact balance of forces, and no flux through the cathode. Measurements usually showed no ions present during the 16.7- μ s pulse used. Displays of the output current pulse showed constant amplitude along the entire pulse width. By increasing the pulse width to 30 μ s, the presence of ions was detected as the increasing or decreasing of total current depending upon axial position.

The second implication of this assumption was certainly not true for this experiment, because it was designed to show whether or not reduction factors for strict Brillouin beams could be used for scalloping Brillouin beams of which the equilibrium radii were used as equivalent Brillouin beams.

The implication of no cathode flux was found by Hallock¹³ to be incorrect. He calculated a flux-leakage ratio of $B_c/B_{axis} = .004$, resulting in a few percent decrease in the scallop wavelength.

In summary, this assumption was found to be substantially correct except for the effect of the cathode flux, which can be taken into account during the calculations.

13. A Large Ratio of Wall-to-Beam Radii. The actual value of the ratio was about 25/1, depending upon the axial position. As the reduction factor curves vary almost not at all for the ratio greater than two, this requirement is completely satisfied.

14. Lowest Radial Mode of Propagation. This last assumption is considered valid because the entire experimental system is axially symmetric, and there should be no excitation other than that uniform with angle.

Most of these assumptions were verified completely on experimental grounds. The only invalid, apparently critical assumptions concern the fraction of a percent of flux in the cathode and the small trans-laminar streaming of electrons. The correction for cathode flux is found from a straightforward extension of the laminar theory. The

correction for the translaminar streaming must be made on the basis of experimental measurements.

C. DISCUSSION OF THE PREDICTED RESULTS

1. Maximum Growth Rate

The experimental gain rates as shown in Figure 9 were mostly calculated by setting the ratio of adjacent standing-wave maxima equal to the factor $\exp \mu \pi$ and finding the average μ over the number of scallops in the trace. The smaller growth rates were determined by measuring the slope of the line drawn through the maxima of the standing wave and setting this equal to the initial slope of the exponential $\mu \pi$. The agreement is seen to be within experimental error, although there is some gain at field strengths above the theoretically possible value. The values for the solid line were calculated by finding A from the calculated values of scallop (corrected for the small amounts of cathode flux and translaminar electrons) and reduced plasma wavelengths. Next, q was found from the calculated curve of $(q/\Delta)_0$, the calculated value of A , and the measured value of the scallop percentage as shown in Figure 9b. It was necessary to fit the curve $p/\beta b$ versus βb with the equation:

$$\frac{p}{\beta b} = \frac{1}{2(\beta b)^{\frac{1}{2}}} \left[1 - \left(\frac{\beta b - .75}{10} \right) \right], \text{ for } .75 \leq \beta b \leq 1.5$$

to obtain values for the slope m needed in the q/Δ relation.

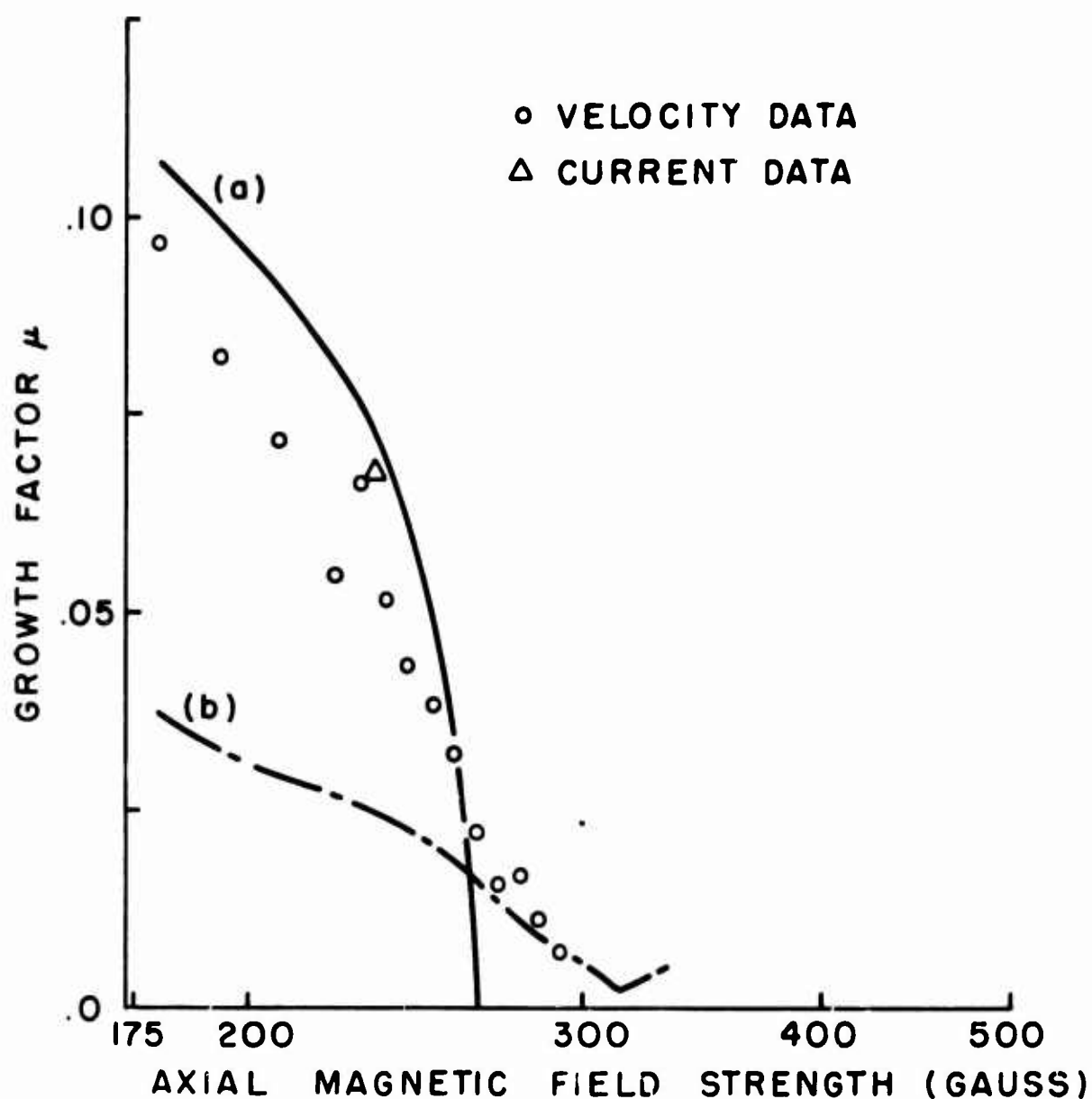


FIGURE 9. Growth Factor μ and Percentage Scalping versus Axial Magnetic Field Strength. (a) Curve is Plot of Calculated Values of the Growth Factor μ ; (Data points are experimental results measured on velocity and current profiles along the axis.) (b) Curve is Plot of Measured Values of Percentage Scalping. (Ordinate scale is multiplied by 1000.)

The maximum gain rate achieved experimentally was $\mu = .097$, which corresponds to 2.64 db/scallop or 0.61 db/cm. This figure is not competitive with those attainable in existing devices, but must be considered as an important secondary instability.

It should be noted at this point that the effect of the cathode flux and slight translaminar behavior is significant. Calculations of A and q based strictly upon the assumptions (including no cathode flux and laminar flow) yield values of μ that are essentially zero over the entire unstable region of operation in this experiment. It is apparent that these two types of non-ideal behavior and their effects on the scalloping need to be known to at least a first-order approximation for quantitative calculations. The occurrence of this sensitivity is apparently caused by the form of the reduction factor which varies rapidly for βb less than unity and slowly for βb greater than unity. Reference to Figure 12 below shows that the plasma wavelength varies nearly as the scallop wavelength below the Brillouin field, and rather differently than the scallop wavelength above the Brillouin field. A slight shift in the scallop values is seen to have a large effect on the value of A in the growth region. A comprehensive discussion of the necessary corrections to the simple theory is contained in the section entitled "Wavelengths."

Negative growths or decays were also measured, but not with sufficient accuracy to allow meaningful quantitative comparison at this point. This matter is discussed as a part of the following topic.

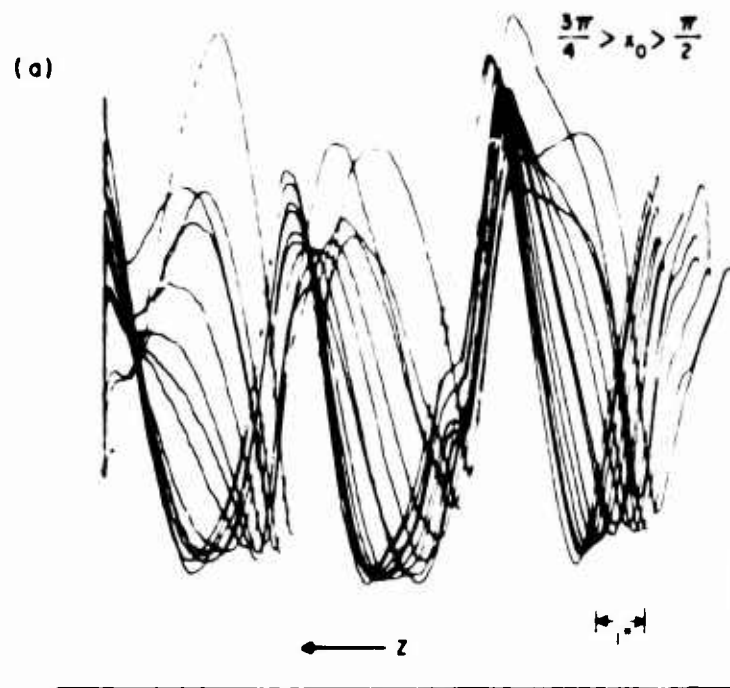
2. Cavity Position

Effective gain rates averaged over the scallops available were taken from the data in Figure 10 and plotted in Figure 11 along with the curve of calculated gain rates versus cavity position. The growth rates are not very reliable near $x_0 = \pi/4$ and $3\pi/4$, as only a few scallops could be measured at these cavity positions at one extreme, and as the behavior was nonuniform at the other extreme position. (The non-uniform behavior is discussed in the next section.) It can be seen that at these relatively low gain rates, just over half the scallop cycle produced gain although the calculated values indicated a wider range for growth. Because these data were taken at 10-w drive level to achieve sufficient definition, some saturation effects are present. These effects have caused the highest gain rate to be lower than the maximum available at this magnetic field.

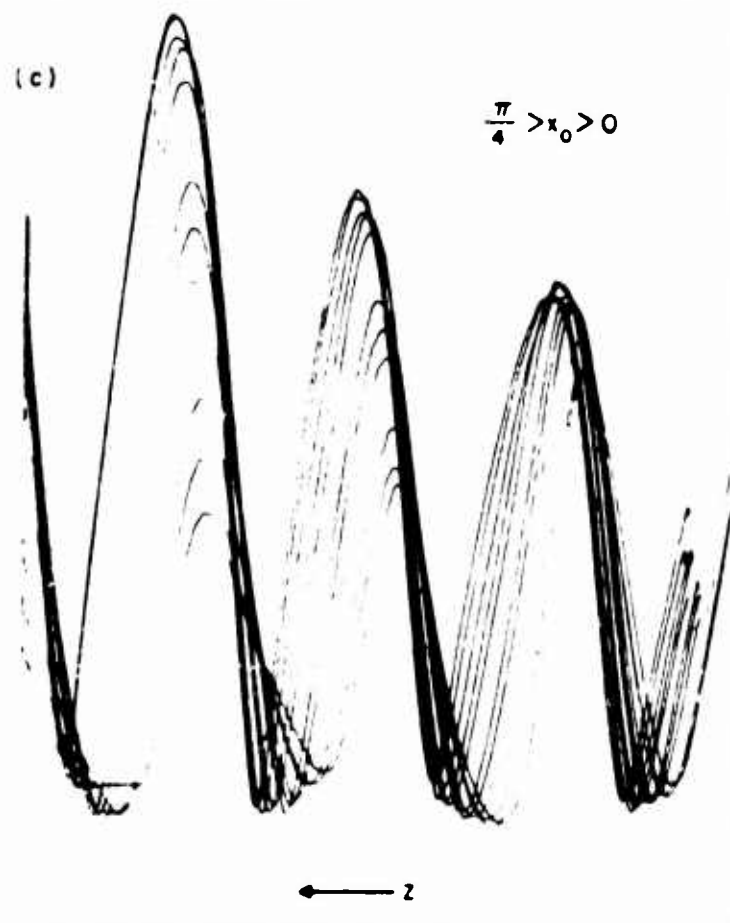
Although gain was realized with the cavity placed over a range of half the scallop cycle, only a very small portion of the scallop led to the maximum gain available. This verifies that at low gains, at least, the gain-position curve is not flat-topped, which necessitates careful placement of the cavity to obtain the maximum possible amplification.

3. Wavelengths

Figure 12 shows plots of the theoretical plasma half-wavelengths and scallop wavelengths. The curve (c) represents scallop wavelengths measured on the beam edge by Gilmour¹⁵ and again by Hallock.¹³ Curve (d) is a plot of the theoretical cyclotron wavelengths. In addition to the

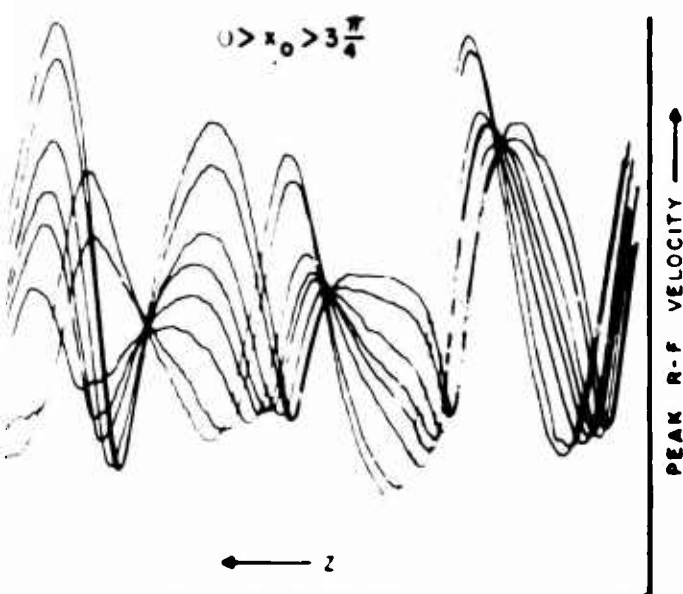
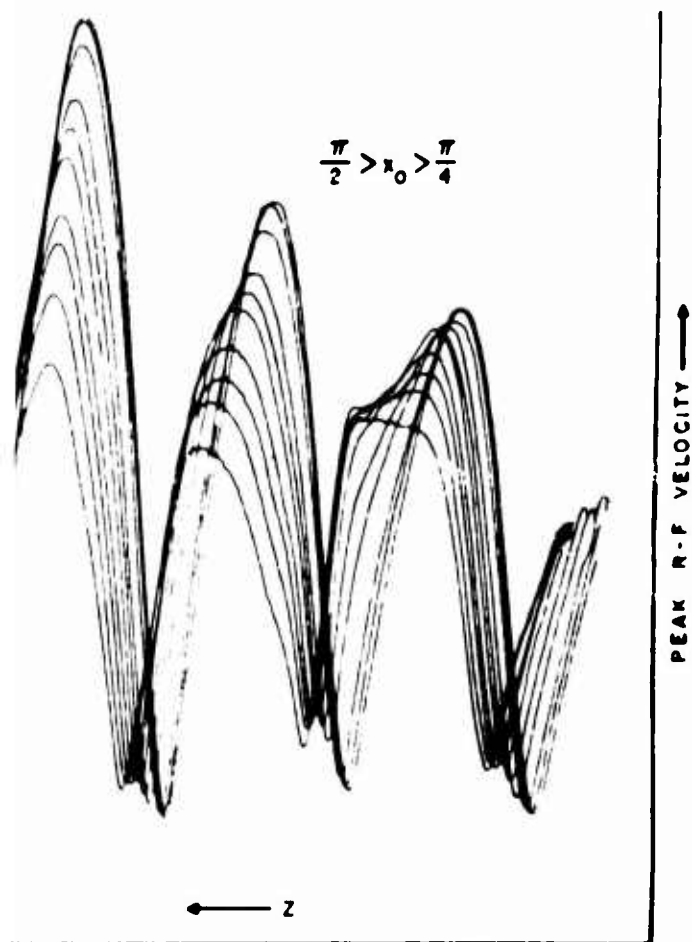


(b)



(d)

FIGURE 10. Peak-Velocity Standing Waves along the Scalloped Beam with 10-w Drive Level and a Magnetic Field Strength of 209 gauss (Figures a, b, c, and d show a Continuous Variation of Cavity Position through a Full Scallop Cycle Starting with $x_0 = 3\pi/4$).



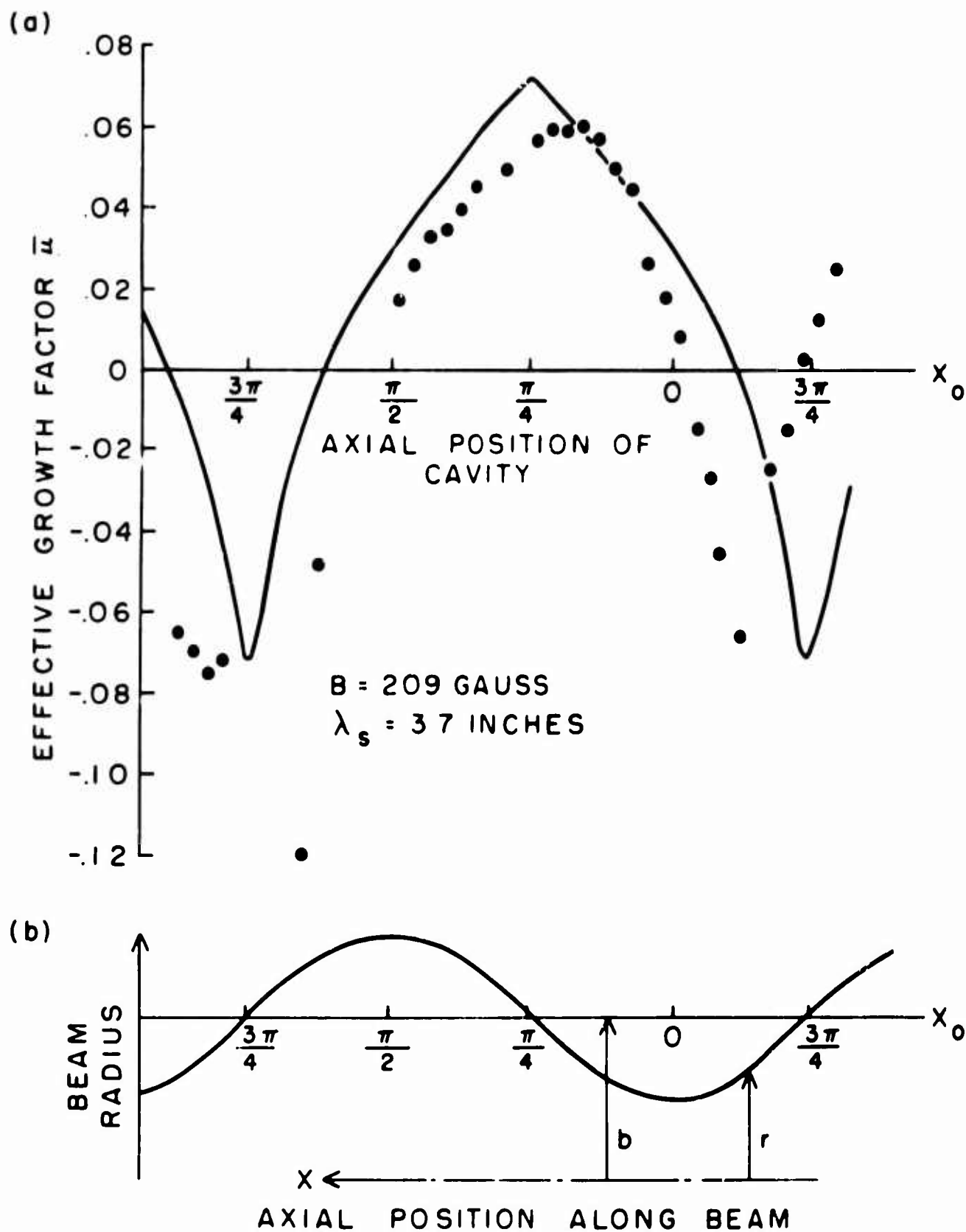


FIGURE 11. a) Curve Shows Plot of Theoretical Effective Growth Factor versus Position of Cavity; Data Points are Experimental Results under Corresponding Conditions; b) Plot of Beam Radius Corresponding to Cavity Position.

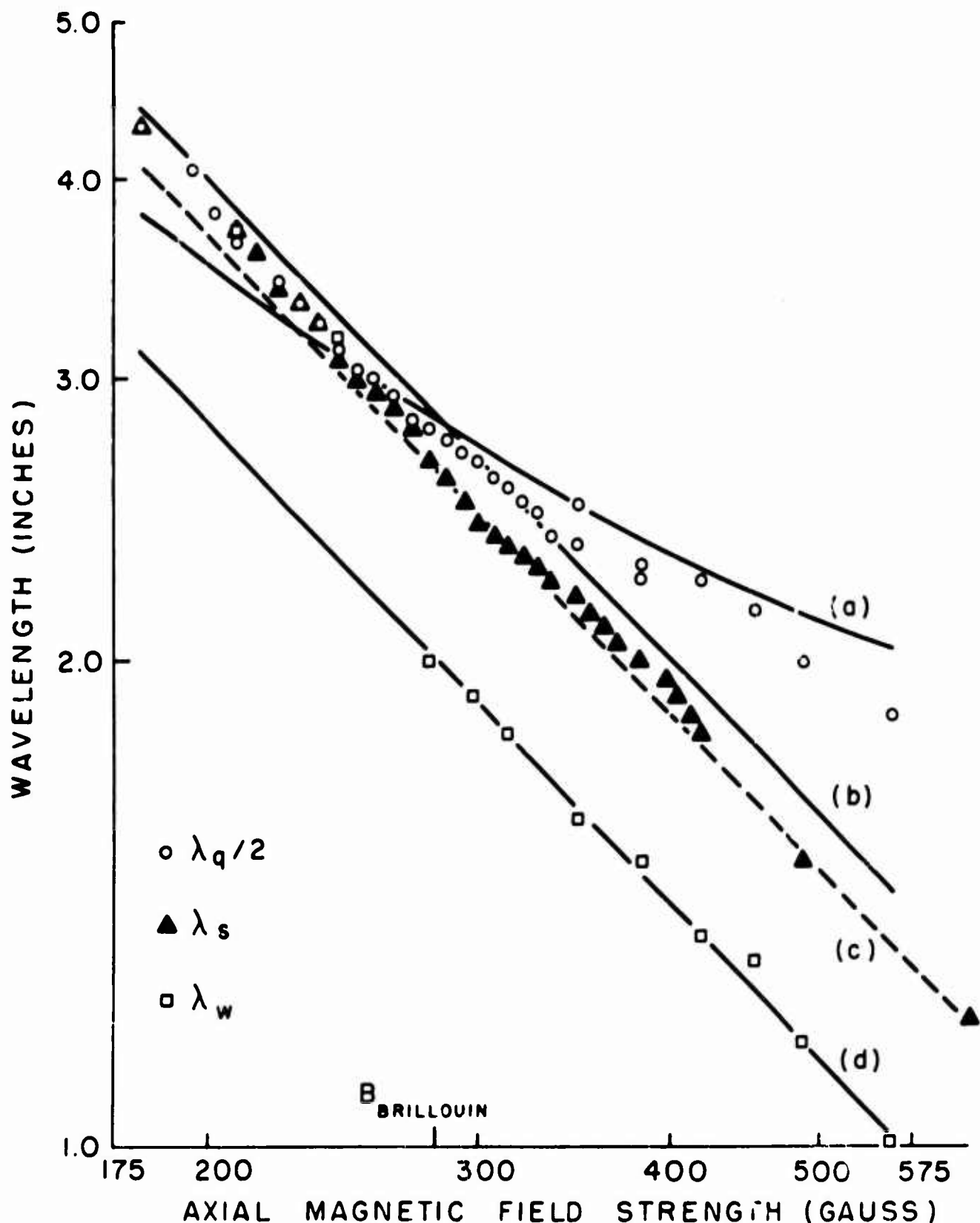


FIGURE 12. Wavelengths versus Axial Magnetic Field Strength; (a) Plot of Theoretical Effective Plasma Half-Wavelength (b) Plot of Theoretical Scallop Wavelength with No Cathode-Leakage Flux, (c) Plot of Measured Scallop Wavelength at the Beam Edge, (d) Plot of Theoretical Cyclotron Wavelength; Data Points Are from Experimental Results Using r-f and d-c Peak Velocity and d-c Current Measurements

measured values of $\lambda_q/2$ and λ_s , there are experimental data labelled λ_w where w stands for wobble.

The plasma wavelengths were calculated using the relation for an unscalping Brillouin beam $\omega_p^2 = 1/2 \omega_c^2$ which resulted in $\lambda_q = \sqrt{2}/p \lambda_c$. The values for the scallop wavelength were calculated using another Brillouin beam relation $\lambda_s = \sqrt{2} \lambda_c$. The reduction in beam velocity caused by finite dimensions was calculated by Gilmour¹⁵ to be 5 per cent.

It is interesting to notice that for $\beta b = 1$, p is essentially equal to $1/2$ making $\lambda_q/2 = \lambda_s$. Reference to Figure 12 shows that for the condition $A = 1$, i.e., where curves (a) and (b) intersect, the magnetic field is equal to the Brillouin value for this beam voltage. Thus, we can make the statement that for a Brillouin beam with $\beta b = 1$, the scallop and half-plasma wavelengths are coincident at the true Brillouin value of magnetic field. This line of reasoning also leads to interesting results concerning the possible gain rates on the special $\beta b = 1$ Brillouin beam. For this particular kind of beam, $A = 1$ right at the Brillouin field and becomes larger or smaller as the field is lowered or raised. At the same time, however, the percentage scalloping (for the theoretical Brillouin beam we are discussing) is zero where $A = 1$ and increases as A is changed from unity. Thus, it is not at all possible to attain favorable gain conditions under these circumstances. In fact, if one could make a perfect Brillouin beam with $\beta b = 1$, there would apparently be two regions of slight gain with an absolute null at the Brillouin value.

The experimentally determined plasma wavelengths appear to agree reasonably well with the theoretical values. The disagreement at the higher-field values can possibly arise from the presence of the anomalous velocity growth referred to previously. As the magnetic field was increased beyond the Brillouin value, the velocity profiles showed increasingly disturbed standing waves. This disturbance, making meaningful averaging impractical, probably accounts for the disagreement, and is discussed in the next section.

The plasma half-wavelengths below the $A = 1$ field strength are seen to correspond exactly with the scallop wavelength, showing conclusively the locking phenomenon already discussed. Data of this form, as reported by Gilmour,¹⁷ motivated, in part, construction of a sliding modulating cavity for this study of scalloped-beam phenomena. Figure 16 of Gilmour's report shows evidence of the locking phenomenon beginning at a magnetic field strength of approximately 205 gauss. Similar experimental results presented in Figure 12 of this report show the critical magnetic field to be about 270 gauss. This difference is easily reconciled by remembering that different frequencies were used in the two experiments. Gilmour's work was performed at 1940 Mc/s making βb smaller for a given magnetic field. This, in turn, comparatively reduces p , which increases λ_q and shifts the synchronous point to lower magnetic fields; thus agreeing with the previous statement that increasing the frequency will shift the synchronous point, and correspondingly the gain region, to higher magnetic field strengths.

A thorough study of the scallop wavelength and its variation with the two parameters of interest here, cathode flux and translaminar currents, was made by Hallock on the same apparatus used in this experiment.¹³ He showed that, by allowing flux in the cathode, the laminar theory predicted a shortening of the scallop wavelength. The form of the variation caused by the flux is identical to that taken by the scallop data in this experiment (represented by triangles in Figure 12). For the leakage ratio of about .004 applicable to this experiment (determined by Hallock), the shortening appears to be a few percent at low magnetic fields and nearly 7 percent at higher fields. Even with this refined theory, it was not possible to explain the scallop data taken by Gilmour (represented in Figure 12 by the dashed line). The anomaly was eliminated by hypothesizing the presence of a small, violently oscillating translaminar stream that moved with a wavelength much shorter than the actual scallop wavelength. As there was also flux through the cathode, the translaminar current could not go through the axis, and therefore would not affect the axial electrons as much as the electrons spread throughout the beam and near the outer edges. Hallock verified this theory by measuring the scallop wavelengths along the axis and also along the beam edge. The wavelengths measured along the axis corresponded to the values predicted by the laminar theory, i.e. to the triangles in Figure 12 which are the results of measuring velocity profiles along the axis of the beam. The wavelengths measured along the beam edge corresponded to the anomalous values represented by the dashed line in Figure 12. There is then clear proof that the

translaminar stream "pulls" the scallop wavelength at the beam edge and throughout the body, with the smallest effect at the axis.

Experimental evidence of velocity across the diameter of the beam shows no variation which is symmetric about the center. These data tend to support the view that the beam is laminar, except for a small translaminar stream, and is not undergoing laminar shear. The model of laminar shear predicts a gradual change in wavelength from edge to axis. On the other hand, the laminar model with a translaminar stream predicts that most of the change in wavelength will occur near the axis.

Since it is apparent that the values of μ are closely tied to the values of A which, in turn, are closely related to λ_s , the question arises of which curve of λ_s to use. As was stated before, use of the theoretical values given by curve (b) results in zero values for the gain rates. The question is answered by considering which electrons interact with the plasma wave. The majority of electrons that are scalloping (and only these help produce gain) are located in the central and outer portions of the beam cross-section, where the actual wavelength has been shortened from the predicted value. In addition, the r-f current wave is entirely on the surface of the beam where it would encounter only the reduced scallop wavelength. For these reasons, it is necessary to use the actual edge value of the reduced scallop wavelength. The calculations based on this argument lead to reasonable agreement, as shown in Figure 9. The same calculations using the laminar theory would result in much lower values for the gain rates.

It is from the beam-edge reduced-scallop-wavelength measurements that the -7 per cent correction figure arises. At the lower than Brillouin fields, approximately 3 per cent of this amount is caused by the cathode flux and the remaining 4 per cent by the translaminar stream.

Another observation can be made concerning the interaction of plasma and scallop wavelengths. In the region of magnetic field from about 340 gauss down to the critical value of about 270 gauss, the plasma and scallop wavelengths appear to be resisting the locking forces. At the critical magnetic field strength, the gain rate is apparently high enough to cause locking. It is interesting to note that it is at this magnetic field that the behavior of the λ_w changes from the expected cyclotron values to the scallop values also. This second locking phenomenon attests to the forces involved in the scalloping beam.

The λ_w were measured as the periods of the no-signal axial velocity variations. Above field strengths corresponding to $A = 1$, this wobble is seen to be equal to the cyclotron wavelength as expected. The slight cyclotron spiral is sufficient to produce a few volts variation in velocity across the beam, as if it were spreading on one side more than on the other side. Thus, taking a profile of peak velocity down the axis of the drift tube actually samples the velocity at various locations in the beam as it spirals about the center line. This results in a few volts variation on top of the beam voltage. At magnetic fields below the $A = 1$ value, however, the wobble period becomes identical to that of the scallop variation.

It should be stated that all the plasma wavelength data in Figure 12 are taken from peak velocity measurements, as are the wobble wavelengths with no signal applied. The scallop data are determined from the axial current-density profiles. The wavelengths given as plasma half-wavelengths are true values in that they are all periodic with no apparent phase shift between minima. This condition is not that predicted and will be discussed in section VD. The current data did, however, show the minima shift and, in general, cannot be assigned simple wavelengths.

4. Effect of the Magnetic Field Parameter

Figure 1 shows the path of operation taken in this experiment by changing the magnetic field. Starting at the upper right-hand point of the line near $\mu = .1$, the magnetic field is about 180 gauss and is continually increased to about 600 gauss. The line which stops, however, at $q = 0$ only describes the field variation up to about the Brillouin value. This should cause no concern as the Mathieu diagram is symmetric about the ordinate, and the operating line continues along its diagonal extension. The theory would seem to suggest that higher gain could be attained by simply increasing the accelerating voltage; in this case only q would be affected and not A by the change of parameter. The general behavior of this line corresponds to the predicted variation in section VD, i. e. an upward diagonal line for a decreasing magnetic field.

5. Shift in the Minima

One result of the analysis is that the periodicity of the space-charge wave in the unstable region be that of the scallop variation. Also, excitation at an arbitrary plane will give rise to a shift in the minima to the position of the growing solution, $x_0 = \pi/4$. Figure 13 presents the reduced data of r-f current standing waves for four different cavity locations on one side of the optimum position. Careful study of this data shows the curve at the optimum location is strictly periodic, with a period of the scallop at that magnetic field. The other three cavity positions shown, however, yield aperiodic waves. The initial planes of excitation are all equally spaced, whereas at each succeeding group of minima, phase shifts occur in the three waves. By the end of the drift tube, equilibrium is being established, and the minima have shifted nearer to the optimum position. A few calculations made (the general solution is very involved algebraically for A not equal to unity) showed close agreement with the measured minima shift. Anomalous behavior was noted on the part of the velocity waves which in general did not show minima shift and is discussed in section VD.

6. Curvature of the Standing Waves

A final check on the theoretical predictions can be simply made by looking at the shape of the envelope of the space-charge waves. Figure 14 shows a typical velocity profile taken along the center of the beam trajectory. The nonsinusoidal behavior is manifested by the difference in curvature between the two quarter-cycles. This asymmetry arises from

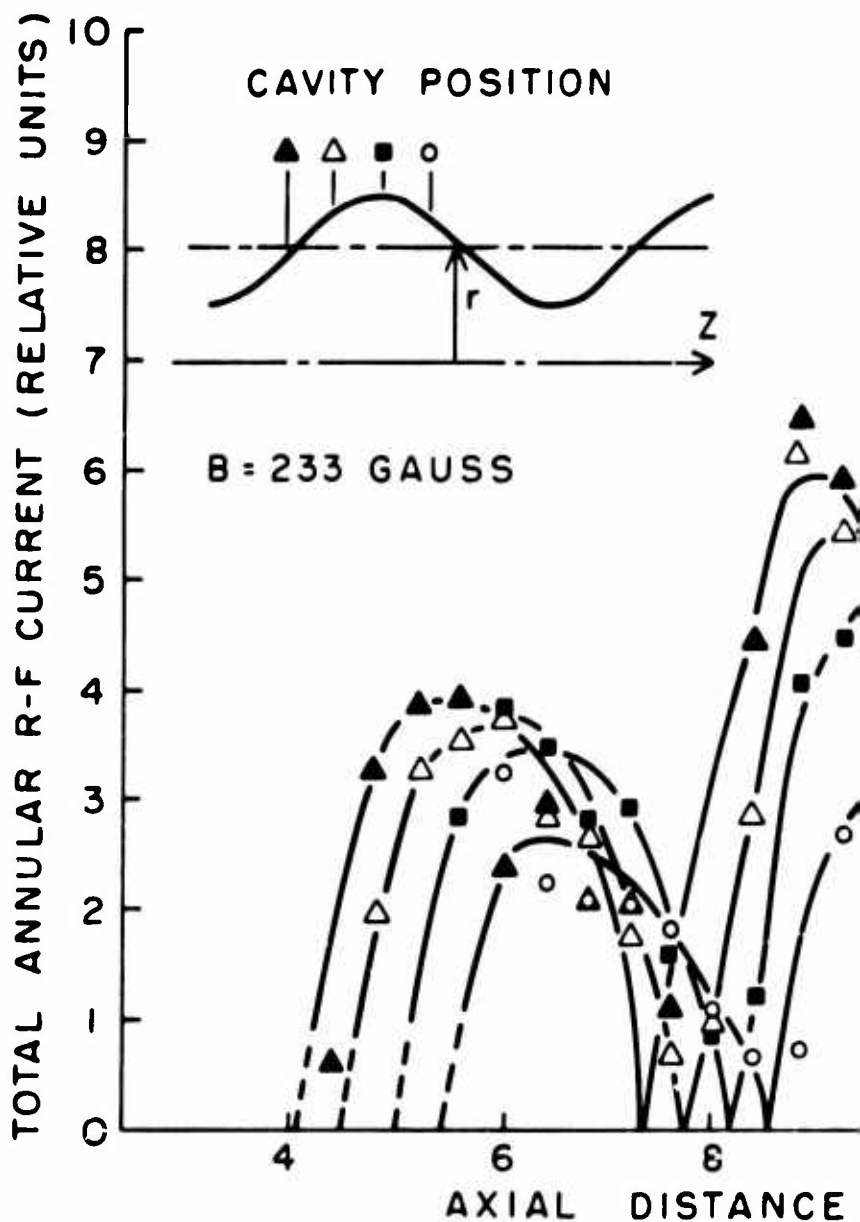
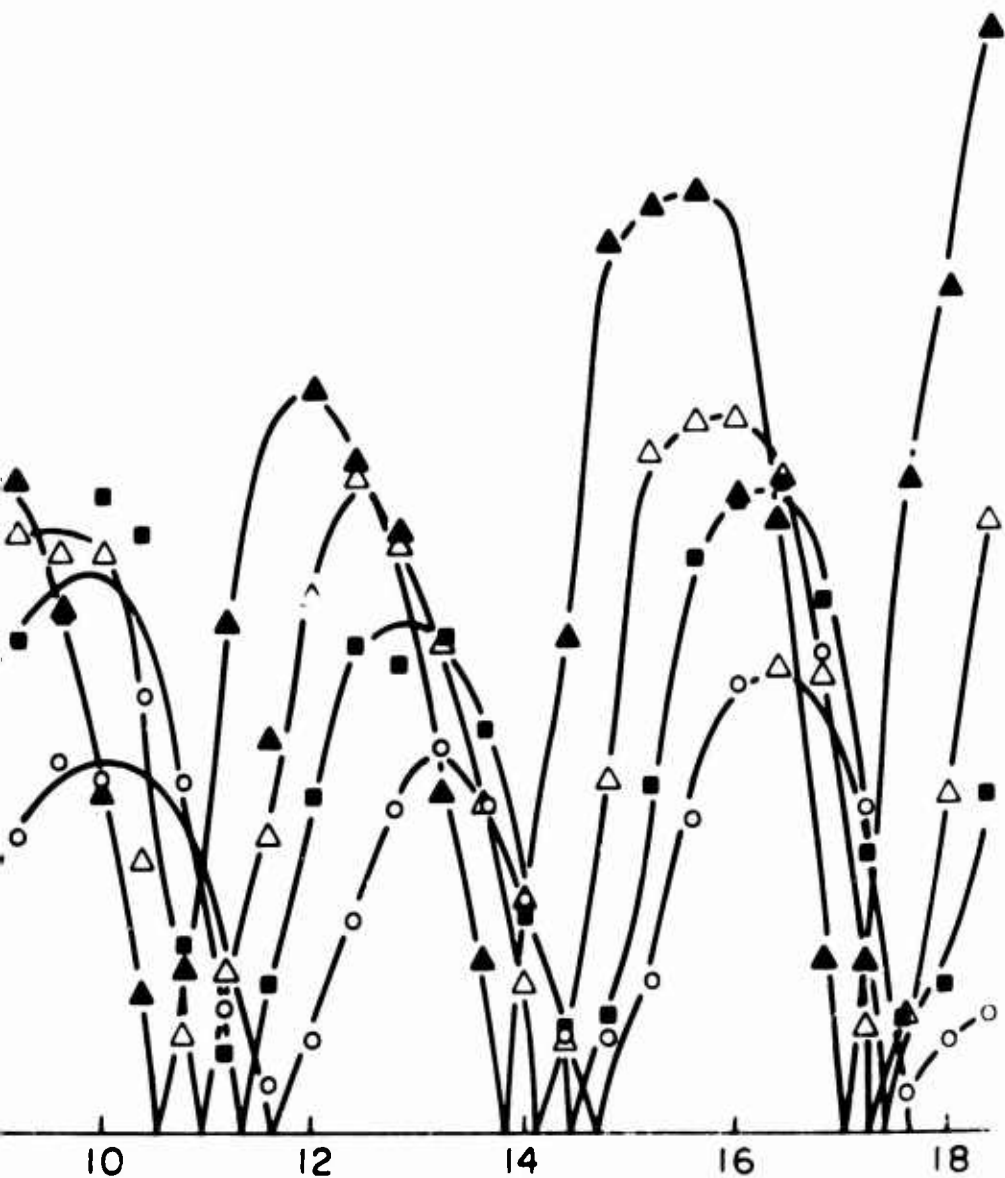


FIGURE 13. Total Annular
Distance from the Anode with Ca



DISTANCE FROM ANODE (INCHES)

r-f Current versus Axial Distance from Anode as Parameter.

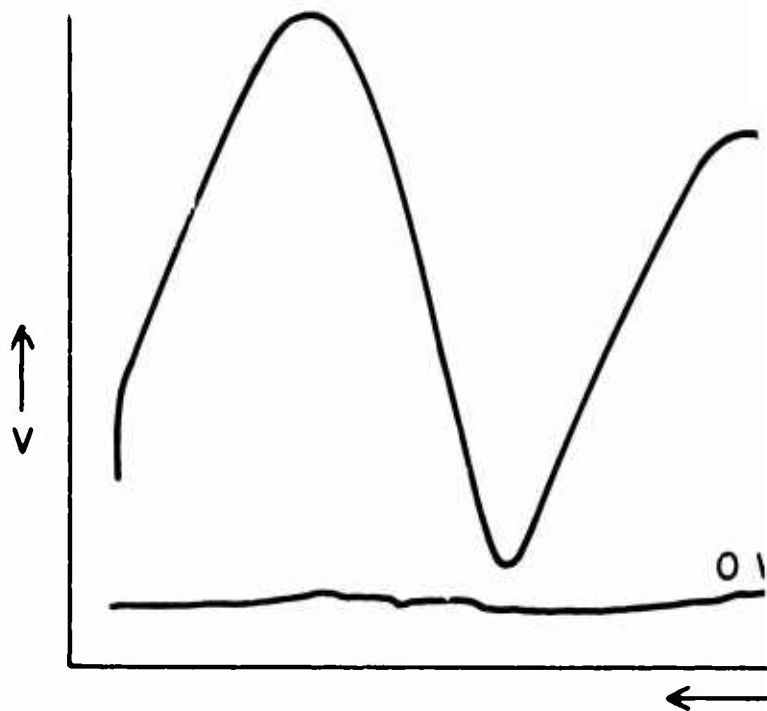
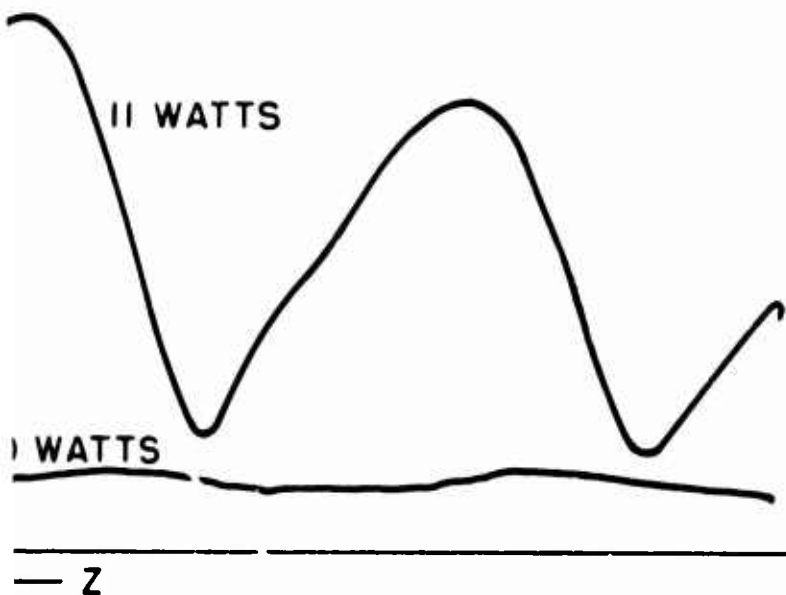


FIGURE 14 Peak-Velocity
the Scalloped Beam with an

B = 195 GAUSS

$X = \pi/4$



ity Standing Waves along
and without an Input Signal.

the two regions of high and low density. A second point to notice is that the maxima are not equally spaced between the minima as would be customary in sinusoidal behavior. A longer bunching distance and shorter debunching distance, as suggested by the physical explanation of the mechanism, would account for this behavior.

D. DISCUSSION OF THE UNPREDICTED RESULTS

During the course of the experiment, four results appeared that were not adequately explained or expected by the theory. Two of these phenomena are of some possible importance. These two effects are the r-f power saturation reducing the growth rate and the growth of the no-signal peak velocity on the beam. The third matter has to do with differences in behavior between the current and velocity standing waves. Lastly, nonuniform behavior in some of the standing wave patterns is of concern.

1. Power Saturation

Figure 15 shows a family of curves of peak velocity where power level is the parameter. The level is varied from $1/8$ w to 11.5 w. The effective gain rates (averaged over the length of the beam) at this magnetic field and three others are plotted as a function of drive level in Figure 16. The apparent drop-off of gain at low power is caused by low-signal levels with the attendant loss of sensitivity. It is seen that saturation begins to occur at drive levels above a few watts and depends

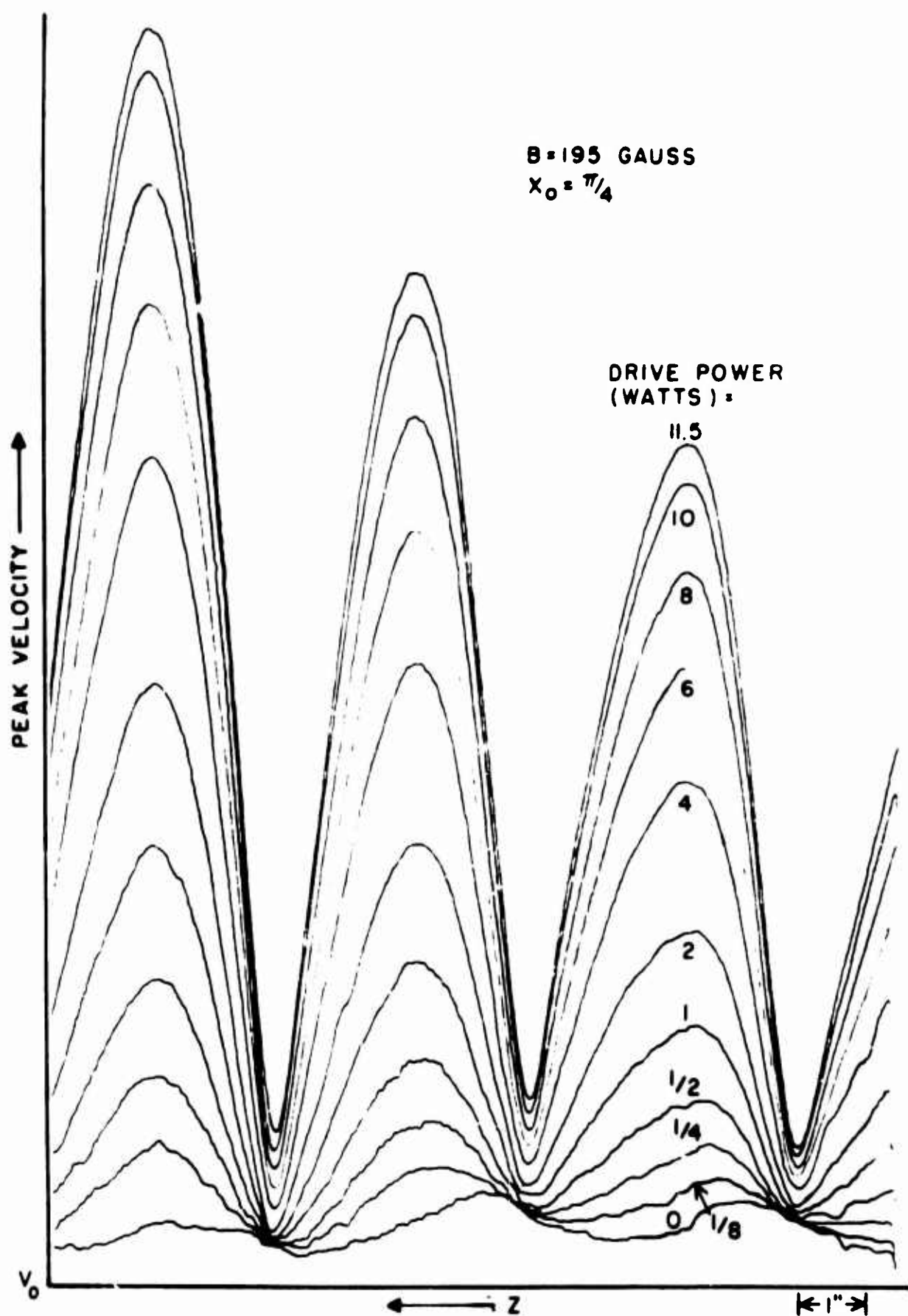


FIGURE 15. Peak-Velocity Standing Waves along the Scalloped Beam for Various Input Power Levels.

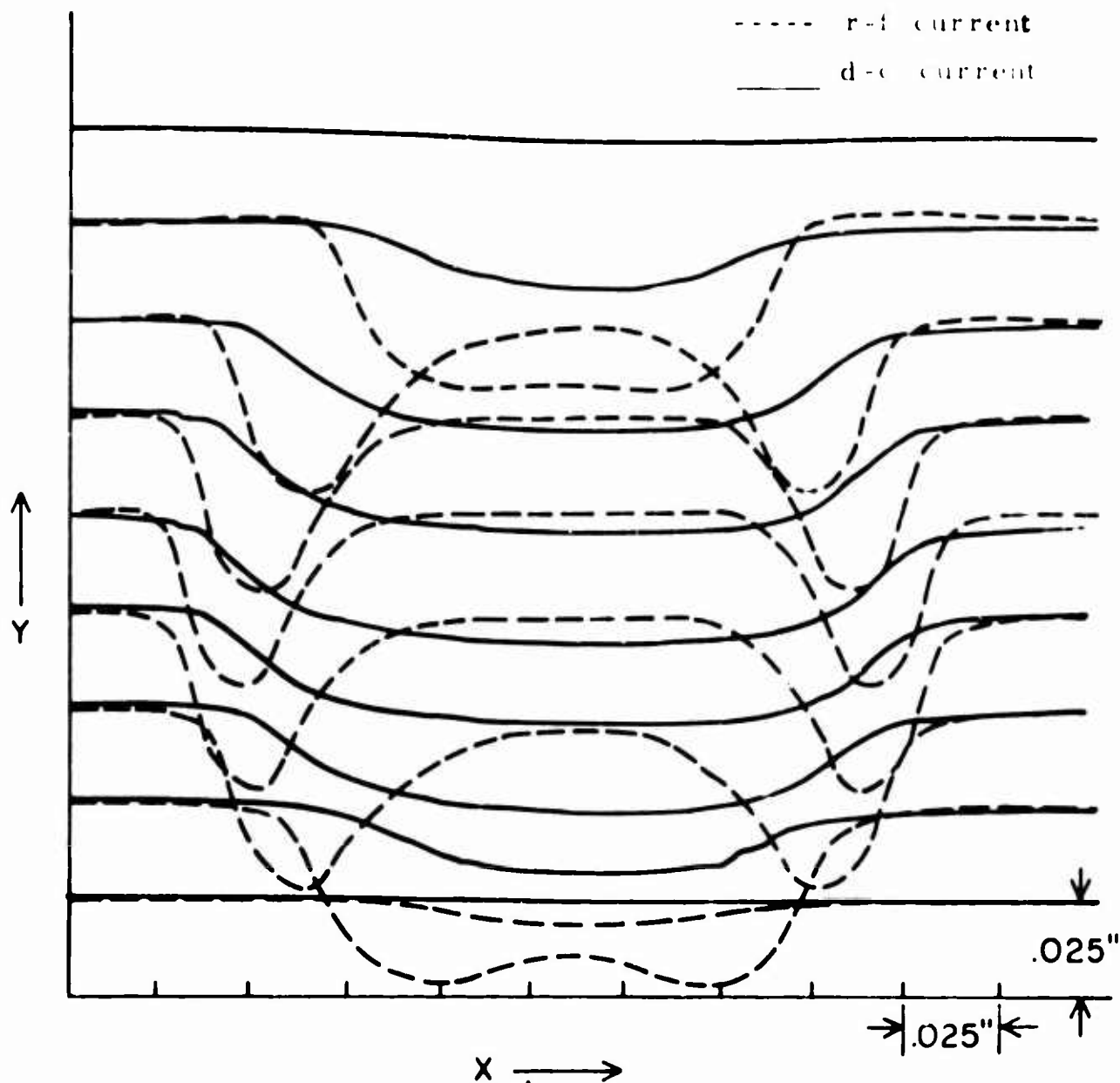


FIGURE 16. Growth Factor μ versus r-f Input Power with Magnetic Field as Parameter.

on the actual power level attained at some position in the beam. That this statement is true can be judged from the earlier saturation excitation levels for the higher gain rates. This indicates that saturation (in this report a lowering of the gain rate is implied, and not a maximum power level) begins at a power level on the order of 20 w.

Although there is no explicit mention of saturation in the theory, one can estimate the meaning of "small signal" currents as being an a-c to d-c ratio of 0.1, corresponding to a power ratio on the order of 1 per cent or 20 w in this case. Thus, the appearance of power saturation tending to limit the gain rates is not surprising, though not entirely expected. This, of course does not explain the low-saturation-level mechanisms, but does appear to put a limitation on the usefulness of the scalloped-beam amplifying mechanism.

Recent experimental work by Gilmour¹⁶ provides interesting results that are pertinent to this discussion. Using the same type beam, he applied higher power drives at 1940 Mc/s to the beam under Brillouin-flow conditions. At 200 w input, the r-f current completely disappeared within a full space-charge wavelength, and at 100 w severe saturation was evident, although normal small-signal behavior resumed within a space-charge wavelength. With the drive set at 50 w, the space-charge waves were constant in amplitude and followed the usual sinusoidal behavior. These results would tend to place the limiting factors for the saturation in this experiment with the scalloped-beam amplification mechanism and not with the beam itself.

A qualitative argument can be given to help correlate the saturation effects in this and Gilmour's experiments. The energy in an unmodulated scalloping Brillouin beam can be considered as the sum of three parts. The first and the largest part is the longitudinal energy of uniform axial motion. The second part corresponds to the radial energy of strict Brillouin flow, i.e., $\dot{r} = 0$ for all electrons. The

third part can be called "excess" radial energy and is associated with the additional energy in scalloping.

With these distinctions in mind, it is understandable that there would be two different saturation levels, one associated with longitudinal interaction and the other with radial interactions. Gilmour's saturation experiment showed the effects of nonlinearities at r-f to d-c power ratios on the order of 0.1. His experiment dealt with Brillouin flow and the interaction of r-f waves with the longitudinal energy only. In this present experiment, nonlinear effects were apparent at r-f to d-c power ratios of .01. This value is computed, however, with respect to the longitudinal energy of the beam and is therefore misleading. The power ratio should be calculated with respect to the d-c energy that is being converted to r-f energy. The source of d-c energy that is being tapped in this mechanism is the "excess" radial motion. Since the "excess" energy is probably at least an order of magnitude smaller than the longitudinal energy, the ".01" figure is actually .1 or more.

In summary, it is seen that nonlinearities tend to limit uniform space-charge wave behavior to a level of about 10 percent of the d-c energy source. The absolute power saturation level is then much lower for the scalloped beam amplification mechanism since it depends upon the "excess" radial energy.

2. Anomalous Velocity Growth

A family of curves describing the second important phenomenon is shown in Figure 17, where magnetic field is the parameter. Each

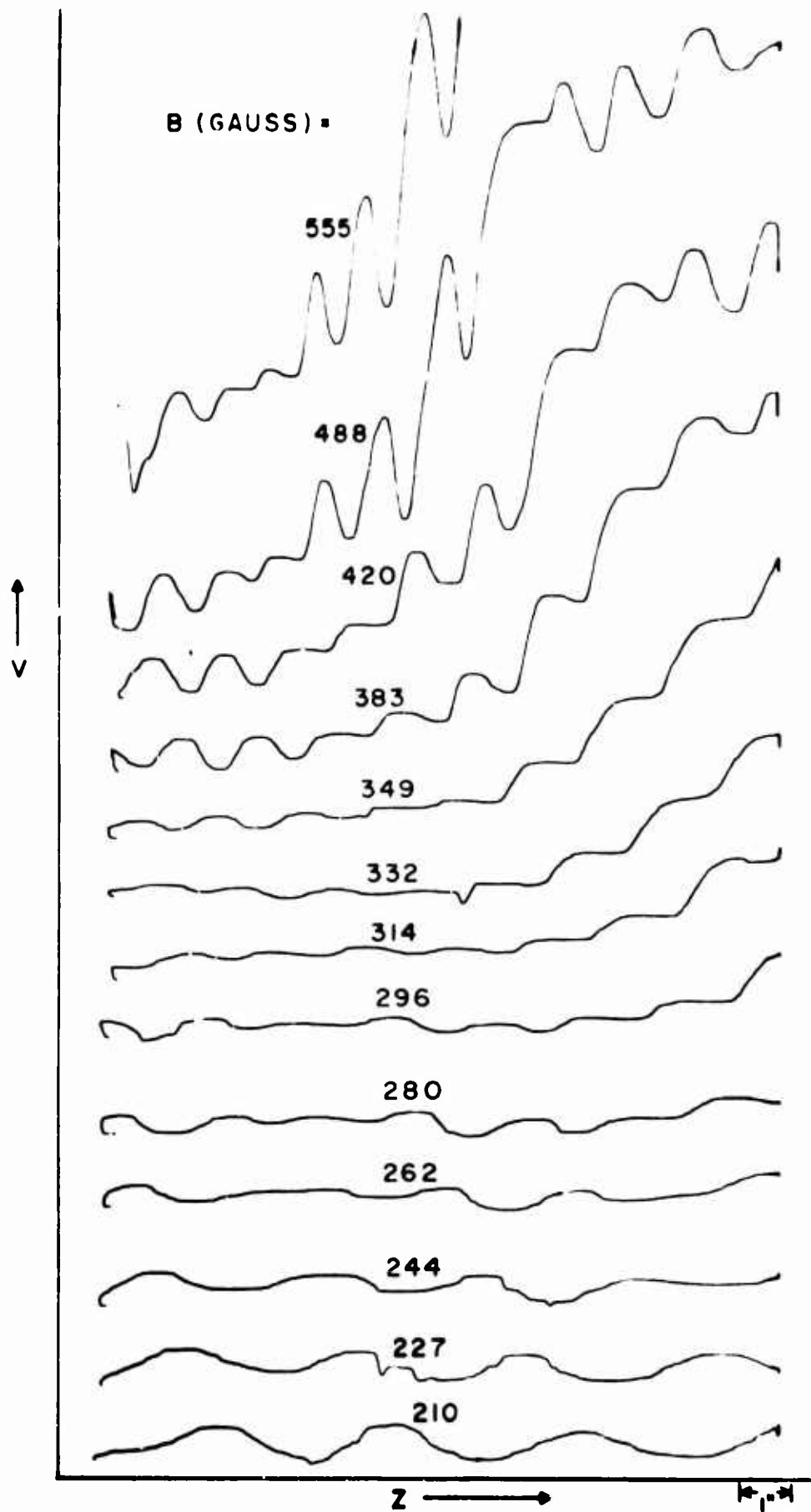


FIGURE 17. No-Signal Peak Velocity along the Scalloped Beam for Various Magnetic Fields.

curve is the peak velocity along the center of the beam with no signal applied to the cavity. This increase in the peak velocity can be divided into three regions after the stable section. First is a slow-growth region, then a rapid growth region, and finally a slow growth plateau region. The magnitude of the highest plateau is on the order of 50 v above the base level. This effect appeared in Gilmour's reports⁵ as an increase of the minima in his plots of velocity standing waves using much higher drive powers than were available in this experiment. Recent investigations of this phenomenon by Professor T. G. Mihran¹⁷ on this equipment has shown the velocity growth sharply dependent upon the cathode flux caused by a variation from the optimum in the phasing between the filament current and the pulse voltage. The periodic variations in the voltage waves are those associated with the wobble wavelengths. Corresponding growths were not detected in representative current data taken at the same levels of magnetic field. A possible explanation for this growth is the scalloped-beam amplification mechanism operating on higher-frequency noise waves. This hypothesis is supported by two facts: The first is the experimental verification that there was no growth in the current at 2917 Mc/s; the velocity measurement is frequency independent. The second fact is that gain appears possible, theoretically, at magnetic fields higher than the Brillouin value if the synchronism point is shifted to the higher magnetic fields. This shift can be accomplished by an increase in the frequency which raises p , and therefore lowers the entire λ_q curve.

3. Differences Between Current and Velocity Data

The shift of the minima was predicted to occur in all but the cases $x_0 = \pi/4$ and $3\pi/4$. Plots of the current data showed the expected results, but most of the velocity data exhibited the form of a strict periodicity with no phase shifts. The exceptions are illustrated in Figure 18 which shows the theoretical values of the plasma half-wavelength and three types of experimental data. The data labelled "locking" are those shown in Figure 12 and refer to the velocity standing waves having constant wavelengths along the entire beam. The data labelled "unlocked" are also values of constant wavelengths of velocity waves, but shorter than the locked wavelengths. These data are called "unlocked" because they would seem to correspond to the unperturbed plasma wavelengths, but they do not agree with the calculated values shown by the solid line. Also, these data were taken with the cavity placed at or near the optimum attenuation plane and were not detected at any other cavity plane. In addition, the theory does not allow any periodicity other than that of the scallop; suggesting some abnormality in the situation. The data labelled "locking" all refer to a single profile and are reminiscent of the expected behavior as the wavelength shifts from a low value to the locked value. This profile of shifting phase was taken with the cavity at a position near the maximum attenuation position, but was growing owing to a high gain rate. This particular curve was apparently the transition between the single case of unlocked wavelengths and the majority of cases where the wavelength was locked. The d-c beam at these particular conditions appeared to be perturbed by the

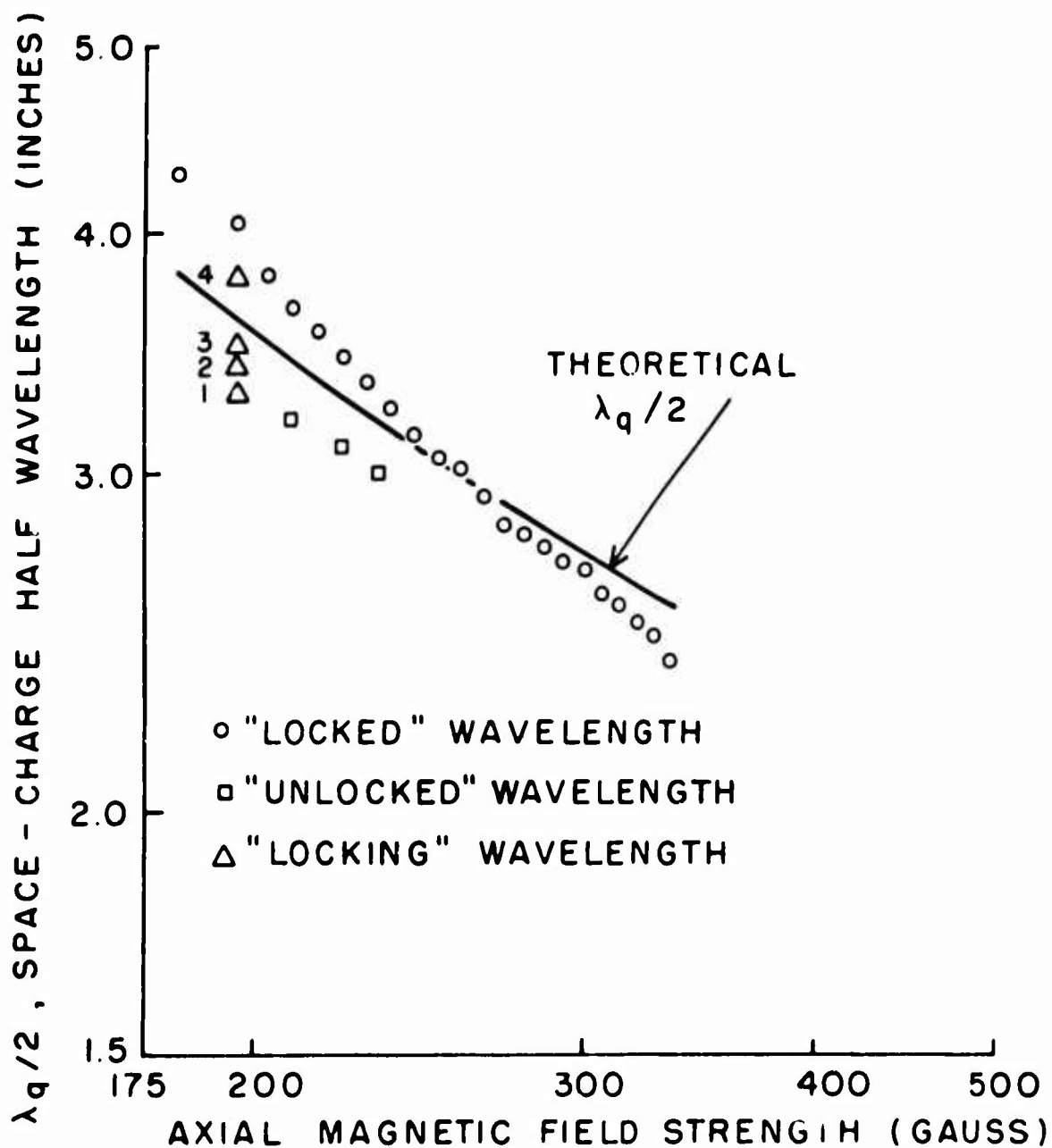


FIGURE 18. Effective Plasma Half-Wavelength versus Axial Magnetic Field Strength. (Curve shows plot of theoretical values of space-charge half-wavelength; data points are measured values taken from velocity standing waves.)

cavity location to the extent that the behavior at the current-density maxima was not sinusoidal.

Since the theory makes no essential distinction between the velocity and current envelopes, it is reasonable to ascertain whether there is some physical difference between the two types of waves. As the analysis is macroscopic, the actual nature of current and velocity distributions on a Brillouin beam has been neglected. It has been stated and experimentally verified that the current consists of ripples on the surface. On the other hand, the velocity is a body effect (see velocity cross-sections reported by Gilmour⁵) and is essentially constant across the cross-section. As a matter of experimental fact, some body current was detected when the maximum of the space-charge wave occurred at a minimum of the beam radius and the scalloping was substantial. Careful consideration of the sample data for amplification in Figure 5 discloses very small amounts of current at the center of the beam. This current, however, becomes unimportant when the radial weighting factor is taken into account. Thus, it can be said that the only apparent theoretical difference between the current and velocity waves which could cause the observed difference in behavior is the physical nature of the wave distributions themselves.

4. Nonuniformities

The remaining point to be discussed is the nonuniform behavior of some velocity standing-wave patterns. One form of the nonuniformity is seen in the data with cavity position as parameter (Figure 10). Here the envelope is not smooth, i.e. heights of alternate maxima vary above and

below an average growing envelope. These data were taken at a time later than the data in Figure 7, where the envelope does grow smoothly. There was, however, no deliberate or noticeable change in any parameter between these two data runs.

Nonuniformities were also noted whenever the cavity was placed at the position of maximum attenuation. This behavior can be noted in Figure 10 for the cases of maximum attenuation. As the cavity approached $x_c = 3\pi/4$, the minima became broad. These cases are also unusual in that the periodicity changes to that of the "unlocked" wavelength. It is therefore probable that the perturbation caused by either a slight interception or a steering by the cavity affects the beam. After a few cycles of attenuation, the decaying plasma wave has a small amplitude and is more susceptible to beam disturbances than a growing wave. As previously mentioned, experimental axial current-density profiles did show the perturbing effect of the cavity at certain positions of the cavity. This perturbation was recognized as a local disturbance and was not important enough to warrant reworking of the cavity.

VI. SUMMARY OF CONCLUSIONS

The result of the small-signal, small-scalloping, linear analysis is that space-charge wave propagation on a scalloping beam can be described by the solutions of Mathieu's Equation. These solutions can be unstable if the ratio of the scallop wavelength to half the plasma wavelength is approximately unity and the scalloping is large, (although the scalloping must be less than about fifty per cent to keep the linearity conditions). Both the unstable and the stable solutions were observed and were in qualitative agreement with the simple theory. In order to obtain close quantitative agreement with the data, it was necessary to include the effects of a fraction of a per cent of cathode flux and small translaminar streaming on the scallop wavelength, which was shortened from the predicted value of the laminar theory.

The calculated variation of the gain rate with magnetic field was presented and compared to the measured values taken from velocity and current data. For the highest growth rate having a gain rate of $\mu = .097$, the calculated value is .107. This is a favorable comparison when it is realized that μ , unfortunately, is sharply dependent upon the amount of scalloping and the wavelengths, and a few per cent error in one of these quantities is magnified in the gain-rate calculation. The forms of the variations were essentially identical except for the appearance of some gain at higher than expected magnetic fields. The plot of measured gain rates appeared to be proportional to the measured scalloping percentages.

A plot of the path of operation on the Mathieu diagram showed that solutions in both the unstable and stable regions were excited.

Consideration of the μ contours on the diagram showed that increasing the frequency or the perveance, and decreasing the magnetic field might increase the gain, whereas an increase in the voltage would definitely increase the gain rate.

The effect of the cavity position on the form of the total solution was measured and found to be that predicted, with the exception of a slightly smaller region of growth along the scallop than predicted. The analysis states that for large enough gain rates, the curve of growth versus cavity position is essentially flat except for the resonance decay plane, but at the low values attained in this experiment the maximum gain could only be achieved over a very small portion of the scallop.

Wavelengths of both the current and velocity standing waves were measured and compared to the results of the Mathieu-Equation analysis. The phenomenon of locking between the periods of the scallop and plasma waves is a consequence of the periodicity of the Mathieu functions themselves and was verified by experimental measurement. The unperturbed effective plasma wavelength was calculated with the unscalloped Brillouin-beam reduction factors and was used in determining the gain rates. The measured values of the plasma wavelength agreed with the predictions reasonably well in the stable region, but were exactly synchronized to the scallop wavelength in the unstable region. It is therefore possible to use the published reduction factors as if the scalloped beam were a perfect Brillouin beam, the radius of

which was the equilibrium radius of the scalloped beam.

The scallop wavelengths measured near the beam axis corresponded to the predictions of the laminar theory if .4 per cent cathode flux is allowed. The scallop wavelengths used for the calculation of the gain rates were measured on the beam edge and were a few per cent shorter than the laminar values. This few-per cent difference was critical enough, however, to give very misleading results for the gain rates.

The analysis predicted a shift in the minima as the growing component dominated the total solution. The current data did show this effect, and the nulls moved toward the optimum excitation plane at $x_0 = \pi/4$. The velocity data on the other hand did not show this behavior, except for a few instances in which there was apparently a disturbance on the beam.

The underlying cause of the gain mechanism, the variation in electron density, was graphically presented in the changing curvature of a velocity standing wave. It is this periodically varying density, alternately weakening the space-charge forces opposing bunching and strengthening the forces opposing debunching, that brings about the scalloped-beam amplification.

A saturation or lessening of the gain rate was observed as the r-f power approached 20 w on the 2-kw beam. Rather than the 1 per cent value that is implied by these figures, the 20 w was probably more than 10 per cent of the d-c power that could be converted from excess transverse energy. Experimental work by Gilmour with

unscalped beams showed that this beam could support over 50 w at normal space-charge wave behavior, confirming the hypothesis that the saturation was a function of the gain mechanism and not of the beam itself.

Anomalous velocity growths at magnetic fields above the Brillouin field were observed. The gain rates increased with magnetic field, and the lack of growth in the current data at 2917 Mc/s strengthened the belief that higher-frequency noise currents were being amplified by the scalped beam amplification mechanism.

A more complete understanding of the peak-velocity measurements in this experiment would be helpful in understanding some of the phenomena observed with the retarding-field potential technique. This measurement samples only some of the fastest electrons in the beam and is no longer simple when used with a scalloping beam.

One of the heralded advantages of Brillouin flow for a laminar beam is the economy of magnetic field. It is, therefore, interesting to note that for excitation frequencies at and below approximately 3 kMc/s, a scalloping beam offers more economy and possible gain, with the beam-spreading amounting to less than twice the original linear dimensions.

In conclusion, this experiment shows that the Mathieu Equation model is qualitatively accurate, but is highly sensitive to slight disturbances on the electron beam. Hence, any useful calculations must be done a posteriori to take account of the particular beam optics involved.

APPENDIX: DESCRIPTION OF THE APPARATUS

The most important parts of the electron-beam analyzer, originally built by Gilmour and modified first by Hallock and then the author, are the vacuum system and the scanning mechanism. The associated electronics are essentially standard and have been described earlier. Details of the scanning mechanism, the cavity and the electron gun can be found in a previous report.¹⁸

A. VACUUM SYSTEM

The vacuum system is divided into two distinct parts: one part is the primary (high-vacuum) section and the other is the secondary ("rough"-vacuum) section.

1. Primary Section

The main vacuum envelope consists of the drift tube (4 1/4 in. i.d. x 22 in.) housing the scanning mechanism and the formed beam, the supporting "tee" section leading to the 75 l/s VacIon pump, and the gun section. This entire chamber is held at pressures below 1×10^{-7} Torr (as indicated on the pump-control unit) while data is being taken. This system is simply cleaned with alcohol and not baked. The 75 l/s VacIon pump can be sealed off from the system by a free-floating, neoprene O-ring valve positioned externally by C-magnets. Because this valve allows the pump to be continuously under vacuum and not exposed to the atmosphere, pump life is lengthened. A Varian high-vacuum

valve is located above the pump to permit starting of the system by a portable mechanical rough pump with its associated liquid-nitrogen cold trap.

The gun section can be separated from the drift tube by a quarter-turn ball valve. The ball valve has a stainless-steel sphere with a 5/16-in. cylindrical hole through its center; the sphere is compressed between two spherical (concave) Teflon seats. The annular Teflon seats have been undercut to prevent interference with the electron beam by the dielectric material. With the ball valve closed, the cathode is maintained in its activated state at pressures much lower than 1×10^{-7} Torr, while the drift tube is open to the atmosphere. The gun is pumped with a 1 l/s VacIon pump operated by a battery supply, so that with the valve closed, a power failure cannot damage the cathode.

2. Secondary System

The secondary vacuum system is slightly larger than the drift tube and houses those portions of the scanning rods that enter the main vacuum system. In this way, the parts of the rods entering the high-vacuum chamber are never subjected to atmospheric pressure, and therefore cannot contaminate the drift-tube section. This section is kept at a 1×10^{-2} Torr pressure with a mechanical pump and associated Xeolyte trap.

3. Construction

The entire system is demountable and fastened together with

bolted flange joints. All parts, other than the gun and pole pieces, are made from nonmagnetic type-304 stainless steel and are fabricated with either brazed or heliarced joints.

4. Seals

The majority of the fixed seals are made with flat flanges and a lead (fuse wire) O-ring squeezed between the flanges. Creeping of the lead stops after a few days, during which time periodic tightening of the bolts is required. The other fixed seals are copper ConFlat (hermaphroditic type) gaskets compressed between stainless-steel knife-edge flanges. All the sliding seals (seals through which rods pass and turn) are made with Teflon O-rings held in place with Veeco "Quick-Couplings." These O-rings flow over a long period of time, and the coupling must be tightened periodically, and the O-rings eventually replaced.

Vacuum grease is put on the rods to assure adequate seals even with the presence of microscratches.

B. SCANNING MECHANISM

The scanner as seen by the beam is a .003-in. Molybdenum, grounded collector plate carbonized with Aquadag to reduce secondary emission. The plate has a .010-in. hole in the center. Behind the scanner plate is a thicker support plate with a larger hole; 1/32 in. behind the .010-in. hole is the entrance to the Faraday cage. The cage is insulated from ground by a ceramic sleeve and leads through

a flexible cable to a 5/8-in. 50-ohm stainless-steel line. The entire scanning mechanism has been r-f shielded with many layers of copper braid and mesh, and leak-tested to assure no spurious responses.

The cage and pinhole assembly are supported from the two rods extending into the drift tube from the outside through the secondary vacuum system. (If the pinhole is at the center of a clock, then the vertical positioning rod is at 9 o'clock and the horizontal positioning rod is at 6 o'clock.) Extending radially inward from each of the support rods are two parallel 1/8-in. stainless-steel rods. The Faraday-cage scanner assembly riding on Teflon bearings can move on these two sets of parallel rods in the transverse plane. The most common mode of operation has been to scan the x-z plane with y fixed. In this mode, the vertical positioning rod is adjusted so that the pinhole is on the horizontal center line of the beam. The horizontal positioning rod is now driven back and forth through a small angle. The motion of the pinhole is essentially straight across the diameter of the beam. The lever arms are approximately 2 in. long, and the beam diameter is less than .300 in. , causing a departure from linearity of less than .15 per cent.

C. CATHODE

The cathode structure, made of the cathode surface and the attached focus electrode, was provided by Sperry Gyroscope Co. The emitting surface was applied in the form of a 3 to 4 mil layer of BaCO_3 sprayed onto the nickel spherical segment cathode in thin

layers after the entire structure had been chemically cleaned and hydrogen fired. No difficulties were experienced with the cathode coatings in the several months of experimentation.

VII. REFERENCES

1. O. E. H. Rydbeck and B. Agdur, "The Propagation of Electronic Space-Charge Waves in Periodic Structures," Chalmers Tekniska Hogskolas Handlingar, No. 138, 1954.
- 1a. C. K. Birdsall, "Rippled Wall and Rippled Stream Amplification," Proc. I.R.E., 42 (November 1954), pp. 1628-1636.
2. S. Bloom, "Space-Charge Waves in a Drifting, Scalloped Beam," Tech. Rep. PTR-363, RCA Laboratories Division, RCA, Princeton, N. J., January 1954.
3. J. A. Rich, "Space-Charge Waves in an Electron Beam of Sinusoidally Varying Charge Density," A talk presented at the twelfth Annual Conference on Electron Devices, University of Maine, June 1954.
4. T. G. Mihran, "Scalloped Beam Amplification," Trans. I.R.E., ED-3, (January 1956).
5. A. S. Gilmour, Jr., "The Velocity Distribution in a Velocity-Modulated Electron Beam from a Shielded Pierce Gun," Res. Rep. EE 507, Cornell Univ., August 1961.
6. M. Roberts, "Investigation of Small-Signal R-F Modulation on D-C Scalloped Brillouin Beam," in Res. Rep. EE 558, Cornell Univ., July 1963.
7. C. C. Wang, "Electron Beams in Axially Symmetrical Fields," Proc. I.R.E., 38 (February 1950), pp. 135-147.
8. L. J. Chu, A paper given at the I.R.E. Conference on Electron Tubes, Durham, N. H., 1951.

9. S. Bloom and R. W. Peter, "Transmission-Line Analogy of a Modulated Electron Beam," R.C.A. Review, 15 (March 1954), pp. 95-112.
10. N. W. McLachlan, Theory and Application of Mathieu Functions, Oxford: Clarendon Press, 1947.
11. A. H. W. Beck, Space-Charge Waves, New York: Pergamon Press, 1958, pp. 118 and 125.
12. W. W. Rigrod and J. A. Lewis, "Wave Propagation along a Magnetically Focused Cylindrical Electron Beam," The Bell System Technical Journal, 33 (March 1954), p. 108.
13. D. D. Hallock, "An Investigation of the Laminarity of Flow in a Magnetically Confined Electron Beam," Res. Rep. EE 539, Cornell Univ., September 1962.
14. G. R. Brewer, "Some Characteristics of a Magnetically Focused Electron Beam," Jour. Appl. Phys., 30 (July 1959), pp. 1022-1038.
15. A. S. Gilmour, Jr., "A Beam Tester for Studying the Characteristics of Velocity-modulated Electron Beams," Res. Rep. EE 495, Cornell Univ., May 1961.
16. A. S. Gilmour, Jr., "Drive-Induced Current Minima in Velocity-Modulated Brillouin Beams," in Res. Rep. 575, Cornell Univ., December 1963.
17. T. G. Mihran, "Peak-Velocity Growth along Scalloped Brillouin Beams," in Res. Rep. EERL 3, Cornell Univ., February 1964.
18. M. Roberts, "Investigation of Small-Signal R-F Modulation on D-C Scalloped Brillouin Beam," in Res. Rep. EE 575, Cornell Univ., December 1963.